NEGATIVE CAPACITANCE SHUNTING OF PIEZOELECTRIC PATCHES FOR VIBRATION CONTROL OF CONTINUOUS SYSTEMS

A Dissertation
Presented to
The Academic Faculty

By

Benjamin Stewart Beck

In Partial Fulfillment
Of the Requirements for the Degree
Doctor of Philosophy in the
George W. Woodruff School of Mechanical Engineering

Georgia Institute of Technology

December, 2012

NEGATIVE CAPACITANCE SHUNTING OF PERIODIC ARRAYS FOR VIBRATION CONTROL OF CONTINUOUS FLEXURAL SYSTEMS

Approved by:

Dr. Kenneth A. Cunefare, Advisor
George W. Woodruff School of
Mechancial Engineering
Georgia Institute of Technology

Dr. Alper Erturk
George W. Woodruff School of
Mechancial Engineering
Georgia Institute of Technology

Dr. Manuel Collet
Laboratoire de Mécanique Appliquée
Raymond Chaléat
Institut Franche-Comté Electronique
Méchanique, Thermique et Optique –
Sciences et Technologies

Dr. Massimo Ruzzene
D. Guggenheim School of Aerospace
Engineering
George W. Woodruff School of
Mechancial Engineering
Georgia Institute of Technology

Dr. Krish K. Ahuja
D. Guggenheim School of Aerospace
Engineering
Georgia Tech Research Institute
Georgia Institute of Technology

Date Approved: 24 September 2012

To Becca

ACKNOWLEDGEMENTS

There are so many people I need to thank and acknowledge for their support as I have worked to receive my Ph.D., I know I will forget someone. For those not named specifically, know that I could not have done this without all of you and I am grateful for all you have done.

Specifically, I would like to acknowledge the tremendous and continuous guidance, support, and expertise of my advisor, Dr. Ken Cunefare. His experience and knowledge on all topics (technical or otherwise) has been an immense help. For the rest of my academic career, my goal will be to exceed his already high standards. Dr. C is my academic and professional role model and I will always be in his debt.

I would also thank my reading committee Dr. Collet, Dr. Ruzzene, Dr. Erturk, and Dr. Ahuja. In particular, Dr. Collet's guidance and encouragement pushed me when I truly needed it. In addition, I want to thank all the people who have given enormous technical support to my project, including Filippo Casadei whose modeling proficiency is unmatched, Kyle French’s help with circuit difficulties, and Antonette Benford who made my life easier in so many ways. I cannot thank my office and lab mates enough, especially Nick Earnhart. Listing all the ways that Nick has helped me in this endeavor would be impossible. I must also mention Robert Amaro, Man Prakash Gupta, Elliott Gruber, and Ellen Skow for ensuring that I made it through each day.

My friends and family’s support, reassurance, and inspiration over the past 5 years has been perfect. Thank you to my wife, Becca: she is the greatest cheerleader and strongest support I could ever ask for. To all my parents, Lou, Bill, Susan, and Tripp, and all my siblings, thank you for believing in me. Similarly, thank you to Ryan Kane and Garey Gomez for knowing I could do this.

TABLE OF CONTENTS

LIST OF TABLES

LIST OF FIGURES

NOMENCLATURE

C - capacitance

$\hat{C}_{ij}$ - wave amplitude

c - elastic constant

D - electric field displacement

D_i - mass per unit length

E - Young’s modulus

e - piezoelectric constant

h - thickness

I - current

K - controller

M_i - mass per unit length

L - inductance

L_i - length

k - wave number

k_{31} - piezoelectric coupling coefficient, poling direction perpendicular to strain

p - poling direction

q - generalized coordinate

S - total apparent power

R - resistance

R_{pot} - tuning potentiometer total resistance, $R_3 + R_4$

u - transverse velocity

V - voltage

V_o - strain-induced voltage

w - transverse displacement

Y - admittance

Z - impedance

α - tuning parameter, R_3/R_{pot}

δ - attenuation constant

ξ - dielectric constant

ε - strain

κ - stiffness modulus ratio

η - loss factor modulus ratio

ϕ - electric field intensity

φ - basis function

ω - angular frequency

σ - stress

μ - propagation constant

υ - Poisson's ratio

Superscripts

D - open-circuit

E - short-circuit

S - constant strain

SU - shunted

T - constant stress

Subscripts

b - beam

P,p - patch

S,Z - shunt

SUMMARY

The ability to reduce flexural vibrations of lightweight structures has been a goal for many researchers. A type of transducer-controller system that accomplishes this is a piezoelectric patch connected to an electrical impedance, or shunt. The piezoelectric patch converts the vibrational strain energy of the structure to which it is bonded into electrical energy. This converted electrical energy is then modified by the shunt to influence to mechanical response. There are many types of shunt circuits which have demonstrated effective control of flexural systems. Of interest in this work is the negative capacitance shunt, which has been shown to produce significant reduction in vibration over a broad frequency range. A negative capacitance circuit produces a current that is 180° out of phase from a traditional, passive capacitor. In other words, the voltage of the capacitor decreases as charge is added. The negative capacitance shunt consists of a resistor and an active negative capacitance element. By adding a resistor and negative capacitor to the electrical domain, the shunt acts as a damper and negative spring in the mechanical domain.

The performance of the negative capacitance shunt can be increased through proper selection of the shunt's electrical components. Three aspects of component selection are investigated: shunt efficiency, maximum suppression, and stability. First, through electrical modeling of the shunt-patch system, the components can be chosen to increase the efficiency of the shunt for a given impedance. Second, a method is developed that could be utilized to adaptively tune the magnitude of resistance and negative capacitance for maximum control at a given frequency. Third, with regard to stability, as the control gain of the circuit is increased, by adjusting the circuit parameters, there is a point when the shunt will become unstable. A method to predict the stability of the shunt is developed to aid in suppression prediction.

The negative capacitance shunt is also combined with a periodic piezoelectric patch array to modify the propagating wave behavior of a vibrating structure. A finite element method is utilized to create models to predict both the propagation constant, which characterizes the reduction in propagating waves, and the velocity frequency response of a full system. Analytical predictions are verified with experimental results for both a 1- and 2-D periodic array. Results show significant attenuation can be achieved with a negative capacitance shunt applied to a piezoelectric patch array.

CHAPTER 1

INTRODUCTION

1.1 Research Motivation

The ability to reduce vibrations of flexural systems through application of various control methods has been a widely studied field. The control of vibration is desirable for many reasons including fatigue reduction, acoustic noise mitigation and reduction in unwanted structural responses. The focus of this work will be the investigation of reduction of broadband low- to mid-frequency flexural vibration of thin plates and beams through application of a negative capacitance circuits, or shunts, connected to piezoelectric actuators. A shunt is considered to be any electrical circuit that connects the two electrodes, or leads, of a piezoelectric element.

Current types of shunts consist of either passive circuit elements, limited to narrow-band control, or active control methods which may be complex. One alternative shunt configuration, a negative capacitance shunt, is a particularly simple, adaptive solution for vibration attenuation. This shunt bridges the gap between the simplicity of a passive circuit solution and the broadband control ability of active methods. The negative capacitance shunt is a self-sensing controller, in that a connected piezoelectric patch simultaneously acts as both a sensor and actuator. Through the piezoelectric coupling, a negative capacitance shunt can be approximated in the mechanical domain as a negative stiffness, which shifts the resonance frequencies of a vibrating system to lower frequencies. When a resistor is added to the shunt, the damping of the system is also increased. While the amount of vibration control is generally proportional to the magnitude of the negative capacitance, the range achievable negative capacitance is limited by electrical stability of the operational amplifier (op-amp) utilized for implementation of the circuit. The useable magnitudes of negative capacitance are therefore limited, reducing the available control gain. Also, depending on the magnitude of the resistor added to the shunt, the bandwidth of control can be shifted or reduced.

1.2 Research Objectives and Approach

There is a need to increase the control ability of the negative capacitance shunt, in terms of control effort and effective frequency range. Two primary investigations are performed in an effort to reach this goal. First, the electromechanical behavior of the circuit is investigated to determine the correlation between the power dissipated in the circuit and the causes of circuit instability. The results of the investigation aid in determining the circuit parameters that increase vibration suppression and improve efficiency. The analysis is performed on a simple test structures to allow for straightforward comparison of vibration suppression and shunt behavior. Specifically, a thin aluminum cantilever beam with one set of control patches is used for analysis of circuit parameters to mitigate the voltage and current limitations of the op-amp. This structure is also used for comparison of negative capacitance selection methods presented in the literature. A second cantilever beam with ten high impedance patches with nominally identical properties will be used to investigate the effect of patch impedance on the stability of the shunt.

Secondly, negative capacitance shunts are applied to piezoelectric patches installed in a periodic array, which consists of a series of equally spaced piezoelectric patches. The wave motion, energy localization and frequency response of various test structures are analyzed, both numerically and experimentally, to assess the physical effects of the negative capacitance shunt. Two test structures will be utilized to assess the performance of the control system. The first consists of a long cantilever beam with a 12 element periodic array bonded in the center. This is designed to allow for measurement of both up- and down-stream response. A thin aluminum panel with 16 piezoelectric patches is also used to determine the vibration suppression of a 2D array.

1.3 Overview of Dissertation

Chapter 2 presents a literature review of the state of the art of piezoelectric shunt control. The chapter also presents four methods to determine the optimal negative capacitance shunt parameters, also known as shunt tuning methods. Chapter 3 presents the numerical modeling derivation for the vibrating structures that are analyzed in the following chapters. The implementation of negative capacitance shunts is outlined in Chapter 4 with a presentation of frequency trends of control. In Chapter 5, the electro-mechanical behavior of the shunt is investigated and a new shunt tuning method is presented. Chapter 6 presents the control advantage of applying the negative capacitance shunt in conjunction with periodic arrays. Finally, the conclusions and future work are discussed in Chapter 7.

CHAPTER 2

LITERATURE REVIEW

2.1 Introduction

This chapter outlines the fundamentals and background of the research presented in this dissertation. The first section presents the basics of piezoelectric materials and their properties. This is followed by an overview of piezoelectric control methods. The specifics and background of the use of negative capacitance shunts is presented. Four methodologies that utilize negative capacitance shunts to determine shunt parameters which correspond to maximum suppression of vibration are outlined. Finally, an overview of periodic systems and their effect on wave propagation is then discussed.

2.2 Piezoelectric Materials

The basics of piezoelectric theory are presented here as an introduction to the use of piezoelectric elements as transducers in control systems. A more thorough introduction to piezoelectricity can by be found in [1-3]. When certain materials are subjected to a stress field an electric charge is generated on the surfaces: these materials are called piezoelectric. The inherent coupling of the mechanical and electrical domains lends piezoelectric materials to be commonly used as sensors and actuators. For flexural systems, the piezoelectric elements typically are thin plates with electrodes covering the top and bottom surfaces. The plates (or patches, in literature) are bonded to the surface of a vibrating structure. This configuration allows for large sensing voltages from flexural strain or actuation forces from an induced charge from a single set of electrical connections without adding significant mass to a system.

A representative piezoelectric element is shown in Figure 2.1, which consists of a piezoelectric material with electrodes covering two sides. Mechanical and various electrical parameters will change the response of the piezoelectric element, in addition to the size, shape and direction of the applied force. Similarly, the direction of poling and electric field will alter the mechanical response. In Figure 2.1, the poling direction is shown as the vector p which, by convention, sets the negative z direction of the rectangular coordinates. The electric field is generated between the electrodes in the z direction. The constitutive equations of an unbounded piezoelectric element relating stress and strain to the displacement and intensity of the electric field are

$$\sigma_{ij} = c_{ijkl}\varepsilon_{kl} + e_{kij}\phi_k \tag{2.1}$$

$$D_i = e_{ikl}\varepsilon_{kl} - \xi_{ik}\phi_k \tag{2.2}$$

where c is the elastic constant, e is the piezoelectric constant and ξ is the dielectric constant [2]. These constitutive relations are used to find the electrical or mechanical response to induced forces or voltages. Simplification of these relationships can be made by the boundary conditions of the configuration of interest. For a typical piezoelectric transducer bonded and to the surface of a thin flexural system, the piezoelectric element will only be strained in the x and y directions and the electrical field will only vary in the z direction.

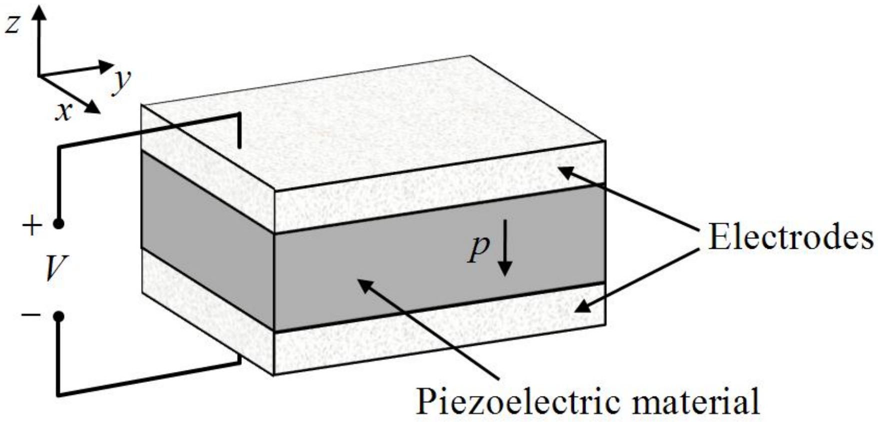

Figure 2.1 - Schematic of a piezoelectric element

2.3 Control Methods

The use of piezoelectric transducers for control purposes has been studied for quite some time by many research groups [1, 4-7]. A summary article by Mohiemani [3] and the dissertation of Niederberger [8] present an overview of the past developments (up to 2005) and an excellent summary of the main types of control methods used in conjunction with piezoelectric transducers. More thorough discussion of control using piezoelectric transducers may be found in the textbook “Piezoelectric Transducers for Vibration Control and Damping” [9]. The types of piezoelectric control methods are usually separated into passive or active methods. The following two sections highlight key works within passive and active methods for reducing vibrations of flexural systems.

2.3.1 Passive Shunts

A model of a thin, shunted piezoelectric patch which has been bonded to a substrate is shown in Figure 2.2. The system can be driven by an arbitrary force or by acoustic loading. An electrical domain model of this configuration can be seen in Figure 2.3, which includes a strain-induced voltage source V_o, the capacitance of the piezoelectric element C_p, and the shunt impedance Z_S. By making assumptions for a thin element and uniform voltage over the electrodes, the constitutive equations, Equations (2.1) and (2.2), can be simplified into one equation to express the stiffness of the patch as a function of shunt impedance [10].

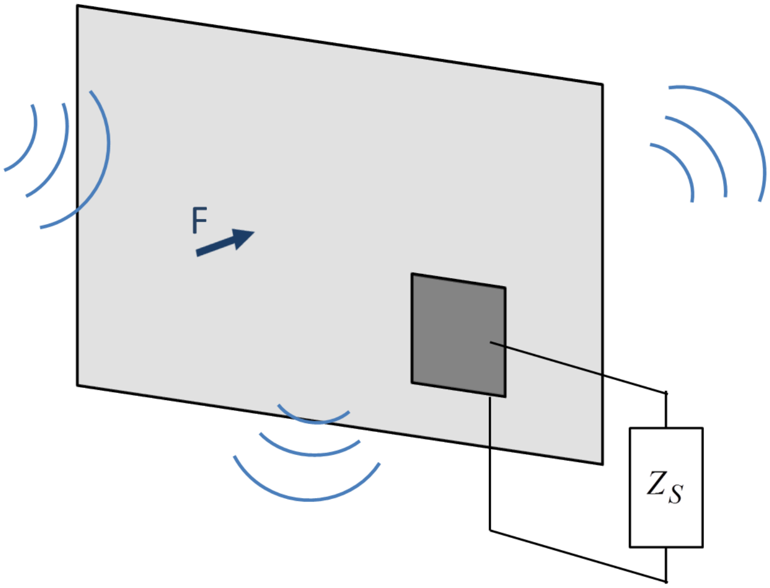

Figure 2.2 - Bonded piezoelectric patch shunted with an arbitrary impedance

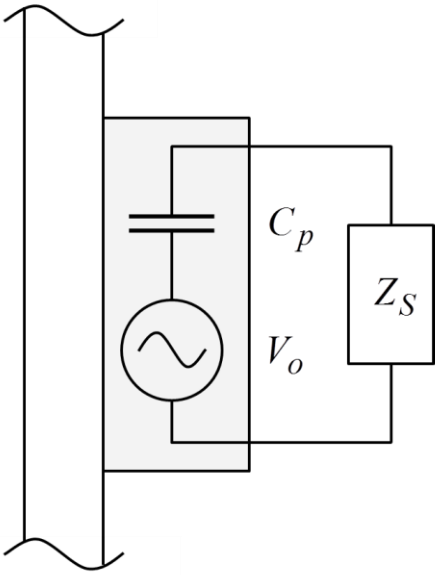

Figure 2.3 - Electrical model of a shunted piezoelectric element

The stiffness may be represented through the Young's modulus, where an approximation of the Young's modulus for the piezoelectric element is expressed as

$$E_p^{SU}(\omega) = E_p^E \frac{i\omega C_p^T + Y_S}{i\omega C_p^T (1-k_{31}^2) + Y_S} \tag{2.3}$$

where $1/Z_S = Y_S$ is the admittance of the shunt, E_p^E is the short-circuit Young's modulus of the piezoelectric material, and k_{31} is the piezoelectric coupling constant [10, 11]. The capacitance of the patch for constant stress C_p^T is related to the capacitance at constant strain by

$$C_p^S = C_p^T \left(1-k_{31}^2\right). \tag{2.4}$$

A significant result from Equation (2.3) is that the shunt has the ability to modify both the real and imaginary components of stiffness, and thus may be used to control the dynamic behavior of the piezoelectric material. Similarly, it can be seen that the relationship between the open circuit ($Z_S = \infty$) stiffness and short circuit ($Z_S = 0$) stiffness is

$$E_p^E = E_p^D \left(1-k_{31}^2\right). \tag{2.5}$$

Forward [12] was the first to investigate adding a resonant, or resistive-inductive (RL), shunt to a piezoelectric control actuator to damp a specific mode of vibration of a system. A resonant shunt works as a means of vibration control by nulling the reactive impedance of the electrical domain at a specific frequency to increase the damping of the system. Hagood and von Flotow [10] extended Forward's research with the development of Equation (2.3) and noting that a resonant shunt introduces another degree of freedom to the system. Therefore, the resonant shunt acts as a narrow-band vibration absorber, analogous to a tuned mass absorber in the mechanical domain. Many others have investigated the use of an RL shunt to damp a single resonance [13-18] or multiple modes of a densely modal system [19, 20]. Most researchers use a synthetic inductor [21] to allow for tuning to low frequency modes as physical inductors would be impractically large. The synthetic inductors are created using a circuit requiring two operational amplifiers which can be tuned to the magnitude of inductance needed. Therefore, even the passive shunt techniques are not truly passive because of the active inductors. The amount of reduction for a single mode of vibration from a passive shunt can be on the order of 10-20 dB.

The resonant RL shunt only allows for narrowband damping of vibrations, therefore other passive shunts were developed to allow for broadband control. Hollkamp initially developed a multi-branched resonant shunt that could control multiple modes of a cantilever beam [22]. Yet, this configuration is cumbersome to implement because the value of each circuit element has to be computed through numerical optimization. Therefore, to control many resonances the optimization becomes complicated. Other researchers overcame this problem by introducing either current blocking [23] or current flowing [24, 25] circuit elements into the resonant branches. These solutions allowed for each branch to be tuned individually to a specific mode. Multi-mode passive shunts retain the same control effectiveness of a single resonant shunt. There are a few drawbacks to multi-mode passive shunts. The complexity of implementation is substantial because of the number of synthetic inductors necessary for the current-flowing and current-blocking circuits. Yet, the most significant disadvantage of the multi-mode passive shunts is the non-adaptive nature of these control mechanisms. If the resonant frequencies of the host structure were to change, the narrow-band control of the tuned shunts would be greatly diminished.

2.3.2 Active/Semi-Active Control Strategies

To allow for adaptive broad-band control, active control schemes utilizing piezoelectric transducers have been developed concurrently with the passive techniques. The active control of vibrating structures is an extensive research field and cannot be fully reviewed in this dissertation. Therefore, a short overview of active control methods using piezoelectric transducers will be presented while focusing on self-sensing techniques, although many active control techniques include separate sensors and actuators. Commonly, the actuator is a piezo-element and the sensor is an accelerometer [26-30] or another piezoelectric element [31-36]. These sort of single-input/single-output control pairs have shown good control over a broad frequency range.

The use of a self-sensing piezoelectric transducer, or sensoriactuator, was developed by Dosch [37] by replacing the sensor element of a feedback control loop with a capacitor identical to the patch capacitance. This solution estimates the voltage induced on the patch to obtain an approximate mechanical strain value of the vibrating structure. The strain is used by a digital controller to drive the patch. There are many drawbacks to this method, however, because of the assumptions that are necessary and the filters that are needed [3]. Another active control implementation of a sensoriactuator is the use of a synthetic impedance [38-40]. By tailoring the shunt impedance to an arbitrary impedance that cannot be obtained by analog circuits over the frequency range of interest, the control can be maximized. A specific yet simple implementation of a synthetic impedance for vibration control is the negative impedance converter [21]. Specifically, negative capacitance has been studied widely and has shown both large amplitudes of suppression and wide bandwidth of control is a negative capacitance.

2.3.3 Negative Capacitance Shunt Control

Many researchers have demonstrated the suppression of resonant frequencies of many types of structures using a negative capacitance shunt. Forward was also the first to suggest the use of negative capacitance shunts [41]. Most of the past research focuses on the negative capacitance as “cancelling”, “compensating” or “neutralizing” the capacitance of the piezoelectric material [35, 42-45]. The argument was made that, through “cancellation” of the patch capacitance, the resistance in the negative capacitance shunt could then dissipate energy over a greater frequency range. Therefore, in most experimental work to maximize energy dissipation the negative capacitance magnitude is set to be as close as possible to the capacitance of the piezoelectric actuator to which it is attached. Because of the stability of the circuit, the negative capacitance cannot exactly equal the patch capacitance. In contrast to resonant shunt tuning, the marked advantages of a negative capacitance shunt include an increased bandwidth of control and robustness to changes in perturbation in the resonances of a structure [46, 47].

The limiting factor during implementation of the negative capacitance shunt is the stability. There are studies within the literature that have discussed the stability of the system in regards to capacitance values of the shunt that will yield stable responses. Neubauer [48] and Bisegna [49] represented the stability through the Routh-Hurwitz criterion. Bisegna also added a RC branch in parallel with the negative capacitance of the shunt to increase the system stability and to theoretically improve damping. Tang and Wang presented the stability in terms of positive definiteness of the generalized stiffness matrix [35]. A similar system stiffness stability analysis as Tang and Wang was performed by Premont [50]. Collet discussed the stability of a negative capacitance control system in terms of the wave propagation on a 1D waveguide, and noted the difference between the system stability and circuit stability [51]. Date *et al.* present a thorough electrical analysis of the stability of the realization circuit of a negative capacitance [52]. In practice, the stability of the circuit does not correspond to the predicted stable magnitude of negative capacitance. The reasons given for the discrepancy are varied with many researchers commenting on the practical "difficulties" near the system instability [47, 48, 53, 54]. Sluka *et al*. notes that the circuit analysis of Date *et al.* does not fully predict the stability of the circuit [55]. Bruneau *et. al* hypothesize that the difficulties arise from the thermal changes of the capacitance of the patch [56]. Behrens *et. al* state the capacitance is unattainable due to the vague "physical nature" of the piezoelectric patch [47]. Tang and Wang state that the limitation in attainable negative capacitance values is the current output of the operation amplifier [35].

In light of the difficulties presented above and the fact the suppression capability of the negative capacitance shunt increases exponentially as the negative capacitance magnitude becomes closer to the patch capacitance [55, 57], it is necessary to properly model the stability limitations of the circuit to accurately predict the attenuation capability of the negative capacitance shunt. If physical parameters are the limiting case, then measurements will need to be performed and included in the system or circuit stability model. Similarly, if the circuit is the limiting factor, then a thorough circuit design presents itself as the best way to increase the suppression using a negative capacitance shunt.

In contrast to the energy dissipation hypothesis, Behrens showed that the negative capacitance shunt is inherently a broadband, active feedback control means [58]. Similarly, Date, Fukado, Imoto and Kodama recognized the feedback nature of the negative capacitance shunt [59-62]. Thus, the amount of control may not correlate to the amount of energy dissipated in the shunt circuit. To determine this correlation, the power dissipated in the circuit will be compared to the suppression of vibration by the shunt.

The discussion of the negative capacitance shunt above discussed selection of the negative capacitance magnitude, but the choice in the resistance of the shunt can have equal effect on the magnitude and bandwidth of suppression. Some studies have omitted the use of a resistor in the shunt for dissipation, and relied solely on the structural damping [50, 56, 63, 64]. Some studies do not discuss the choice of resistor, or state the use of trial and error to find circuit component values for maximum suppression [42, 45, 65]. Bisegna optimized the shunt parameters to maximize the decay rate of a cantilever beam using an ad-hoc method [43]. Neubauer *et al.* developed a method to select a resistor based on the derivative of an FRF of a SDOF oscillator with respect to frequency [48]. Generally stated, the method minimizes the sum of the velocity frequency response over a narrow bandwidth surrounding the natural frequency. More complex methods that are of interest here are presented in the following section.

2.4 Negative Capacitance Tuning Theories

Four shunt selection methodologies, or tuning theories, using negative capacitance circuits that are of interest here have been presented in literature. Each shunt tuning theory seeks to optimize a certain performance function to obtain circuit impedance values that will obtain maximum control of a structure to which piezoelectric patches are bonded.

2.4.1 Control Optimization

The ability to select shunt parameters based on feedback control schemes was developed by Behrens [58]. The process begins by representing the voltage-current relationship in the Fourier domain as

$$V_Z(\omega) = I_Z(\omega) Z(\omega) \tag{2.6}$$

where Z is the shunt impedance and V_Z and I_Z are the voltage and current across the shunt. The voltage across the shunt is related to the variable voltage induced on the patch, V_P, by

$$V_Z(\omega) = V_p - \frac{1}{i\omega C_p} I_Z(\omega) \tag{2.7}$$

where C_P is the patch capacitance. Manipulation of Equation (2.6) and (2.7) yields

$$V_Z(\omega) = \frac{i\omega C_P Z(\omega)}{1 + i\omega C_P Z(\omega)} V_P(\omega). \tag{2.8}$$

If a structure with a control patch is driven with another piezoelectric patch collocated with the control patch then the control patch voltage is

$$V_P(\omega) = G_{vv}(\omega) V_{in}(\omega) - G_{vv}(\omega) V_Z(\omega) \tag{2.9}$$

where V_{in} is the driving voltage on the structure and G_{vv} is the undamped response of the structure. The transfer function relating V_P to V_{in} is found by substituting Equation (2.9) into (2.8), yeilding

$$\hat{G}_{vv}(\omega) \equiv \frac{V_P(\omega)}{V_{in}(\omega)} = \frac{G_{vv}(\omega)}{1 + G_{vv}(\omega) K(\omega)} \tag{2.10}$$

where

$$K(\omega)=\frac{Z(\omega)}{Z(\omega)+\frac{1}{i\omega C_P}}\,. \tag{2.11}$$

Using a similar process, it can be shown that the transfer function relating the transverse displacement of the structure, $W(x,\omega)$, to the input voltage is

$$\hat{G}_{wv}(x,\omega)\equiv\frac{W(x,\omega)}{V_{in}(\omega)}=\frac{G_{wv}(\omega)}{1+G_{vv}(\omega)K(\omega)}\,. \tag{2.12}$$

It can be seen from Equations (2.10)-(2.12) that the use of a shunted piezoelectric transducer is a feedback control application. Therefore, selection of the shunt parameters can be found through the use of control optimization techniques.

The process to find the shunt impedance begins with substituting Equation (2.11) into (2.10) and rearranging to find the damped response of the structure,

$$\hat{G}_{vv}(\omega)=\frac{G_{vv}(\omega)\left(i\omega C_P Z(\omega)+1\right)}{i\omega C_P Z(\omega)\left(1+G_{vv}(\omega)\right)+1}\,. \tag{2.13}$$

The damped response of the structure can be set to its minimum by setting the numerator of Equation (2.13) to zero. This is possible by selecting the impedance of the shunt to be purely capacitive,

$$Z(\omega)=-\frac{1}{i\omega C} \tag{2.14}$$

and setting C to equal C_P. Unfortunately, this electrical circuit cannot be created because it produces an undamped electrical resonance. To overcome this, a resistor can be place in series with the capacitance. The full shunt impedance is expanded to become

$$Z(\omega)=\frac{i\omega RC-1}{i\omega C}\,. \tag{2.15}$$

Substituting Equation (2.15) into the expression for the controller *K*, Equation (2.11) becomes

$$K(\omega) = \frac{i\omega - \frac{1}{RC}}{i\omega + \frac{1}{RC}\left(\frac{C}{C_P} - 1\right)}. \tag{2.16}$$

The capacitance of the shunt circuit must be greater than the patch capacitance in order for the controller *K* to be stable. For selection of shunt parameters, the negative capacitance is set to a value slightly higher than the capacitance of the shunt to allow for frequency variations in the piezoelectric material capacitance. For the resistance value, Behrens employs a minimization approach: a line search algorithm is used to minimize the $\mathcal{H}_2$ norm of the first five structural modes of vibration [58].

2.4.2 Maximum Dissipated Power

Kim and Jung developed a method based on the maximum dissipated energy similar to methods used for resonant shunts [66]. For this method, the electrical impedance of the patch and shunt, and structural impedance are represented as an equivalent electrical circuit at each resonant frequency. This equivalent circuit model, the Van Dyke model, is shown in Figure 2.4, where C_0 is the inherent piezoelectric capacitance of the patch, and L_1, R_1, and C_1 are the mass, damping, and compliance of the structure. To determine these electrical parameters, an impedance analyzer is used to measure the conductance and susceptance for the structure at each of the resonant frequencies of interest. Thus, a different Van Dyke model must be created for each resonance. The total impedance of the system can be then written as

$$Z = Z_1 + \frac{Z_2 Z_3}{Z_2 + Z_3}. \tag{2.17}$$

The impedance Z_1 represents the structure with the form

$$Z_1 = i\omega L_1 + R_1 + \frac{1}{i\omega C_1} \tag{2.18}$$

and Z_2 is equal to the impedance of the patch

$$Z_2 = \frac{1}{i\omega C_0}. \tag{2.19}$$

Lastly, Z_3 equals the shunt impedance, Z_{sh}.

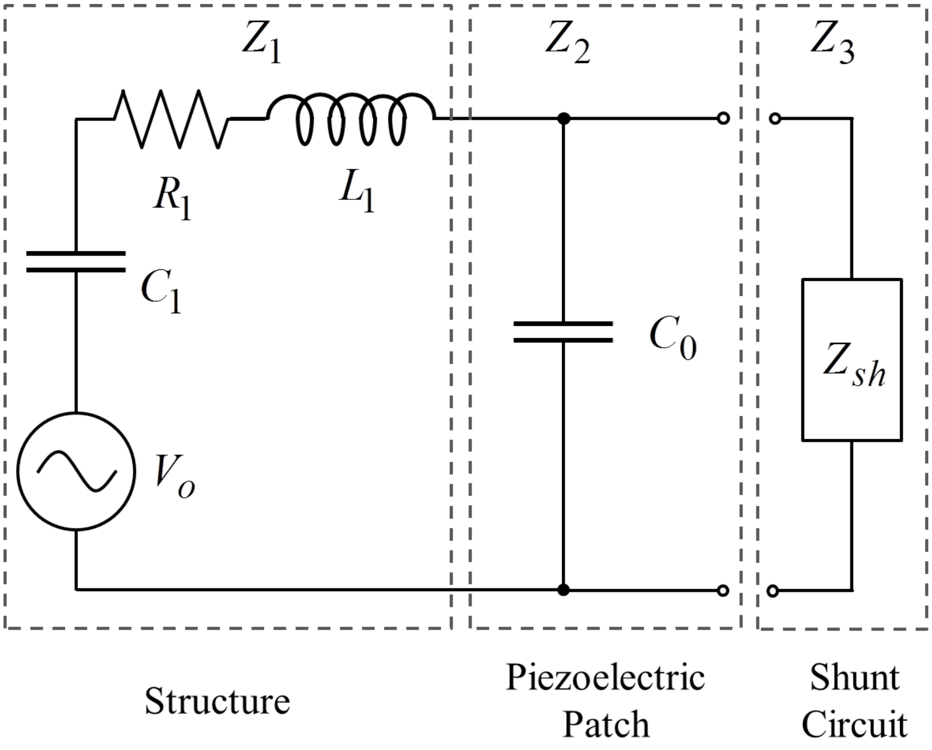

Figure 2.4 - Van Dyke's electrical impedance model for a vibrating structure with attached piezoelectric patch [66]

From the measured impedance values, the shunt parameters can be optimized by computing the maximum dissipated energy. For the full system, the power dissipated is normalized by the input power,

$$J = \frac{P_D}{P_{in}} = \frac{\mathrm{Re}\left(Z_3\right)\cdot\left|\left(\frac{Z_2}{Z_2 + Z_3}\right)\right|^2}{|Z|}\,. \tag{2.20}$$

This power ratio can be computed for each resonance. The optimal shunt parameters would be found for an average of *J* over a specified frequency bandwidth. For a negative capacitance shunt, the capacitance is set to be equal to the negative of the capacitance measured by the impedance analyzer. The resistor of the shunt is determined by maximizing the power ratio

$$\left[R^*\right] = \underset{R}{Max}\left[\frac{1}{n}\sum_{k=1}^{n}\left|J_k\right|\right] \tag{2.21}$$

over the frequency range, or number of resonances, from *n* = 1 to *k*.

2.4.3 Wave Tuning

The focus of the wave tuning method developed by Park and Palumbo is on the minimization of the reflected wave at the edge of a piezoelectric patch to suppress the vibration field on a beam [11]. The vibration field is separated into a traveling component and an evanescent component. The goal is to minimize the reflected wave component using a shunt impedance. This minimization leads to an optimal design for the shunt impedance. This process is done by analyzing a beam, shown in Figure 2.5, with a complex shunt network connected to patches bonded to the beam at the root. Following the developments of Park and Palumbo [11] and Cunefare [67] the transverse displacement of the beam is expressed as

$$\hat{w}(x) = \hat{w}_1(x)(1 - H(x)) + \hat{w}_2 H(x) \tag{2.22}$$

where

$$\hat{w}_1 = \hat{C}_{11}e^{-ik_1(x+L)} + \hat{C}_{12}e^{-ik_1 x} + \hat{C}_{13}e^{-k_1(x+L)} + \hat{C}_{14}e^{-k_1 x} \tag{2.23}$$

$$\hat{w}_2(x) = \hat{C}_{21}e^{-ik_2 x} + \hat{C}_{22}e^{ik_2 x} + \hat{C}_{23}e^{-k_2 x} \tag{2.24}$$

and *H(x)* is the Heaviside function. The vibration field is split into two regions; the region under the patch, Region 1, and the beam excluding the patches, Region 2. These regions are displayed in Figure 2.6, with the complex reflected and incident wave amplitudes, $\hat{C}_{ij}$, for the traveling and evanescent waves in each region. The index *i* is used to indicate in which region the wave is located, and the index *j* indicates the specific wave component in the regions. There are four wave components on the beam under the patch, and only three adjacent to the patch; the incident and reflected traveling waves and a single reflected evanescent wave. There is no incident evanescent wave next to the patch because it is assumed that the patches are far enough from the free end of the beam that its amplitude is negligible. The wave numbers k_i are given in each region by

$$k_i = \left(\frac{\omega^2 M_i}{D_i}\right)^{1/4} \tag{2.25}$$

where M_i and D_i are the mass per unit length and bending stiffness of the beam.

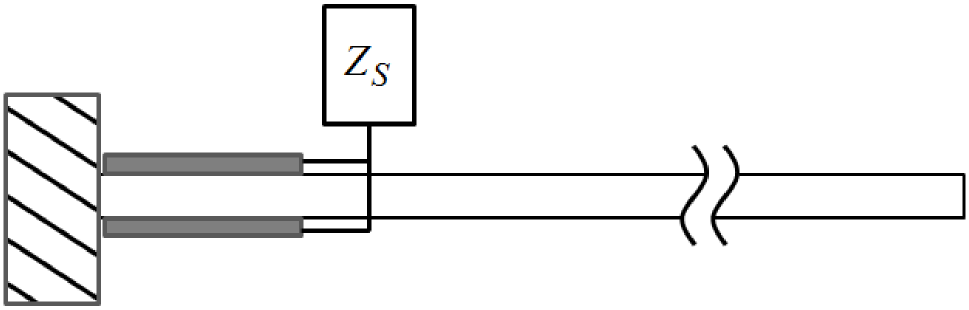

Figure 2.5 - Cantilever beam with shunted piezoelectric patches bonded to the beam at the root.

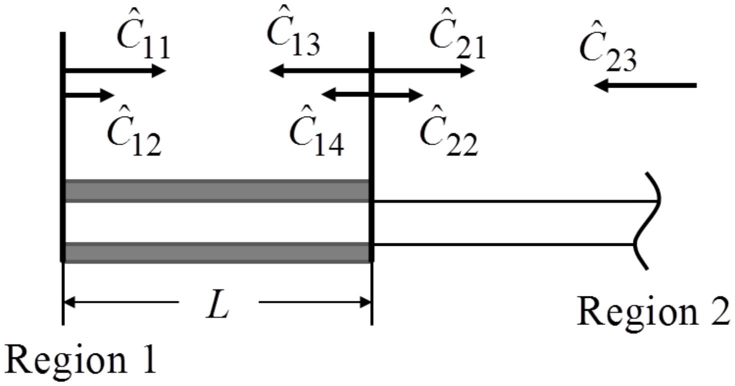

Figure 2.6 - Vibration field decomposition at patch and adjacent to patch.

Park and Palumbo [11] defined the dissipation as

$$Dissipation(\%) = \left(1 - \frac{\left|\hat{C}_{21}\right|^2}{\left|\hat{C}_{22}\right|^2} \right) \times 100 \tag{2.26}$$

which may be physically interpreted as the fraction of incident energy that does not reflect off the impedance boundary between Region 1 and 2. The term dissipation does not encompass the complete effect of the shunt because the shunt does not merely add damping. Instead, using a shunt to minimize Eq.(2.26) will reduce the amplitude of the reflected wave, thereby minimizing the amplitude of the vibration on the beam outside the patch.

The optimal shunt impedance is found by minimization of the function

$$f\left(Z_S, \omega\right) = \frac{\left|\hat{C}_{21}\left(Z_S, \omega\right)\right|^2}{\left|\hat{C}_{22}\left(Z_S, \omega\right)\right|^2}. \tag{2.27}$$

The maximization of Equation (2.26), the dissipation function, is equivalent to the minimization of Equation (2.27). Park and Palumbo found that the greatest dissipation required a negative capacitance element for a single shunt configuration in the frequency range of interest [11]. Although Park and Palumbo used an RLC shunt architecture, there is no requirement that a shunt needs to contain an inductive element but it was included for impedance matching over a wider frequency range. In Park and Palumbo's simulation, the tuned frequency was completely suppressed, but as the shunt impedance diverged from optimal the vibration suppression decreased [11]. This frequency dependence can be eliminated by the use of a strictly RC circuit.

2.4.4 Minimum Reactive Input Power

Physically, Cunefare [67] linked the reduction of reflected wave energy to the reduction of reactive input power. A standing wave field on a beam created by a point force is reduced when the reflected wave component is suppressed. The standing wave is reactive in nature because there is no net average energy flow on the beam in the absence of damping when the wave field on the beam is purely standing. This occurs when the reflected component is equal to the incident component. Therefore, a reduction of the reflected wave, and thus the standing wave, will reduce the reactive power input of the point force. In other words, the impedance of the input is controlled through the application of a wave tuned shunt.

This concept can also be investigated by using the wave decomposition notation of Park and Palumbo [11] on the beam system of the previous section, Figure 2.6. Considering only Region 2, the transverse displacement is

$$w_2\left(x\right) = \hat{C}_{21}e^{-ik_2x} + \hat{C}_{22}e^{ik_2x} + \hat{C}_{23}e^{-k_2x} . \tag{2.28}$$

This expression can be reduced to two terms by only considering the travelling wave components,

$$\hat{w}_2\left(x\right) = \hat{C}_{21}e^{-ik_2x} + \hat{C}_{22}e^{ik_2x} . \tag{2.29}$$

The wave field on the beam can also be expressed in terms of a standing wave and a propagating wave. The standing and propagating waves can be separated from each other through manipulation of Eq. (2.29) which is expressed as

$$\hat{w}_2\left(x\right)=\left(\hat{C}_{22}-\hat{C}_{21}e^{i\beta}\right)e^{ik_2x}+2\hat{C}_{21}e^{i\beta}\cos k_2x \tag{2.30}$$

where the first term is the propagating wave component and the second is the standing wave. The phase between the $\hat{C}_{21}$ and $\hat{C}_{22}$ wave terms is β. Depending on the phase angle between wave terms, the propagating wave can be totally suppressed leaving the only the standing wave component. In contrast, if the reflected wave $\hat{C}_{21}$ is reduced to zero then the standing wave component of vibration is eliminated. The total response of the beam would only contain the incident travelling wave component.

Extending the concept of how the standing wave is linked to the reactive input power, the total instantaneous power delivered to the beam by a point force is

$$\hat{W}\left(t\right)=\left[F\left(\hat{C}_{22}-\hat{C}_{21}e^{i\beta}\right)e^{ik_2x_F}+2F\hat{C}_{21}e^{i\beta}\cos k_2x_F\right]e^{j\omega t}\,. \tag{2.31}$$

This expression does omit the power that generates evanescent waves, which are assumed to be small. The first term in the brackets is proportional to the real input power and the second term is proportional to the reactive input power. Taking into account the discussion of the wave tuning method, specifically the suppression of the standing wave component and the minimization of Eq. (2.27), the minimization of $\hat{C}_{21}/\hat{C}_{22}$ will achieve the equivalent vibration suppression as by suppressing the reactive input power. In general, it is evident that the wave tuning method proposed by Park and Palumbo is a type of input impedance control.

The application of the above does not fully address the vibration throughout the entire length of the beam. The derivation only applies to the section of the beam between the driving force and the patch location. Therefore, this approach suits the case when the input force is located at the tip of the beam, but does not verify that the same result will occur when the driving force is at an intermediate point. There may or may not be a suppression of vibration on the area of the beam opposite the shunted patch, yet if a minimization of the standing wave field causes a global reduction in the vibration amplitude the theory would apply to all areas of the beam. Specifically, if the beam is highly resonant then the vibration field will be dominated by the standing wave field; therefore a suppression of the reactive power would decrease the vibration amplitude globally.

Since both the wave-tuning and power minimization tuning can be shown to suppress the reactive standing wave field, then their resulting tunings should be identical.

2.5 Periodic Structures

As discussed in Chapter 1, periodic structures are to be utilized to alter the wave propagation on a structure, and in turn increase the control performance of the negative capacitance shunt. Periodic structures are structures that consist of repeated identical mechanical elements. Some of the periodic structures studied for their wave modification include periodic stiffened beams and plates [68, 69], shape memory allow inserts [70] and periodic piezoelectric structures [20, 51, 71]. The work of Brillouin is the basis for most of the resent research in periodic structures [72]. Wave propagation studies in this work considered the propagation constant μ defined as

$$\mu = \delta + i\varepsilon \tag{2.32}$$

where the attenuation constant δ and a phase constant ε characterize the effect as a wave travelled through a periodic structure. Periodic structures demonstrate "stop-bands" and "pass-bands" which either reduce or allow wave propagation. The "stop-band" frequencies correspond to positive attenuation propagation constant. The frequency behavior of the propagation constant can be seen in Figure 2.7 where *S* labels the stop bands and *P* labels the pass bands. To obtain the values for the propagation constants, a Bloch theorem analysis is performed on a unit cell of the period structure. From the continuity of the unit cell's boundary condition, the propagation constants can be solved for by a wave-number integration of the equations of motion of the unit cell.

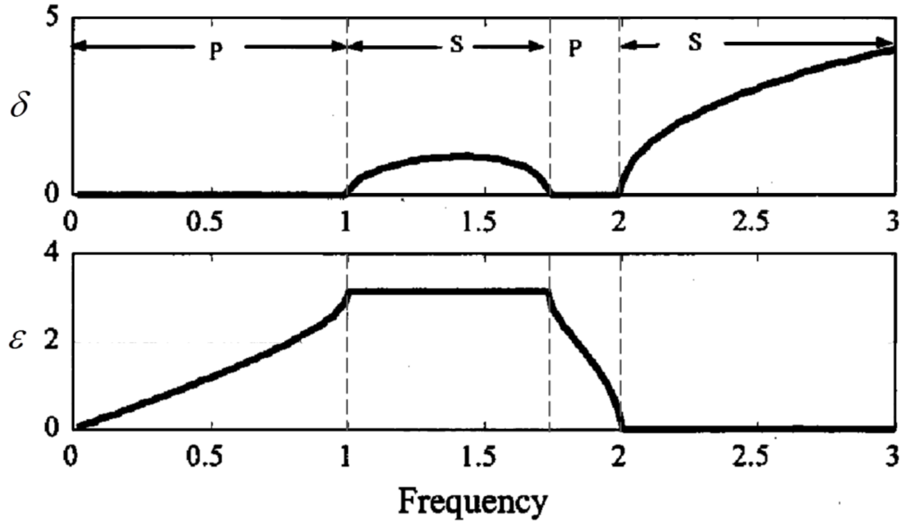

Figure 2.7 - Stop "s" and pass "p" bands [73]

The elements within periodic structures therefore can be modified to increase the "stop-band" frequency bandwidth [73] which enhances vibration control over a greater frequency range. If the periodic structure is a piezoelectric patch array, typical piezoelectric patch control methods can be used. The change in effective material properties of the piezoelectric elements can be controlled to tailor the "stop-band" bandwidth and magnitude through shunt design. The use of shunts to control periodic arrays can either be designed where a single circuit controls a single patch which mimics a SISO control system or where the shunt circuitry couples the piezoelectric patches to form a single control system.

For transverse motion, bladed disks have been a common test structure [74-76] to analyze the use of shunts to control periodic structures. Anges [74] presented a method to control vibrations of a bladed-disk assembly by coupling the blades through piezoelectric patches to reduce mode localization. His work was extended to increase control through more complex circuitry [75-78]. Baz and Thorp *et al.* introduced the concept of active piezoelectric arrays on a linear waveguide [14, 73]. Their work demonstrated that by applying a resonant shunt to a vibrating rod with a piezoelectric array the stop-bands of the system could be made significantly more broadband and while also increasing the magnitude of the attenuation constant within the stop-band. Figure 2.8 illustrates an example of a resonant shunt altering the attenuation constant of a system. A resonant shunt tuned to 1575 Hz creates a high magnitude stop band at 1575 Hz. Most of the later work on shunted periodic arrays has focused on resonant shunts to frequency tune the bandwidths of attenuation [19, 20, 79-84]. Yet, due to the narrowband nature of a resonant shunt, there are stop-band bandwidth limitations. To increase the bandwidth, it is possible to apply negative capacitance shunts to periodic arrays.

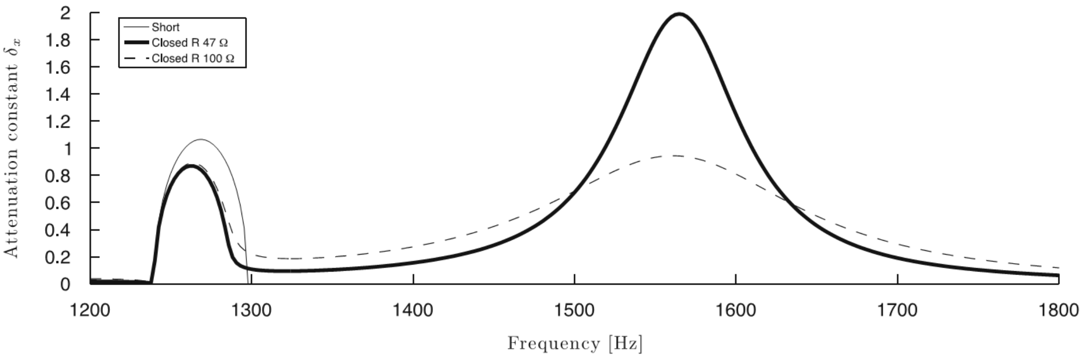

Figure 2.8 - Attenuation constant for a resonant shunt to tuned to 1600 Hz [84]

There has been limited work performed with negative capacitance shunts attached to periodic arrays for suppression of vibration. Bisegna *et al.* performed a numerical analysis of periodic piezoelectric array with negative capacitance shunts that were coupled using resistors [85]. They presented an optimization of single mode and multiple modes of a finite beam with five patches. The metric of their results was in terms of exponential time decay rates, but did not discuss reduction in peak response of resonant modes. Similarly, there was no mention of wave propagation effects and the changes in stop- and pass-band behavior. Collet *et al.* performed a wavenumber and power flow analysis of a beam with a periodic array shunted with negative capacitance shunts [51]. The authors investigated the negative capacitance shunt parameters with respect to wave reflection and transmission. Yet, no experimental validation was performed. The work of Sheng-Bing *et al*. investigated the changes to the frequency location of the stop-bands of a periodic piezoelectric array versus negative capacitance magnitude [63]. Their results show the ability of a negative capacitance shunt to alter the stop-bands to any frequency of interest and significantly increase or decrease the stop-bandwidth. The negative capacitance shunt they simulated did not include a resistor, which limited the design space. Just as with the other two investigations of negative capacitance shunts on periodic arrays, no experimental assessments of vibration reduction was performed.

2.6 Summary

This literature review has presented where the negative capacitance shunt method fits within other piezoelectric control methods for flexural systems. Passive shunts utilize the piezoelectric coupling to modify stiffness and damping of the piezoelectric material, in turn reducing the vibration of the bonded substrate. Active methods use powered devices to actively control the motion of the vibrating structure. Negative capacitors have been shown to be a simple active control architecture. Four current negative capacitance shunt techniques were presented. Finally, a short overview of periodic structures relevant to use of negative capacitance as elements of the structure was given.

CHAPTER 3

MODELING

3.1 Introduction

Numerical models are utilized to investigate the effects of shunt control on the structures of interest in this work. A one- or two-dimensional vibrating system may be modeled numerically many ways; two methods of interest here are the method of assumed modes and the finite element method. A limitation of the method of assumed modes is that it uses the basic variable stiffness approximation of Equation (2.3) to compute the stiffness of the piezoelectric element in one dimension, which limits the accuracy of the electrical degrees of freedom of the system. Therefore, the method of assumed modes is used to analyzer a thin cantilever beam to explore basic shunt behavior and the effect of a shunt on the response of a simple system. The finite element method allows for a more complete model of the electrical properties of the piezoelectric patches. More complex geometries and shunt impedances can also be modeled using the finite element method, which would otherwise be cumbersome to implement using an assumed mode method. The method of assumed modes for a beam is presented first. The finite element method derivation follows, and includes the method to solve for the response of a complete structural system and to solve for the wave propagation effects of a periodic system.

3.2 Method of Assumed Modes

The flexural dynamics of a system such as the system depicted in Figure 2.2 consisting of a substructure with any number of piezoelectric patches bonded to its surface can be solved by developing a matrix representation of the equations of motion in the form

$$[M]\{\ddot{q}\}+[K]\{q\}=\{f\} \tag{3.1}$$

where the mass and stiffness matrices, M and K respectively, are considered a combination of the components from the beam and patch individually and q is the vector of generalized coordinates and f is a vector of generalized forces. As stated in the introduction, the method of assumed modes will be used to analyze a cantilever beam which reduces the geometric complexity to a general single dimensional system as shown in Figure 3.1. To solve for the transverse displacement, the method of assumed modes relates the displacement $w(x)$ to a set of basis functions φ

$$w(x,t)=\sum_{i=1}^{N}\varphi_i(x)q_i(t)=\{\varphi\}^T\{q\} \tag{3.2}$$

where the N is the total number of basis functions chosen. Using a Lagrange formulation [11], the stiffness matrix is found to be

$$[K]=[K_p]+[K_b] \tag{3.3}$$

where

$$k_{ij,p}=\int_{L_p} D_p(x)\varphi_{xx,i}(x)\varphi_{xx,j}(x)dx \tag{3.4}$$

and

$$k_{ij,b}=\int_0^{L_b} D_b(x)\varphi_{xx,i}(x)\varphi_{xx,j}(x)dx \tag{3.5}$$

are the individual elements of the stiffness matrices. For all constants, the subscripts "*p*" and "*b*" denote *patch* and *beam*, respectively. The integrals are performed over the length of the patch L_p and beam L_b. The bending stiffness of the beam is

$$D_b = \frac{E_b b h_b^3}{12} \tag{3.6}$$

and of the patches

$$D_p = \frac{E_p b\left[\left(2h_p + h_b\right)^3 - h_b^3\right]}{12} \tag{3.7}$$

if the patches are placed symmetrically on opposite sides of the beam with the same thickness, h_p, where E is the elastic modulus and b is the width of both the beam and patch. Similarly, the mass matrix is the sum

$$[M] = \left[M_p\right] + \left[M_b\right] \tag{3.8}$$

where the individual components are

$$m_{ij,p} = \int_{L_p} m_p(x)\varphi_i(x)\varphi_j(x)dx \tag{3.9}$$

and

$$m_{ij,b} = \int_0^{L_b} m_b(x)\varphi_i(x)\varphi_j(x)dx \tag{3.10}$$

where the mass density is m_b and m_p. The advantage of constructing the stiffness and mass matrices in this way is the ease in which the stiffness of a patch with an arbitrary shunt admittance may be calculated. The patch stiffness for shunt admittance Y_S is

$$\left[K_p(Y_S)\right] = \left[K_p(Y_o)\right]\frac{E(Y_S)}{E(Y_o)}. \tag{3.11}$$

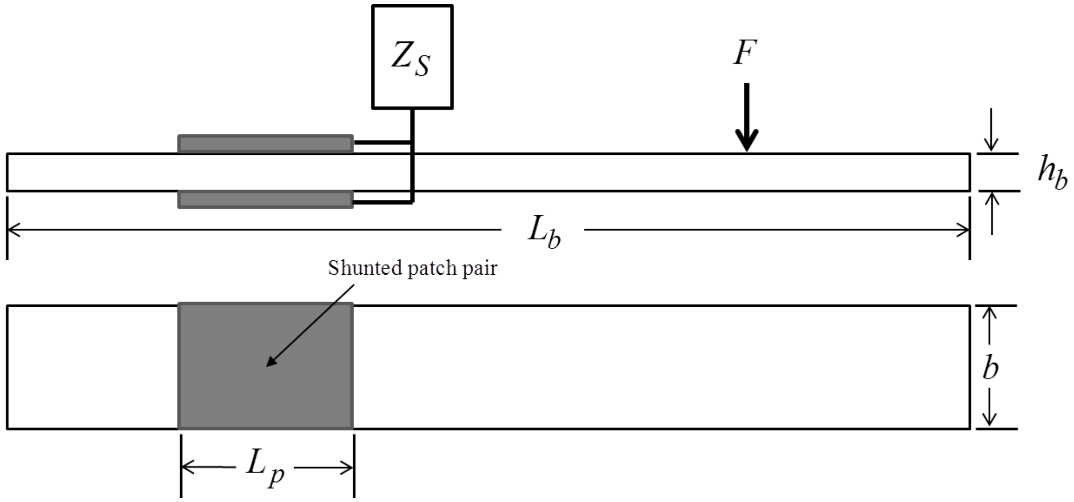

Figure 3.1 - Arbitrary beam with shunted patch pair

Using the above formulation, the response coefficients of the assumed modes of the beam can be solved from

$$\{q\} = [D]^{-1}\{f\} \tag{3.12}$$

where the dynamic stiffness is

$$[D] = -\omega^2[M] + [K]. \tag{3.13}$$

The basis functions $\varphi_i(x)$ used to compute the individual components of the matrices for the cantilever beam are

$$\varphi_i(x) = x^{i+1}. \tag{3.14}$$

The transverse displacement can therefore be calculated using Equation (3.2). Because of the response is harmonic, the velocity or acceleration can be calculated easily.

To assess the effect of a shunt on the motion of the beam, the velocity response is computed for the case when there is infinite shunt impedance representing the open circuit case. The open case is considered the uncontrolled response. The uncontrolled response can therefore be compared to the calculated response when a shunt with arbitrary impedance is applied.

3.3 Finite Element Method

The following finite element derivation is a generic formulation that will be applied to a variety of structures. Likewise, the formulation is robust to geometry or forcing. The boundary conditions for specific geometries will be presented with the results in later sections or chapters. The finite element derivation of the equations of motion for a thin vibrating system with an applied patch and shunt is based on the work done by Casadei et al. [19] and Spadoni et al. [20]. The principle of virtual work

$$\delta L_{tot} = \delta L_{ext} - \delta L_{def} = 0 \tag{3.15}$$

is first applied to an arbitrary piezoelectric structure shown in Figure 3.2. The total work, δL_{tot}, is the difference of the work by external and internal forces and the work done by virtual deformation. Rewriting Equation (3.15) in terms of virtual displacement δu_i and potential $\delta\phi$ functions and arbitrary space-variables yields

$$\int_{V_s} \delta\varepsilon_{ij}\sigma_{ij,j} - \delta u_i \rho \ddot{u}_i + \delta\phi D_{i,i} dV = \int_{S_f} \delta u_i \bar{f} dS - \int_{S_q} \delta\phi \bar{q} dS \, . \tag{3.16}$$

The forcing terms of Equation (3.16) include the mechanical dynamic forces, $\bar{f}_i$, and the imposed electric charges, $\bar{q}$, which are both defined along the system boundaries, S_f and S_q. The term u_i is the mechanical displacement which is defined over the structural domain V_S. The piezoelectric constitutive Equations (2.1) and (2.2) are needed to obtain the electrical displacement D_i and the stress tensor σ_{ij} in terms of linear strain ε_{kl} and electric potential ϕ. The constitutive relations are substituted into

Equation (3.16) to yield the governing equations which are obtained through integration by parts,

$$\int_{V_S} \delta\varepsilon_{ij}\left(c_{ijkl}\varepsilon_{kl} + e_{kij}\phi_k\right)dV + \int_{V_S} \delta u_i \rho \ddot{u}_i dV = \int_{S_f} \delta u_i \overline{f}_i dS \tag{3.17}$$

and

$$\int_{V_S} \delta\phi_{,i}\left(e_{ikl}\varepsilon_{kl} - \xi_{ik}\phi_{,k}\right)dV = -\int_{S_q} \delta\phi\overline{q}dS\ . \tag{3.18}$$

Also, the strain field can be expressed in terms of the displacement variables with the use of the gradient equation

$$\varepsilon_{ij} = \frac{1}{2}\left(u_{i,j} + u_{j,i}\right). \tag{3.19}$$

The Kirchhoff kinematic assumptions for thin plate behavior are then applied which state

$$u_1 = -zw\left(x,y\right)_x,\ u_2 = -zw\left(x,y\right)_y,\ \text{and}\ u_3 = w\left(x,y\right) \tag{3.20}$$

where *w* is the transverse displacement of the mid-surface of the beam. These conditions result in a plane strain state where the only non-zero components of strain are ε_{11}, ε_{22} and γ_{12}.

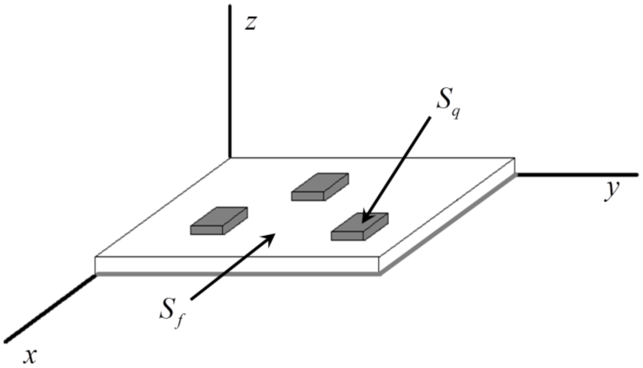

Figure 3.2 - 2D structure with bonded piezoelectric patches

3.3.1 Full System Response

The solution to the governing equations of a full system can be found by applying a Kirchhoff plate finite element discretization. The use of shape functions and nodal degrees of freedom gives the vertical displacement and surface potential,

$$w = \left[N_w\right]\left\{d\right\} \tag{3.21}$$

and

$$\phi = \left[N_\phi\right]\left\{\phi\right\} \tag{3.22}$$

where N_w and N_ϕ are the shape functions. A pair of matrix equations of motion is obtained by substituting Equations (3.21) and (3.22) into Equations (3.17) and (3.18) yielding

$$\left[M_{uu}\right]\left\{\ddot{d}\right\} + \left[K_{uu}\right]\left\{d\right\} + \left[K_{u\phi}\right]\left\{\phi\right\} = \left\{f\right\} \tag{3.23}$$

and

$$\left[K_{\phi u}\right]\left\{d\right\} + \left[K_{\phi\phi}\right]\left\{\phi\right\} = \left\{q\right\}. \tag{3.24}$$

The system mass and stiffness matrices are found using the shape functions and material properties; refer to the work of Cook for exact equations [86].

To obtain one equation of motion combining both electrical and mechanical degrees of freedom, Equations (3.23) and (3.24) are coupled by application of piezoelectric assumptions and a shunting matrix. To start, the electric field at any point on the surface of a piezoelectric patch is considered constant. Also, the electric field potential is assumed to vary linearly through the thickness of a patch. These two assumptions simplify the electrical equation of motion to a scalar equation, for each patch,

$$\left[K_{u\phi}\right]^T \{d\} + K_{\phi\phi}\phi_p = q_e . \tag{3.25}$$

The shunting matrix is found by recognizing that the electric potential can be expressed in terms of the charge when an arbitrary impedance is connected across the patch electrodes. Assuming a harmonic response, the electric potential is

$$\phi_{P_0} = i\omega Z_e(\omega) q_{e_0} \tag{3.26}$$

where Z_e is the shunt impedance. Therefore, combining Equations (3.23) and (3.25) produces

$$\left[[K_{uu}] - \omega^2 [M_{uu}] + \left[S_{Z_e}(\omega)\right]\right]\{d_0\} = \{f_0\} \tag{3.27}$$

which is the single harmonic motion equation where the shunting matrix is

$$\left[S_{Z_e}(\omega)\right] = i\omega\left[K_{u\phi}\right]\left(i\omega K_{\phi\phi} - \frac{1}{Z_e(\omega)}\right)^{-1}\left[K_{\phi u}\right]. \tag{3.28}$$

Through the introduction of capacitance, resistance, and inductance, an electrical shunt allows for modification of the stiffness, mass, and damping of the system depending on the selection of shunt and patch parameters. This formulation will be used to compute the velocity frequency response of a complete vibrating system at each node of the finite element model. The driving disturbance can be modeled as a transverse point, line or area source, or a moment which approximates the disturbance caused by an electrically driven patch actuator.

3.3.2 Dispersion Analysis

As stated earlier, the implementation of a periodic array will modify which wave frequencies will propagate through a structure. To study this physical behavior, the use of a Bloch Theorem analysis is applied to a single repeated periodic cell [72]. The cell's motion can be found using the above finite element formulas by solving the equation of motion

$$\left[\left[K_{uu}\right]-\omega^2\left[M_{uu}\right]+\left[S_{Z_e}\left(\omega\right)\right]\right]\{d\}=\left[K_D\left(\omega\right)\right]\{d\}=\{f\} \tag{3.29}$$

where $\left[K_D\right]$ is the dynamic stiffness of the element with an applied electrical shunt. Because the cell is periodic, the displacement and forcing at the boundaries of the cell must be continuous from one cell to the next with respect to the wave number. To determine the attenuation of the propagating wave, the wave number must be solved for where the real part of the wave number represents attenuation. To begin, the equations of motion are rewritten in terms of the wave number,

$$\left[K_D\left(\mu_x,\mu_y,\omega\right)\right]^{(r)}\{d\}^{(r)}=0 \tag{3.30}$$

where μ_x and μ_y are the *x* and *y* components of propagation constant. The solution to this equation is found by holding the frequency and one wave number component constant while solving for the second term, which is equivalent to varying the wave number vector along the contour of the first irreducible Brioullin zone [20]. Because of the symmetry of the unit cell, the frequency wave number period is square as shown in Figure 3.3. The real positive term that enumerates attenuation is called the propagation constant, *δ*.

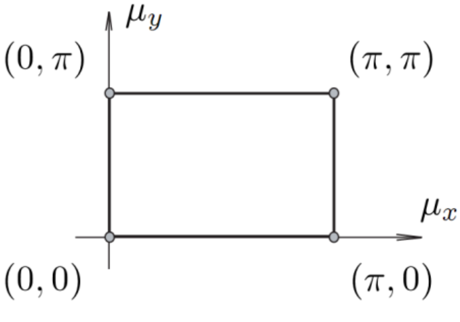

Figure 3.3 - Sketch of the first irreducible Brioullin zone

3.4 Summary

Two methods of modeling a vibrating flexural system with shunted piezoelectric elements were presented. The method of assumed modes is used only for initial investigation of the dynamics of a cantilever beam because of the assumptions made for the modulus of the piezoelectric material when a shunt is connected. The finite element method is used to create a system of equations for both a full dynamic system and a unit cell of a periodic structure. The unit cell is employed to solve for the wave propagation effects of a negative capacitance shunt using a Bloch Theorem analysis.

CHAPTER 4

NEGATIVE CAPACITANCE EFFECT, IMPLEMENTATION, AND TUNING THEORY COMPARISON

4.1 Introduction

The negative capacitance circuit within both the electrical and mechanical domains is difficult to conceptualize. Therefore the effects of shunts on the piezoelectric material properties, with an eye toward negative capacitance, are presented to illustrate the frequency behavior. The following section presents the method of experimental implementation of a negative capacitance, both how to build a circuit and how to apply it in practice. Next, a comparison between two shunt tuning methods is presented along with an experimental assessment of experimentally obtainable shunt values.

4.2 Effect on Piezoelectric Material Properties

The various passive shunting techniques presented in Section 2.3.1 take advantage of the modification of the piezoelectric material properties given by Equation (2.3), repeated here

$$E_p^{SU}(\omega) = E_p^E \, \frac{i\omega C_p^T + Y_S}{i\omega C_p^T (1 - k_{31}^2) + Y_S} \,. \tag{4.1}$$

This section outlines the how resistive and negative capacitive circuits modify the stiffness and damping. Even though the negative capacitance shunt is an active controller, the analysis on the material properties can be performed similar to passive shunts. Given typical piezoelectric control patch geometry and material properties, shown in Table 4.1, the modulus of the shunted piezoelectric element can be normalized to express the stiffness and loss moduli as non-dimensional quantities. The normalized stiffness ratio is defined as

$$\kappa = E_d \Big/ E_p^E \tag{4.2}$$

and the normalized loss factor ratio as

$$\eta = E_l \Big/ \left| E_d \right| \tag{4.3}$$

where the stiffness modulus E_d and loss modulus E_l are the real and imaginary parts of shunted modulus, E_p^{SU} . The use of the absolute value of E_d in the denominator is required so as to retain the sign of the loss modulus if the stiffness becomes negative. These definitions are consistent with the works of Hagood and von Flotow [10] and Park and Park [65]. These ratios are introduced for ease of plotting, along with their correlation to the control-ability of a shunted piezoelectric sensoriactuator. Just as shown in Equation (2.5), the relationship between the open circuit and short circuit modulus is

$$\kappa^E = \kappa^D \left(1 - k_{31}^2\right) \tag{4.4}$$

where superscript *E* and *D* denote short and open circuit respectively. Since the coupling coefficient is less than one, the open circuit stiffness is larger than short circuit stiffness.

Table 4.1 - Physical parameters of piezoelectric PZT-5A

Young's modulus, shorted	E_p=63 GPa
Coupling coefficient	k_{31}=0.31
Capacitance C_p^T	116 nF

Figure 4.1 presents the modulus ratios as a function of frequency for three values of a purely resistive shunt impedance. Inherently, the impedance of a resistor as a shunt is

not frequency dependent but the modulus ratios are expressed versus frequency because of the nature of the stiffness and damping, Equation (4.1).

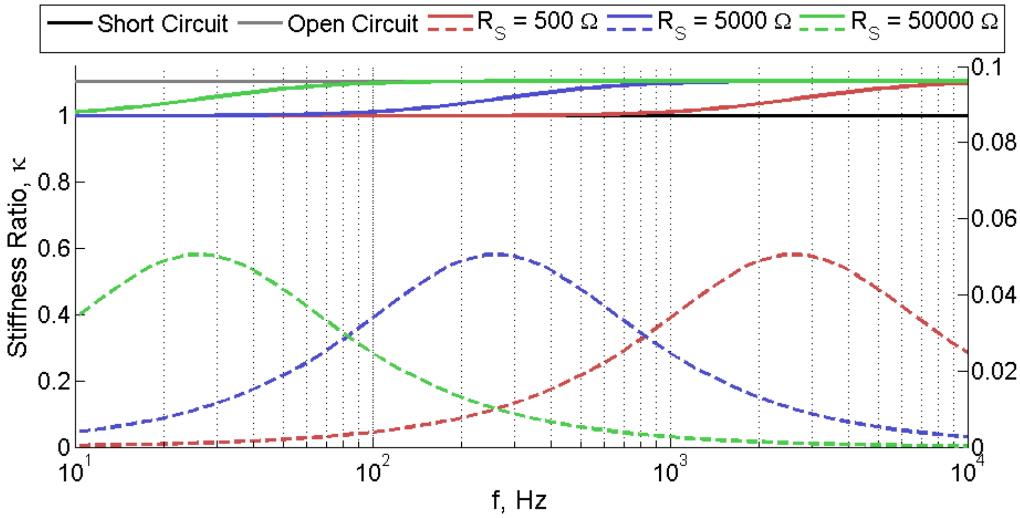

Figure 4.1 - Stiffness modulus ratio κ (solid line), and loss modulus ratio η (dashed line) versus frequency for three pure resistor shunt values

To begin the analysis of the effects of the shunt on the material, consider the 5000 Ω resistor: the stiffness is equal to the short circuit value for low frequencies, equals the open circuit stiffness at high frequencies, and transitions from short circuit to open circuit stiffness in the bandwidth between. This frequency-dependent behavior is consistent with the behavior of the stiffness modulus ratios for the two other resistor values shown in Figure 4.1, but the difference in the effect is at which frequency the transition occurs and the bandwidth of the transition which are proportional to frequency. For larger values of resistance, the shift from short circuit stiffness to open circuit stiffness occurs at lower frequencies and has a smaller bandwidth. Similar behavior is seen in the loss modulus ratio for the three values of resistance with increasing frequency and bandwidth. For all resistances, the loss modulus ratio peaks within the transition frequencies from short to open circuit stiffness. The maximum value of the loss modulus ratio is the same for each resistance, therefore, there is no advantage in increasing or decreasing the shunt resistor for more control apart from targeting a specific frequency and bandwidth: the maximum loss modulus ratio is 0.05. This value of loss factor 5 times larger than the inherent material loss factor of PZT-5A, but is still quite low.

It can be found that when a capacitor is attached to the piezoelectric element, the stiffness modulus ratio is independent of frequency,

$$\kappa = \frac{C_p^T + C_S}{C_p^T\left(1 - k_{31}^2\right) + C_S}. \tag{4.5}$$

Similarly, there is a zero loss modulus ratio for all frequencies because there is no imaginary term of the shunted stiffness associated with a capacitance shunt. Through inspection, the stiffness modulus can vary between the open circuit and short circuit conditions, depending on the magnitude of capacitance. Yet, if one allows the capacitance to have a negative value, the stiffness modulus ratio can achieve any desired value. Figure 4.2 shows how the stiffness modulus ratio changes versus the negative capacitance ratio

$$NCR = -\frac{C_S}{C_p^T}. \tag{4.6}$$

The stiffness modulus ratio is equal to the short circuit stiffness for large values of NCR and equal to the open circuit stiffness for small values of NCR. Yet, for NCR near unity the stiffness modulus ratio exhibits an asymptotic behavior. Approaching the NCR value of 1/(1-k_{31}) from small values causes the stiffness to approach positive infinity. Similarly approaching from larger values causes the stiffness to reduce, become zero, and then approaches negative infinity. The stiffness modulus ratio is equal to zero when the NCR is exactly 1. The piezoelectric element can be approximated as a negative spring when the NCR is within the region between short circuit and open circuit capacitance. Similarly, the stiffness is greatly reduced for values slightly greater than NCR = 1.

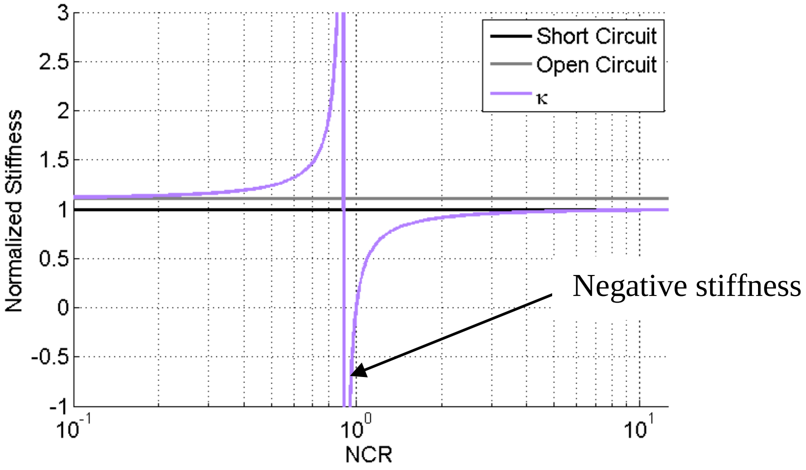

Figure 4.2 - Stiffness modulus ratio κ versus negative capacitance ratio (NCR)

To allow for introduction of significant loss factor, a resistor can be added to the negative capacitance. Two configurations are possible for the shunt configuration: parallel or series. The shunt impedance for a parallel circuit is

$$Z_S(\omega) = \frac{1}{\left[R_S\right]^{-1} - i\omega C_S} \tag{4.7}$$

and the series case is

$$Z_S(\omega) = R_S - \frac{1}{i\omega C_S}. \tag{4.8}$$

To achieve the largest loss modulus ratio, the capacitance of the patch should be equal to the shunt capacitance, or NCR = 1, which minimizes the denominator of Equation (4.3). The stiffness and loss modulus ratios for both the parallel and series shunt cases are shown in Figure 4.3. For a resistance of 5 kΩ, the parallel shunt shows decreasing loss modulus ratio for increasing frequency while the series shunt exhibits increasing loss modulus ratio. The stiffness modulus ratio has the opposite behavior of the loss modulus. Therefore if looking at the loss modulus ratio, the parallel shunt would have more control effect with increasing frequency and the series shunt would have more control at low frequency, with the loss modulus ratio modulus orders of magnitude greater than that attainable with a resistor alone.

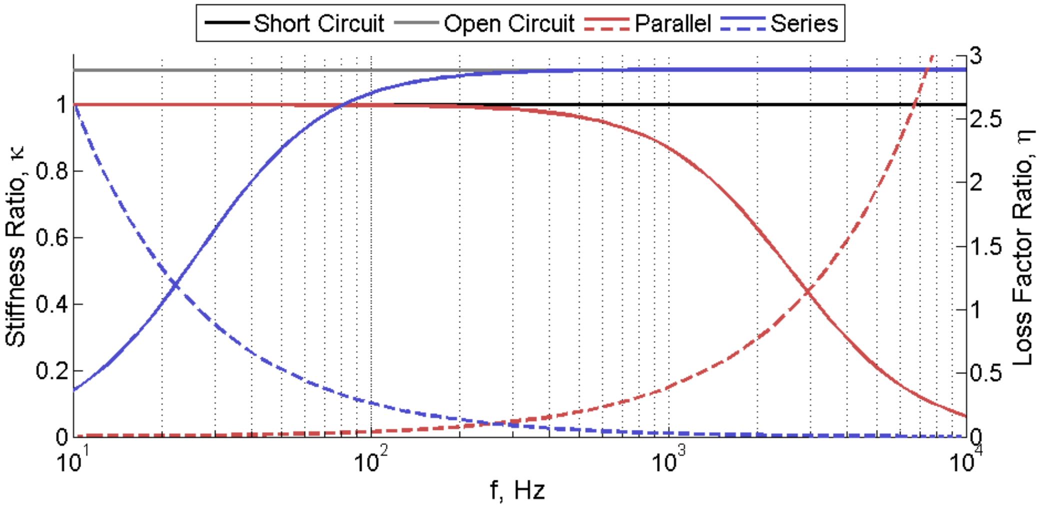

Figure 4.3 - Stiffness modulus ratio κ (solid line), and loss modulus ratio η (dashed line) versus frequency for parallel and series negative capacitance shunts, R_S = 5 kΩ, NCR = 1.00

The analysis above is in agreement with the results of Park and Park [65], but the ability to implement a negative capacitance shunt with a capacitance magnitude with the magnitude exactly equal to that of the patch capacitance for all frequencies is quite low due to the slight variability of patch capacitance versus frequency and exact experimental implementation and stability (which will be discussed in a later chapter). To explore this, Figure 4.4 and Figure 4.5 show the stiffness and loss modulus ratios for three values of shunt resistance when the magnitude of the negative capacitance is only 1% greater than the patch capacitance. For each of the resistors, the behavior of the stiffness modulus ratio is similar to that observed in Figure 4.3, the difference being the minimum value of stiffness modulus ratio obtainable is 0.1 instead of 0 when the NCR = 1. But, the trends of the loss modulus ratio for an NCR = 1.01 are completely different than observed trends when the NCR = 1. For three resistor values in series or parallel, the loss modulus frequency-dependent behavior mimics a resistor alone (see Figure 4.1). But, the magnitude of the peak value of the loss modulus for a shunt with a negative capacitance is 30 times that of a just a resistor. It should be noted it is also possible to obtain the same frequency behavior of the loss modulus using either the series or parallel configuration, only with significantly different resistor values, such as R_S = 50 Ω for the series configuration and R_S = 50 kΩ for the parallel configuration. Therefore, there may be no advantage of the parallel or series shunt configuration, assuming that the loss modulus is the dominant factor in control. But, if the stiffness modulus contribution is greater, then the frequency differences of the shunt configurations will be apparent.

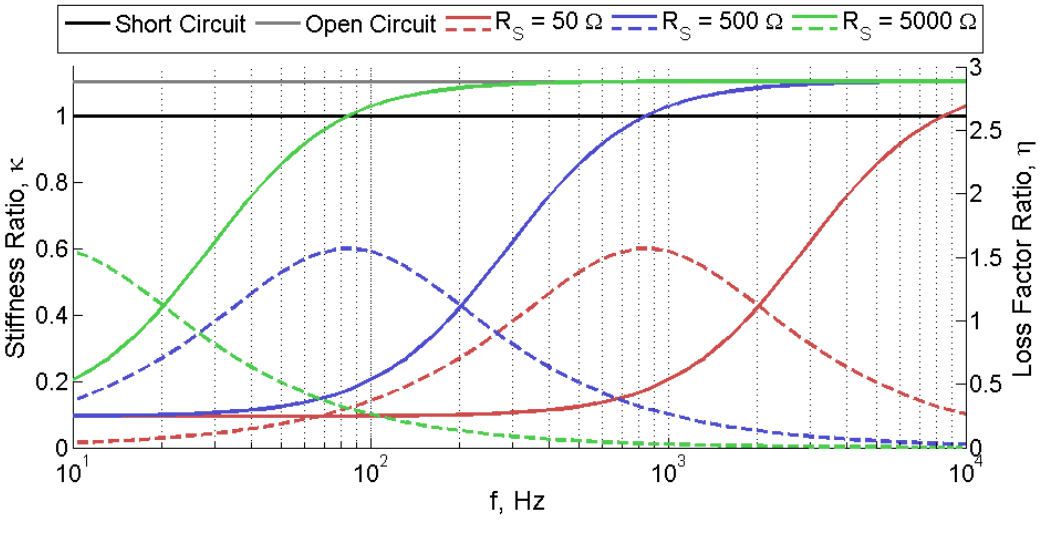

Figure 4.4 - Stiffness modulus ratio κ (solid line), and loss modulus ratio η (dashed line) versus frequency for a series negative capacitance shunt, NCR = 1.01

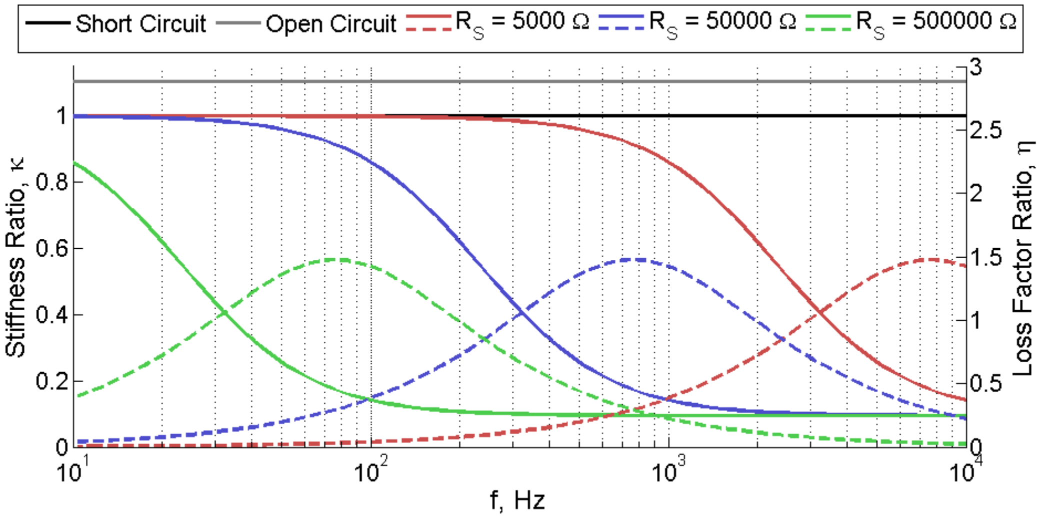

Figure 4.5 - Stiffness modulus ratio κ (solid line), and loss modulus ratio η (dashed line) versus frequency for a parallel negative capacitance shunt, NCR = 1.01

The effect of the negative capacitance ratio on the stiffness and loss modulus ratios for a given series shunt resistor is shown in Figure 4.6. For high frequencies, the stiffness for all negative capacitance ratios equals that of the open circuit stiffness. The differences are seen at frequencies lower than 1000 Hz. In light of Figure 4.2, the stiffness modulus ratio at low frequencies can be less than one, zero, negative, and greater than one depending on the NCR. These cases are shown for NCR = 1.03, 1, 0.97 and 0.87 respectively. The loss modulus associated with NCR of 1.03 and 0.87 are quite similar and exhibit the behavior as shown in the figures above. Because the shunted stiffness goes to zero at 0 Hz for NCR = 1, the loss modulus ratio approaches zero as the frequency decreases. Yet when the NCR = 0.97, the shunted stiffness transitions from negative values to positive, which causes the loss modulus ratio to go to infinity at the zero crossing frequency, 120 Hz. Therefore, it is possible to select a resistor/negative capacitance combination that will obtain infinite loss factor at any frequency. Also, the combination of resistor and negative capacitance for infinite loss factor modulus at a given frequency is non-unique which occurs due to the fact that there is an infinite set of impedances that will cause the stiffness modulus E_d to be zero at a given frequency.

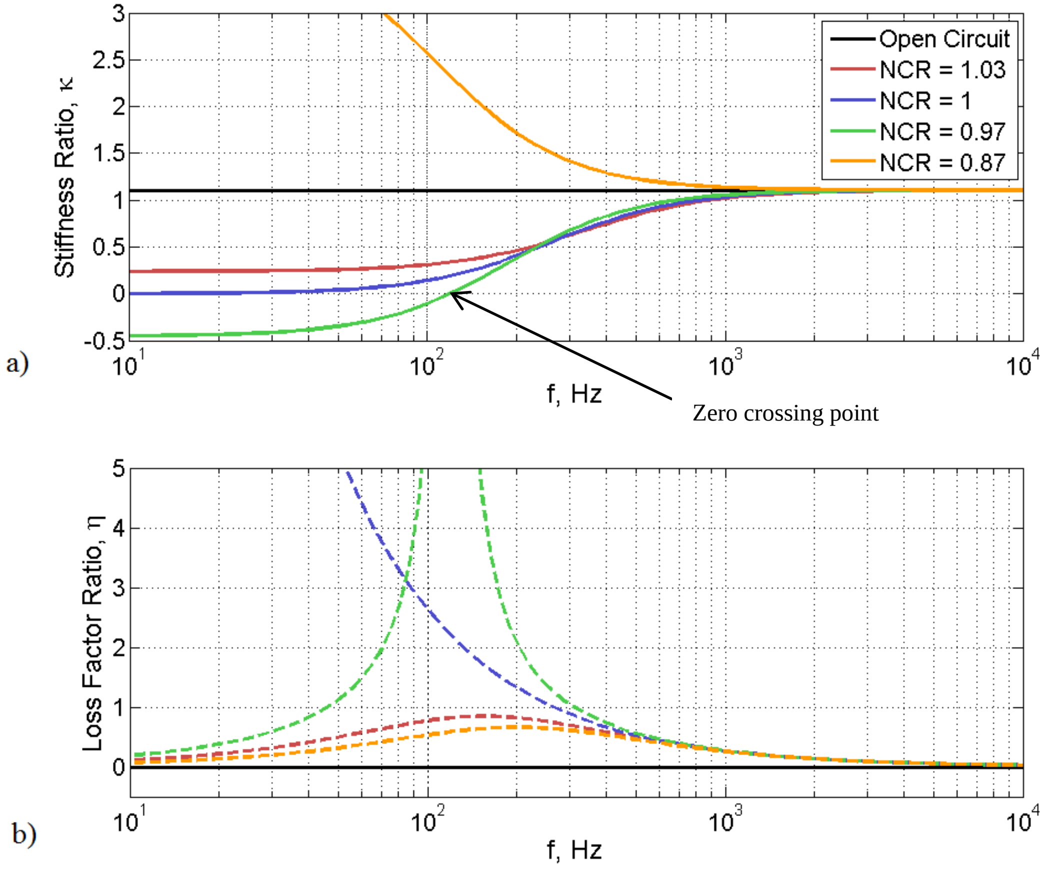

Zero crossing point

Figure 4.6 – a) Stiffness modulus ratio κ (solid line), and b) loss modulus ratio η (dashed line) versus frequency for parallel and series negative capacitance shunts, R_S = 500 Ω

The above analysis only investigates the changes of the piezoelectric material. The overall system stiffness and loss moduli will include the shunted piezoelectric material properties and the substrate properties. This combination of bending stiffness and loss moduli will dictate the amount of control possible when implementing a shunt. It should also be stressed that to implement a negative impedance, the circuit must be inherently active. The implementation of the negative capacitance is discussed in the next section.

4.3 Experimental Implementation of Negative Capacitance Circuits

Throughout literature the negative capacitance shunt includes an active negative capacitance element and a resistor [45, 58, 65, 67, 87, 88]. The placement of the resistor in either series or parallel affects the frequency behavior of the shunt, as discussed in the section above. Park discussed the frequency behavior in terms of the stiffness ratio and loss factor [87]. When a resistor is placed in parallel with the negative capacitor, Figure 4.7a, the stiffness ratio decreases with increasing frequency. Inversely, a resistor in series, Figure 4.7b, has a low stiffness modulus ratio for low frequencies and increases for higher frequencies.

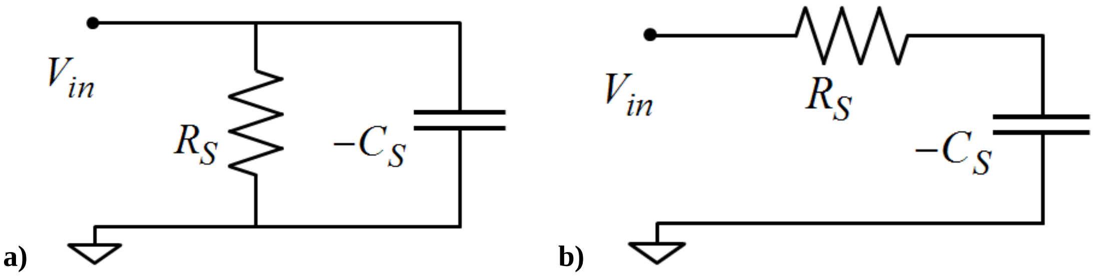

Figure 4.7 - Negative capacitance shunt schematic; a) Parallel b) Series

The implementation of the negative capacitance element is achieved by creating a negative impedance using a negative impedance circuit, Figure 4.8 [21]. The impedance of this circuit is

$$Z_{in} = -\frac{Z_3 Z_2}{Z_4}. \tag{4.9}$$

Since a negative capacitance is desired, Z_2 or Z_3 must contain a capacitor and the ratio of the other two impedances dictates the magnitude of negative impedance. Figure 4.9 shows a “Type 1” circuit where Z_2 is chosen to be the only capacitance element. Figure

4.10 shows a “Type 2” circuit where Z_3 is chosen as the capacitance element. Both instances have been shown to obtain desired negative capacitance magnitudes [47, 52, 59]. By applying the parallel and series configuration to both types of the negative capacitance circuit, four different negative capacitance shunt configurations are possible. All instances have been used in the literature. Park used the Type 1 circuit, Figure 4.9, with both series and parallel resistances [45, 87]. Behrens used the Type 2 circuit, Figure 4.10, with a series resistance [58]. Wu used a modified Type 2 circuit with a parallel resistance [89]. Thus either type of negative impedance circuit can be used successfully for control. The series implementation and the “Type 1” circuit will be the focus of this work.

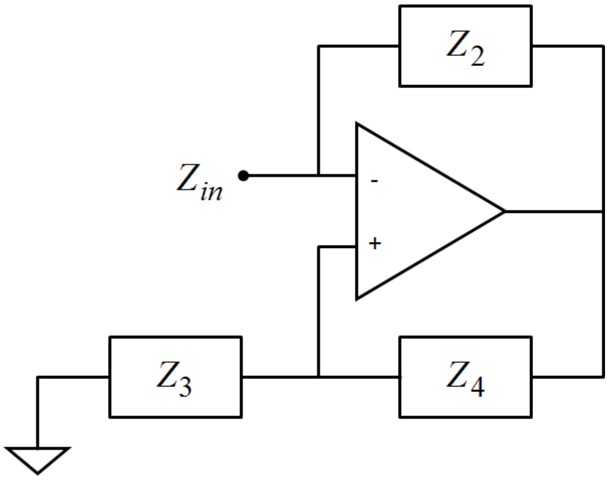

Figure 4.8 - Schematic of a negative impedance circuit

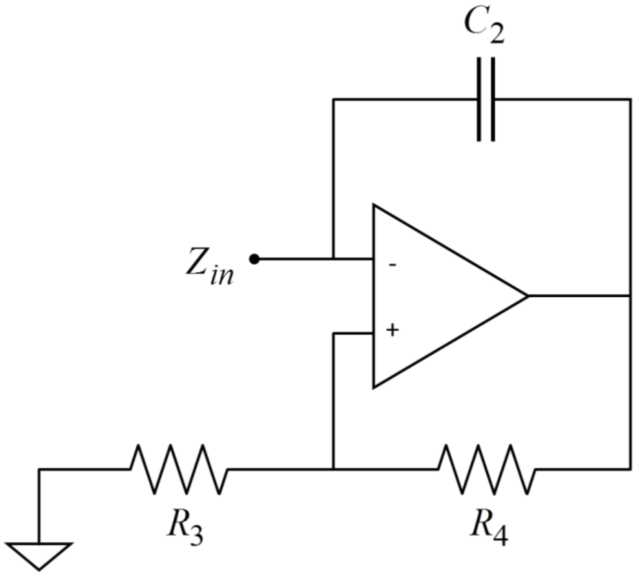

Figure 4.9 - Type 1 negative capacitance circuit

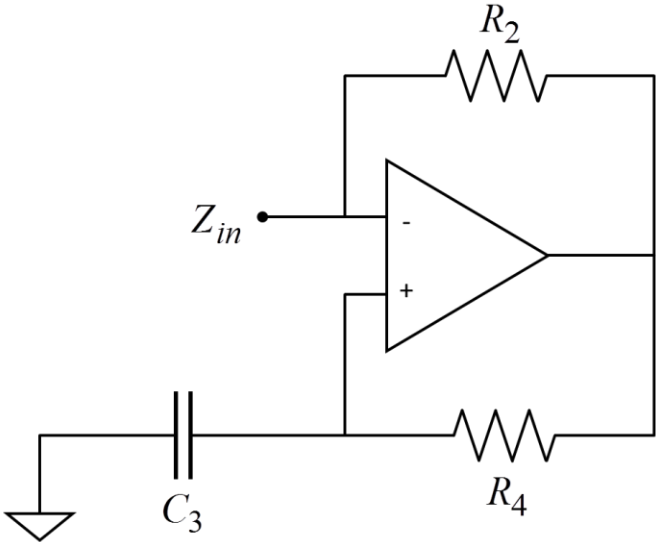

Figure 4.10 - Type 2 negative capacitance circuit

Necessary additions must be made to the final circuits for implementation to achieve the desired shunt impedance because of the dynamics of the op-amp. Both circuit types must contain a resistor in parallel with the reference capacitor to allow for feedback at DC. Without this resistor, the circuit would be unstable at low frequency. The parallel resistor for the “Type 2” circuit prevents the capacitor from acquiring a DC charge by allowing bias current from the op-amp to flow to ground [47]. The full shunt impedance may be explored by investigating the “Type 1” circuit, Figure 4.11. This circuit produces an input impedance of

$$Z_{in} = -\frac{\left[i\omega C_2 + \left(R_2\right)^{-1}\right]^{-1} R_3}{R_4}. \tag{4.10}$$

The resistor R_2, as stated, is necessary for op-amp stability at DC, but is sufficiently large to be considered negligible because for most patch and reference capacitances the real component of Z_{in} only appears below 10 Hz which is below the frequencies of interest for control. Therefore, Equation (4.10) can be simplified to express the impedance in terms of a negative capacitor

$$\frac{1}{i\omega C_{in}} = -\frac{1}{i\omega C_2}\frac{R_3}{R_4}. \tag{4.11}$$

Equation (4.11) can be rearranged to solve for the negative capacitance magnitude

$$C_{in} = -\frac{R_4}{R_3} C_2. \tag{4.12}$$

Also, the resistive element R_S of the shunt is placed in series between the patch and the negative capacitance creating the full shunt impedance

$$Z_S = R_S + \frac{1}{-i\omega C_{in}}. \tag{4.13}$$

A similar analysis can be performed for the Type 2 circuit, shown in Figure 4.12 which creates exactly the same impedance as the “Type 1” circuit.

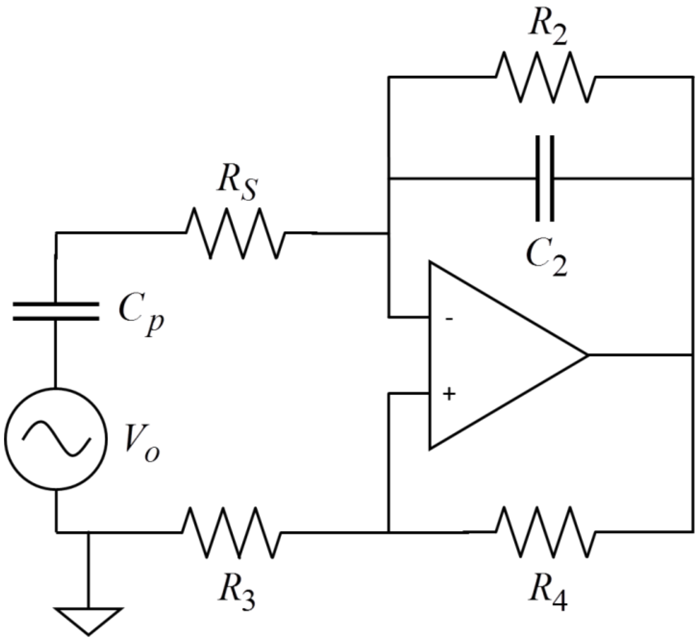

Figure 4.11 - Final Type 1 negative capacitance shunt

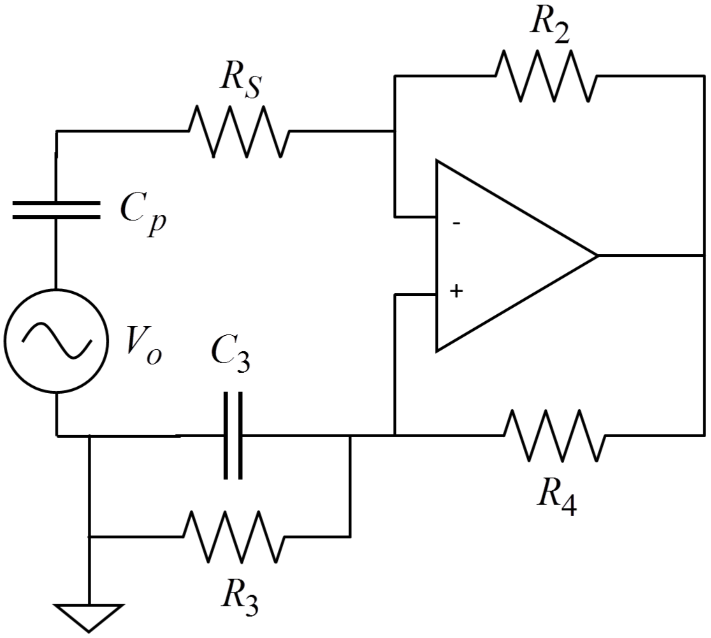

Figure 4.12 - Final Type 2 negative capacitance shunt

4.3.1 Physical Realization

For experimental testing the negative capacitance shunts were created using TI OPA445 operational amplifiers and basic circuit components. Preliminary and exploratory circuit tests were performed on a breadboard circuit. As the parameter space for the circuit was narrowed a prototype circuit was designed. A prototype schematic for a “Type 1” circuit is shown in Figure 4.13 and Figure 4.14 depicts the physically realized circuit on a milled copper circuit board. The circuits used for experimentation include the necessary components for op-amp protection including supply-side capacitors and diodes. The op-amp is powered by a custom built dual DC power supply up to +/- 40 volts. Potentiometers were used for most of the resistors in the shunt implementation to assist in tuning of both the negative capacitance and series resistance. Specifically, a potentiometer is used for the series resistor, R_S, to allow for straightforward selection of the real component of impedance when the target negative capacitance is obtained. Section 4.3.2 describes how the target magnitude for negative capacitance is reached. A potentiometer is used for the resistance divide in Equation (4.12). The use of a potentiometer simplifies Equation (4.12) which becomes a function of only one variable, α, and independent to the magnitude of the potentiometer

$$C_{in}(\alpha) = -\frac{(1-\alpha)}{\alpha} C_2 \tag{4.14}$$

where α is defined as R_3/R_{pot} and R_{pot} is the resistance of the potentiometer. To protect against infinite op-amp gain, which occurs when $\alpha = 1$, a small resistor is added in the R_4 branch in the prototype circuit. A simple terminal screw block is employed to allow for manageable altering of the magnitude of the reference capacitor. Similarly, the two patch leads are attached to the circuit through a terminal block where one must be grounded within the circuit. Test pins were added to facilitate probing of the circuit during operation.

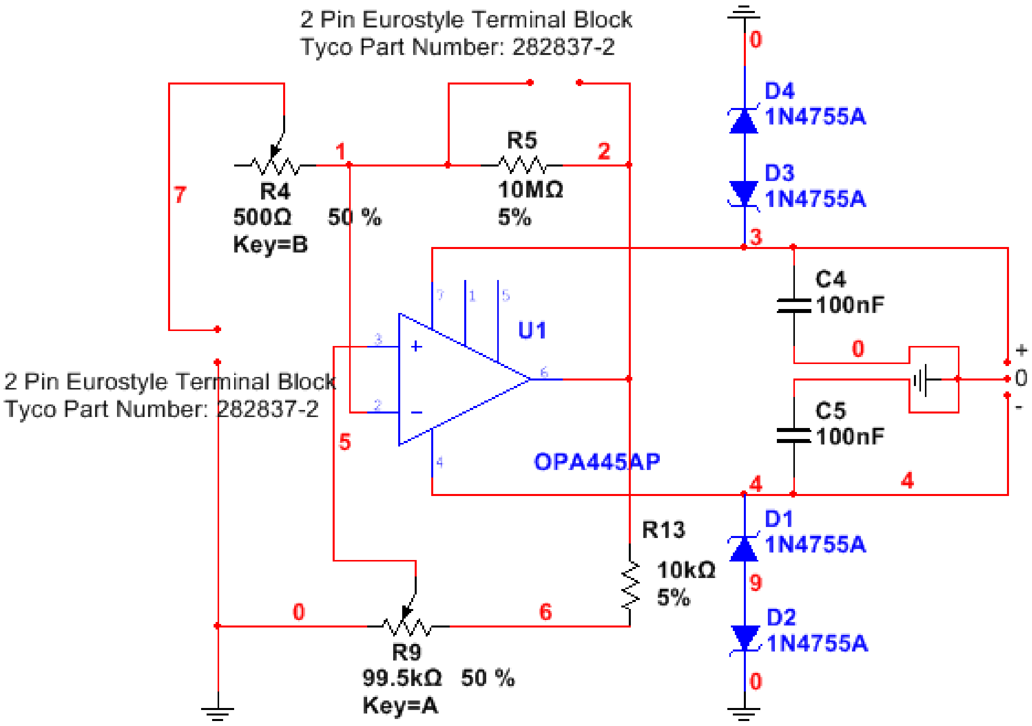

Figure 4.13 - Schematic of a negative capacitance prototype circuit

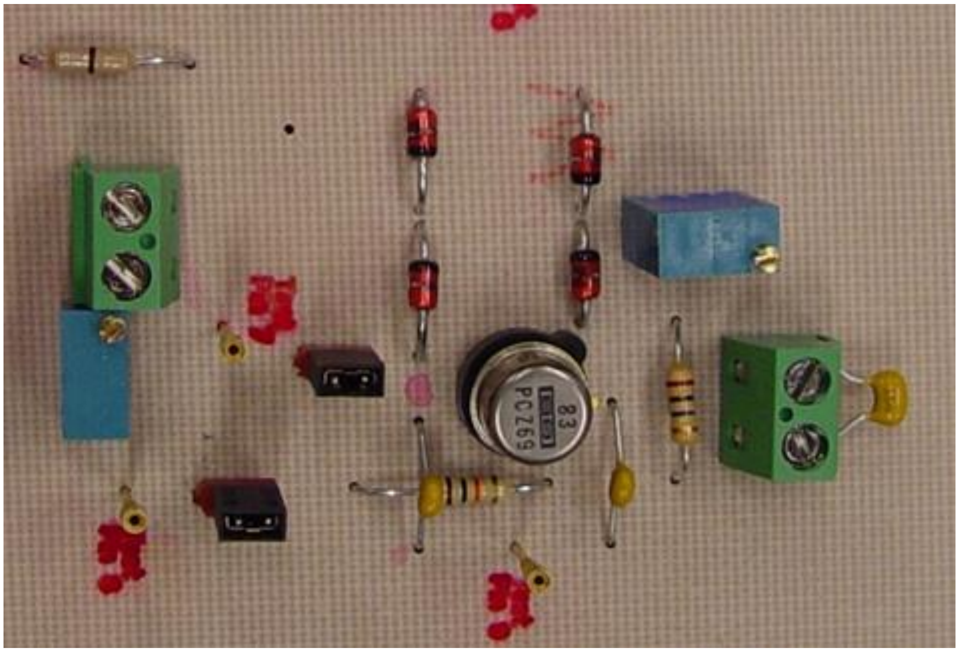

Figure 4.14 - Photograph of a prototype negative capacitance shunt

4.3.2 Experimental Procedure

Achieving a specific magnitude for the negative capacitance required a specific procedure. Due to the nature of the circuit, the negative capacitance circuit is stable for negative capacitance magnitudes larger than the patch capacitance. In practice, the control gain for the shunt is increased by decreasing the magnitude of the negative capacitance impedance from a value greater than the patch capacitance. Yet, as the magnitude approaches the patch capacitance the circuit will become unstable. The unstable response of the circuit is undesirable. Therefore, to achieve maximum control experimentally, the shunt is tuned to as close to the instability point as possible. The experimental tuning process begins by selecting a reference capacitor with a magnitude on the same order as the patch capacitance. By selecting this magnitude of reference capacitor, the tuning potentiometer has the greatest range of tuning possible and the least sensitivity to changes in α.

In practice, the forcing which drives the vibrating system of interest should be on to allow the shunt to create a voltage response for which to monitor the stability. The output voltage of the op-amp (pin 6 in Figure 4.13) is measured and monitored using a Tektronix P2220 voltage probe connected a Tektronix TPS2012B oscilloscope. Initially, the potentiometer should be set to large values of α before the op-amp is powered, corresponding to very large magnitude negative capacitance, or very small imaginary impedance. The circuit is then powered. The potentiometer is then turned to reduce α, which increases the voltage output being monitored. If the output of the op-amp jumps “rail-to-rail”, that is when the output of the op-amp jumps from positive voltage rail to negative voltage rail, then the circuit has gone unstable. The value of α at this condition marks the “instability point” of the circuit. The potentiometer is turned down past the instability point until the response returns to the linear range of the circuit. It should be noted that there may be a significant change to the potentiometer to return to the stable region. Therefore, the potentiometer can be turned again to decrease α to a point just above the instability point. Then, by recording the resistance values of R_3 and R_4 the impedance of the circuit can be computed.

4.4 Comparison of Tuning Methods

A numerical comparison between two of the shunt tuning theories presented in Section 2.4 is made below to both demonstrate the control ability of the negative capacitance shunt on a simple system and to describe the effects of altering the shunt parameters on the vibration response. Because the analysis presented in Sections 2.4.3 and 2.4.4 showed that the parameter solution to the wave tuning method and minimization of reactive input power should be the same, these two methods are compared for a simple cantilever beam. The numerical responses of the parameters chosen with these methods are compared to the shunt parameters that can be obtained experimentally. Similarly, the global effects of the shunt will be presented.

4.4.1 Experimental Setup

To verify the results of the wave tuning and minimization of reactive input power tuning theories, a setup consisting of a cantilever beam, a driving mechanism, a tunable electrical shunt, and a data collecting system is used. For ease of comparison with the Park and Palumbo study, an identical cantilever beam was analyzed, which is based on the beam used by Hagood and von Flotow, and used by Cunefare [10, 11, 67, 90]. Figure 4.15 depicts the beam with two pairs of attached piezoelectric patches. The physical properties of beam and patches are shown in Table 4.2. The patches are bonded to the aluminum beam and cover the full width of the beam, 2.55 cm. The location of the driving pair is *L*/3 along the length of the beam.

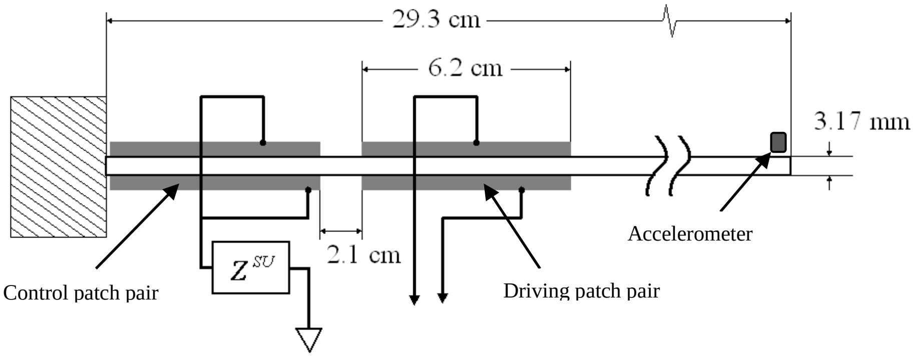

Figure 4.15 - Cantilever beam with shunted patch pair and driving patch pair

Table 4.2 - Cantilever beam and patch physical properties

Beam	Young's modulus	E_b = 73 Gpa
	Density	ρ_b = 2700 kg/m^3
	Width	w = 2.55 cm
Piezoelectric	Young's modulus, shorted	E_p = 63 Gpa
	Density	ρ_p = 7800 kg/m3
	Coupling coefficient	k_{31}= 0.35
	Thickness	t = 0.25 mm
	Capacitance, total	C_p = 116 nF

Two methods of driving the cantilever beam are used. The first involves a mechanical shaker that driven by a swept sine over the frequency range of interest. The point force location of the mechanical shaker is 14.8 cm from the base of the beam. A swept sine voltage applied across the driving patches is the second driving mechanism. The data acquisition system recorded tip vibration, average spatial vibration, electrical power input, as well as mechanical impedance. Tip vibration was acquired using an accelerometer placed at the end of the beam. A Laser Doppler Vibrometer (LDV) was used to obtain spatial average vibration measurements. The piezoelectric disturbance voltage was obtained by placing a voltage probe across the driving patch terminals, to study the phase between the tip response and driving voltage. The driving impedance from the shaker was measured using an impedance head and analyzed through post processing.

4.4.2 Results and Analysis

The wave-tuning and minimum reactive power input methods for shunt selection are compared by analyzing the vibration response of the beam and the input power to the system. Both the tip vibration velocity as well as the spatial average velocity response are compared for the open circuit case, which is considered uncontrolled, to the optimal value for shunting parameters. The input power of the system is analyzed by consideration of the phase response of the voltage driving the driving patches on the beam and the reactive input power from the shaker. The theoretical shunt tuning values obtained by the modeling approach given in Section 3.2 are compared to the experimentally optimized values.

The shunt parameter values found through optimization exhibit a dependence on frequency. Figure 4.16a and Figure 4.16b show the optimal theoretical resistor and negative capacitance values for both tuning theories. In general as the driving frequency increases, the optimal resistor value decreases and then levels off at a value close to zero. Similarly, the magnitude of the optimal negative capacitance value decrease as the frequency increases slightly. There are some deviations between the two theories. These inconsistencies are present at frequency ranges that are not at controllable modes, and occur because of optimization function instabilities and the non-unique nature of the solution. Specifically, Table 4.3 compares the optimal shunt values at the first 5 modes.

These values are all similar to each other, except for the capacitance value at the 4th mode.

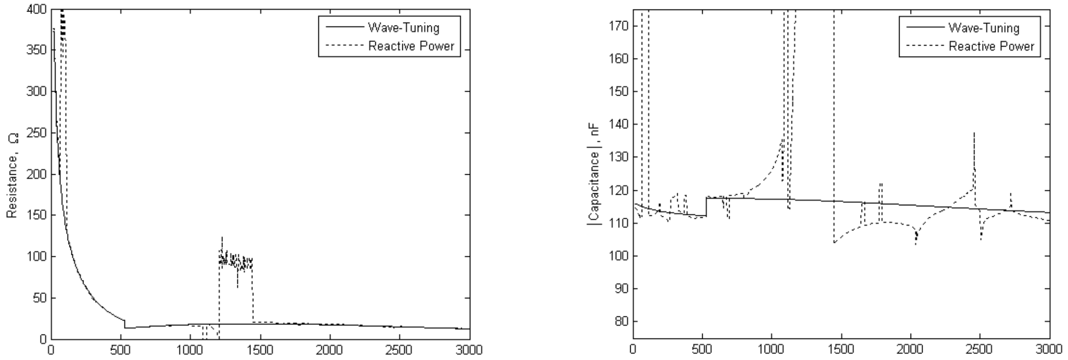

a) b)

Figure 4.16 - Optimal shunt values a) Resistance value b) Capacitance value

Table 4.3 - Comparison of shunt parameters, Theoretical

		Mode Number				
		1	2	3	4	5
	Frequency (Hz)	34.7	222.8	610.3	1177	1941
Wave Tuning	Capcitance (nF)	-115.5	-113.5	-118	-117.1	-115.6
	Resistance (Ω)	405	99	19.6	25.5	24.4
Reactive Power	Capcitance (nF)	-113.4	-111.9	-117.4	-196	-109.8
	Resistance (Ω)	413	100.6	19.5	15.3	25.7

The optimal shunt values determined experimentally were limited by the stability of the shunt circuit. The negative capacitance can only reach a certain level before a circuit instability point is reached, which was determined to be -119.6 nF for this system. Therefore, the negative capacitance values solved for by the shunt selection theories were unattainable. Yet, significant performance was achieved through the use of the NIC circuit. Figure 4.17 shows the tip vibration velocity response of the beam with the shunt shorted and the response when the shunt is tuned to the first mode. The first resonance of the beam has been reduced by 30 dB for the wave tuning method and 20 dB for the minimum reactive input power method. The optimal experimental values for the shunt are shown in Table 4.4. These shunt values show similar trends as the theoretical values.

The resistance value decreases with increasing frequency, with the negative capacitance held at the maximum, as stated earlier.

Table 4.4 - Optimal shunt parameters, Experimental

		Mode Number				
		1	2	3	4	5
	Frequency (Hz)	34.4	197.3	556	1027	1754
Experimental	Capcitance (nF)	-119.6	-119.6	-121.4	-120.1	-119.6
	Resistance (Ω)	787	314	155	113	6

The theoretical responses of the beam for the wave tuning and minimum reactive power input theories are compared to verify the correlation between the two. The tip velocity response is compared in Figure 4.17, tuned to the first mode. Even with the tuning focused on one mode, there is still broadband attenuation at the other modes. The experimental tip velocity, Figure 4.18, achieves similar suppression as the theoretical implementation, but could not achieve as great a control because of the shunt limitations. The first mode is reduced by 22 dB.

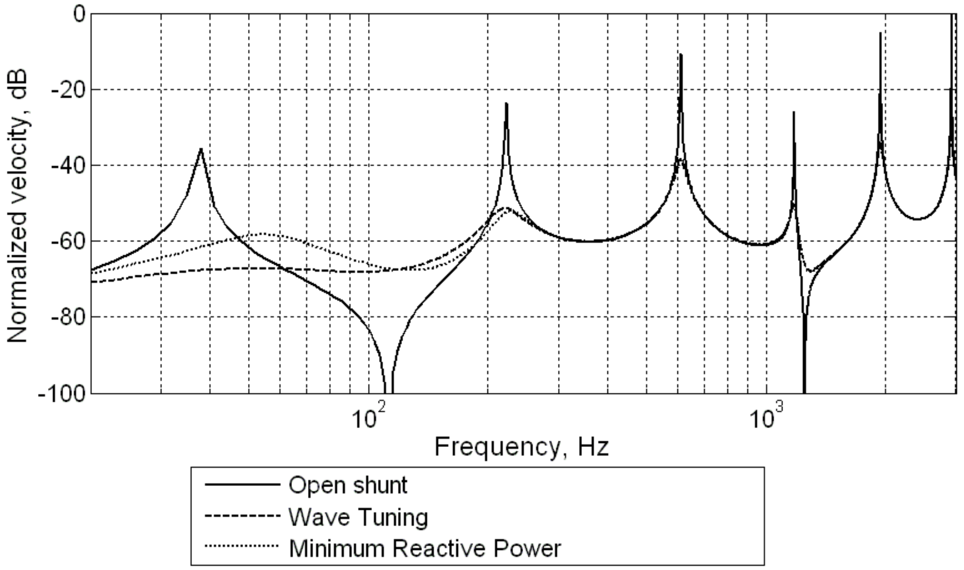

Figure 4.17 - Theoretical tip velocity response, shunt tuned to the first mode

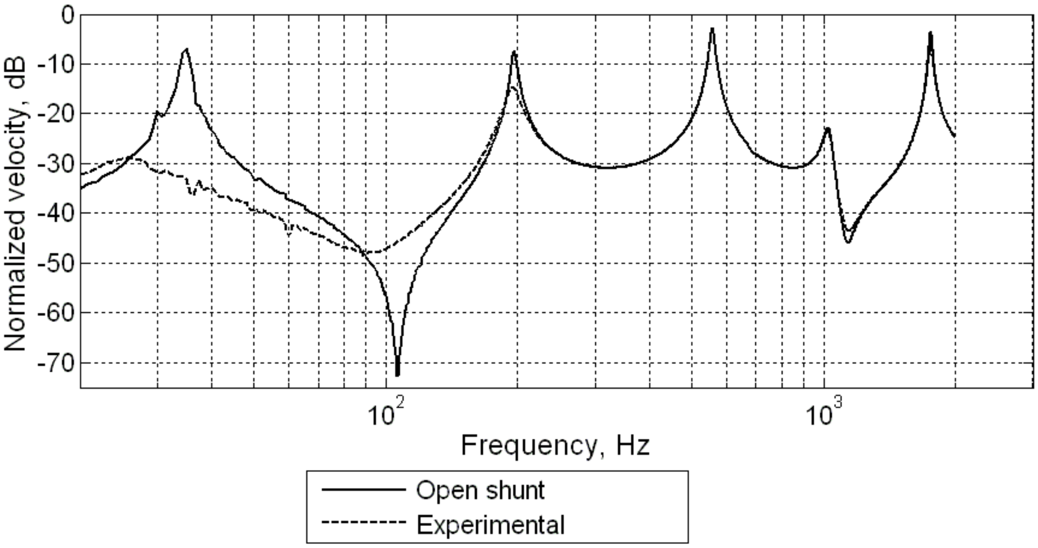

Figure 4.18 - Experimental tip velocity response, shunt tuned to the first mode

The spatial average response of the beam is also of interest as this relates to the global suppression of vibration. Theoretically, both tuning methods achieve overall vibration suppression by reducing the standing wave, when tuned to the second mode, across the whole of the beam, which is shown in Figure 4.19. There are some increased levels of vibration at the frequencies with minimum vibration, which occurs because the beam begins to act as if it is infinite, due to the suppression of the reflected wave. This decreases the destructive interference of the incident and reflected wave, which inherently increases the vibration response. The spatial average response experimental results, Figure 4.20, confirm the reduction of vibration on the beam with the most reduction at the first mode. This response coincides with the results of the response of the tip, which will allow the tip response to be an adequate measure of the global reduction for a cantilever beam.

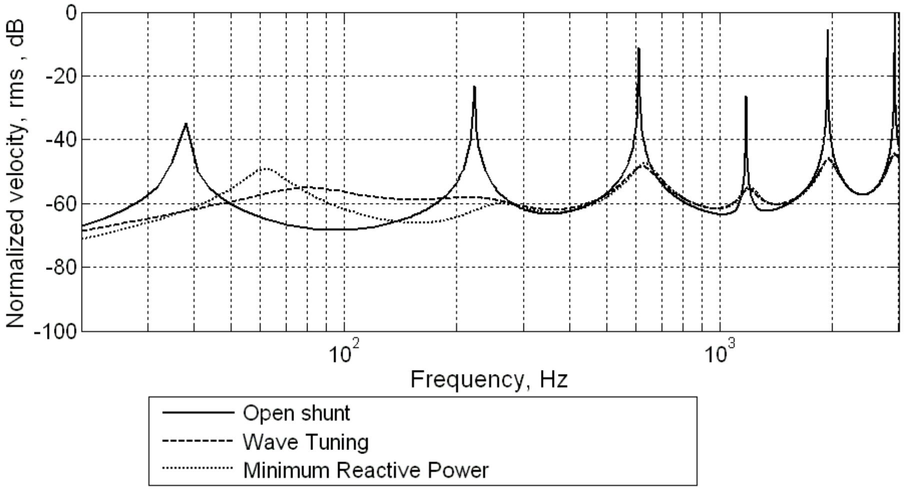

Figure 4.19 - Theoretical spatial average velocity, shunt tuned to the second mode

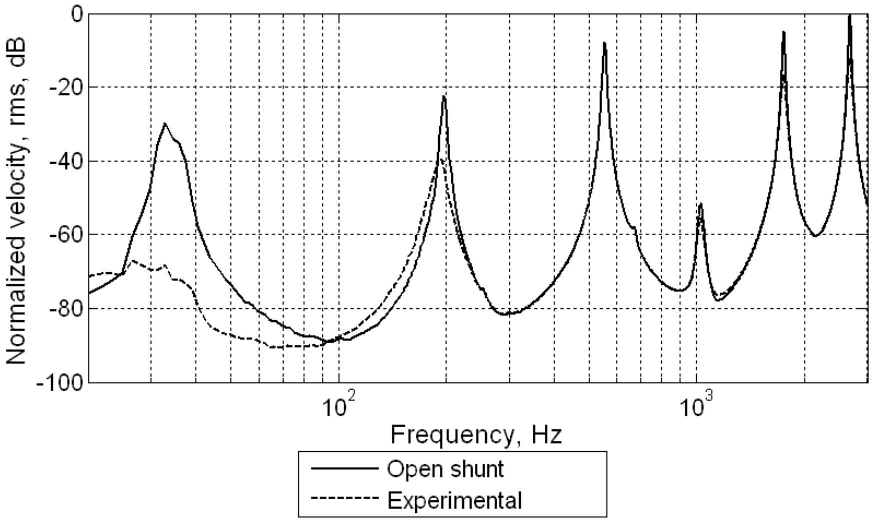

Figure 4.20 - Experimental spatial average velocity, shunt tuned to the second mode

A reduction of reactive input power at the point of the shaker input force is observed as the shunt is tuned to each mode. This is best illustrated by inspecting the sixth mode of the beam because the small amount of system damping present before the introduction of the shunt when driven by the shaker. Figure 4.21 illustrates how the reactive power input to the beam is reduced as the tuning approaches optimal for the specific resonance.

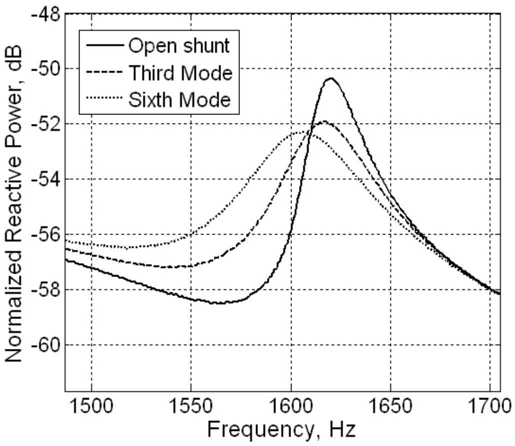

Figure 4.21 - Reactive power of the sixth mode for the tunings associated with the Third and Sixth mode

The phase difference between the tip response and the voltage supplied to the driving patch are investigated to attain another picture of reactive power input the system. The power can be defined as

$$P = |F||v|(\cos\theta + i\sin\theta) \tag{4.15}$$

where the phase angle between the force and velocity is θ. If the beam is assumed to be lightly damped, the phase difference between the force and velocity at any point on the beam will be the same. Therefore, a decrease in the reactive power correlates to a decrease in the phase difference. Figure 4.22 and Figure 4.23 show a reduction in phase differenced when tuned to the first mode. Therefore, as the phase difference approaches zero, the input power becomes less reactive, which confirms the minimization reactive power tuning theory. This reduction in reactive power decreases the standing wave, in turn decreasing the vibration magnitude across the whole beam.

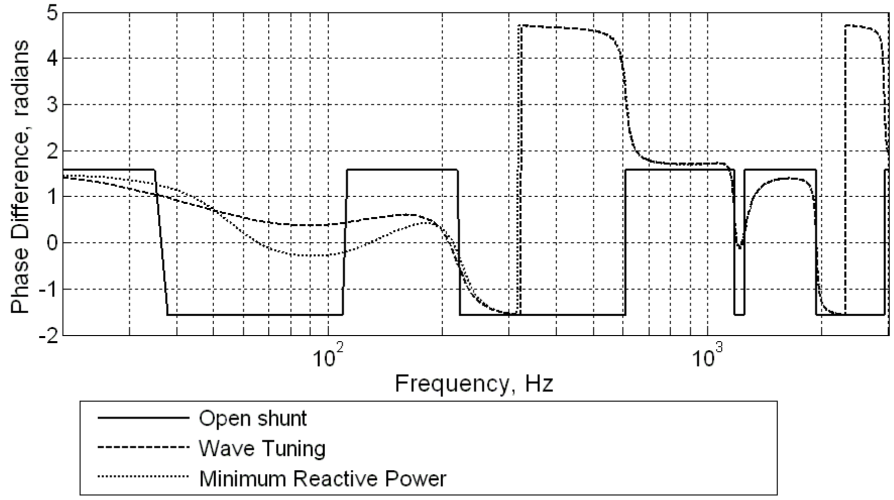

Figure 4.22 - Theoretical phase difference between tip response and voltage

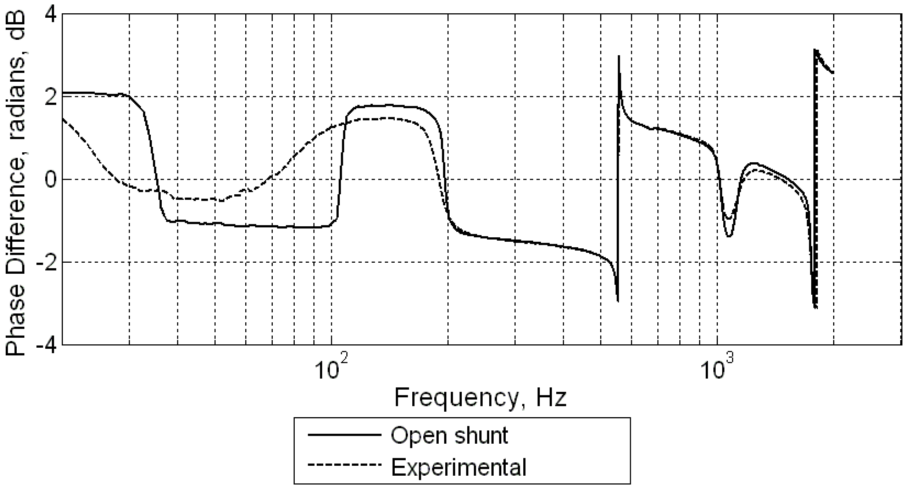

Figure 4.23 - Experimental phase difference between tip response and voltage

4.5 Summary

This chapter has presented a basic overview of the behavior of a negative capacitance shunt. The negative capacitance shunt is an active, broadband shunt but is simple enough for analysis to be performed similar to a passive shunt. When combined with a resistor, the negative capacitance shunt allows for large changes in both the stiffness and loss modulus ratios versus frequency. Using its frequency dependent characteristics, the shunt can be designed to achieve certain control frequency profiles.

The physical implementation of a negative capacitance circuit was presented. This presentation included a prototype circuit and the method for implementation.

The wave tuning theory developed by Park and Palumbo [11] has been shown to be experimentally and theoretically equivalent to the minimum reactive input power theory of Cunefare [67]. The wave tuning theory minimizes the reflected wave which has been shown to be equivalent to the minimization of reactive input power. The control shunt yields a decrease in tip vibration, spatial average vibration amplitude (a measure of global reduction), and minimization of reactive input power. The negative capacitance shunt shows broadband control of vibration centered on the tuning frequency.

CHAPTER 5

ELECTRO-MECHANICAL EFFECTS

5.1 Introduction

The electro-mechanical effects of a shunt control system are analyzed to understand and quantify the link between the electrical domain of the shunt and its effect on vibration suppression. First, the power output of a negative capacitance shunt circuit is measured to analyze the correlation between vibration suppression and control effect, which will be considered the suppression in the velocity reduction of a vibration structure, with an interest in increasing the efficiency of the negative capacitance shunt. Next, a circuit analysis formulation for an adaptive tuning method is presented. An investigation of the circuit limitations and stability is performed. Finally, a summary of the electro-mechanical domain results is given.

5.2 Power Output and Efficiency

For the negative capacitance circuit to be considered a feasible control mechanism, the op-amp power versus some measure of control effort is required so that the requirements for the circuit can be designed. Apart from a measurement of circuit power, the goal of this section is to describe increases to the efficiency of the shunt, which will be defined as the power output of the op-amp with respect to the impedance of the shunt. The electrical limitations of the shunt will also be quantified.

An efficiency discussion of a negative capacitance shunt was made by Václavík and Mokrý for a piezoelectric stack actuator to decrease the force transmitted by a single degree of freedom piezoelectric oscillator at a single resonance [64]. Yet, they did not investigate how the power flow of the system was altered by changing the shunt parameters. This work will discuss the change in efficiency over a large frequency range when utilizing the negative capacitance shunt for flexural control. The efficiency of the shunt will be defined as the power output of the shunt divided by the power supplied by the op-amp,

$$\eta = \frac{S_{shunt}}{S_{op-amp}} . \tag{5.1}$$

To aid in this task, a piezoelectric patch connected to a negative capacitance shunt is electrically modeled using National Instruments Multisim circuit simulation software. The results of the numerical model will be compared to experimental measurements. Circuit modeling is presented first, followed by the method used to obtain experimental data and finally the results and analysis.

5.2.1 Circuit Modeling

National Instruments Multisim software was utilized to create a numerical model of a piezoelectric patch connected to a negative capacitance shunt, shown in Figure 5.1. With respect to the elements labeled in Figure 5.1, the Multisim model includes the electrical equivalent model of a piezoelectric patch which consists of a strain-induced voltage *V1* and a capacitor *Cp*. The model of the negative capacitance shunt includes all necessary components for experimental implementation, as outlined in Section 4.3.1. Multisim includes a manufacturer-provided electrical model of the op-amp. In addition to the shunt and patch, the impedances of two voltage sensors are included, which are necessary to experimentally measure the circuit response. A current probe is implemented by means of a voltage probe measuring the voltage across a small resistor R_I to determine the current flowing through the output terminal of the op-amp. The voltage probe is a 10x voltage attenuation probe used to measure the op-amp voltage, which is the same as used in experiments. A virtual oscilloscope is included in the model to measure the temporal response of the model. The software also performs AC circuit analyses to obtain frequency responses.

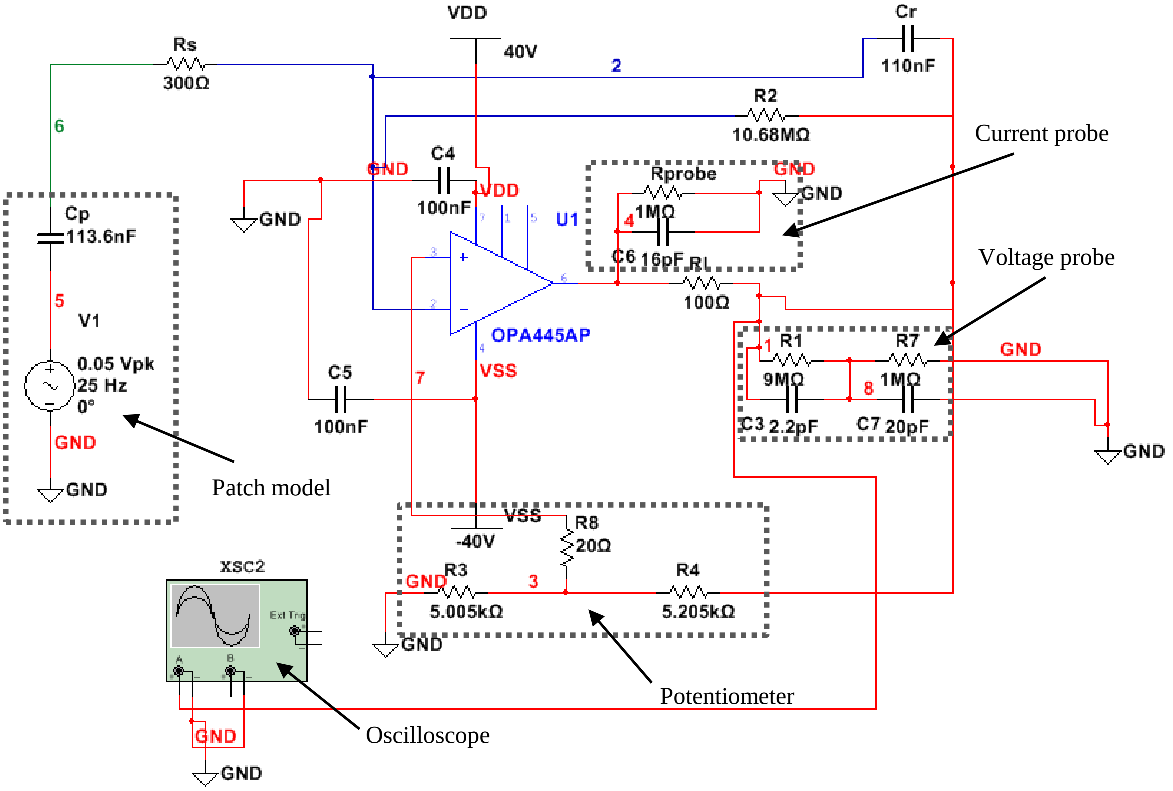

Figure 5.1 - Multisim shunt and patch model

The impedance of the shunt Z_s can be characterized by

$$Z_S = R_S + \frac{1}{-i\omega C_{in}} \tag{5.2}$$

where R_s is the series resistance and C_{in} is the magnitude of negative capacitance. Generally, the imaginary component of impedance of the shunt is described as a single capacitance value for all frequencies. The value of negative capacitance can be found by

$$C_{ratio} = -\frac{R_4}{R_3} C_r \tag{5.3}$$

where C_r is the reference capacitor in the inverting branch of the op-amp and C_{ratio} is considered the ratio approximation of negative capacitance. To verify that the negative impedance converter within the shunt creates a purely negative impedance and constant versus frequency to be characterized by a single value, the impedance of the Multisim model can be found by dividing the voltage of "node 2" V_2 by the current through the series resistor R_s,

$$Z_{sim} = \frac{V_2}{I_{R_s}}, \tag{5.4}$$

where Z_{sim} is the simulated impedance. The effective capacitance of the negative capacitance model can be calculated by

$$C_{sim} = \frac{\mathrm{Im}\left[Z_{sim}^{-1} \right]}{\omega} \tag{5.5}$$

where ω is the angular frequency. Figure 5.2 shows three frequency response plots of C_{sim} and the value of capacitance using the ratio representation C_{ratio}. The simulated response of the circuit closely matches the ratio representation of the negative capacitance shunt for all frequencies. The maximum error in capacitance between the two is 0.25%, therefore for frequencies from 10 to 5000 Hz the shunt can be accurately characterized by a single value of negative capacitance.

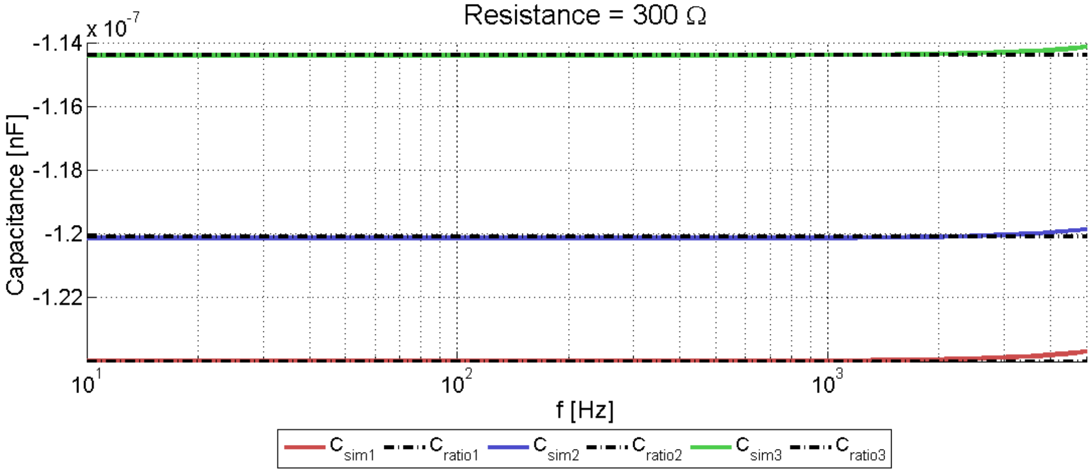

Figure 5.2 - Negative capacitance versus frequency for model and ratio representation

5.2.2 Experimental Setup and Procedure

This section presents the method used to measure the electrical behavior of the shunt circuit during control of a cantilever beam. The key electrical measure of interest is the power output of the operational amplifier. Figure 5.3 shows a schematic of the experimental circuit. To find the output of the op-amp, the voltage at the output, V_2, is measured using a 10x attenuating voltage probe, and the current is measured by determining the voltage drop over a small resistor R_I placed at the output pin of the op-amp, shown in Figure 5.3. The complex power output of the op-amp is computed by

$$S = \left[\bar{V}_2 I\right] \tag{5.6}$$

where the current is

$$I = \frac{V_I}{R_I} \tag{5.7}$$

and V_I is the voltage drop across resistor R_I

$$V_I = V_1 - V_2 \,. \tag{5.8}$$

The complex power can be expressed in terms of its real and imaginary components,

$$S = P + iQ \tag{5.9}$$

where P is the real power and Q is the reactive power. The apparent power is magnitude of the complex power, $|S|$.

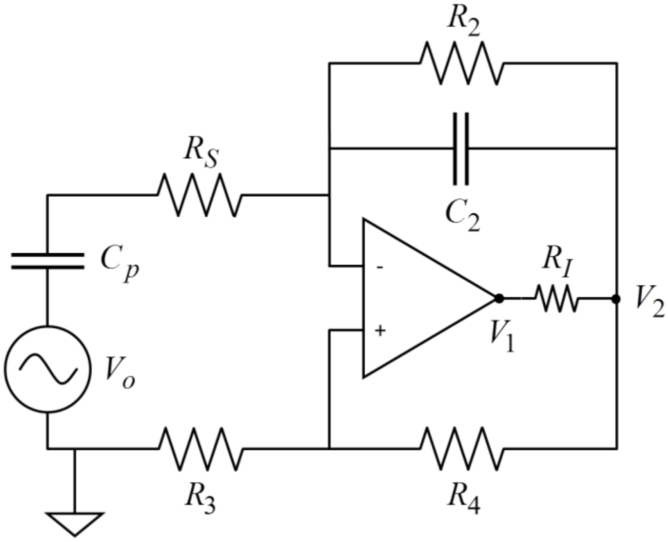

Figure 5.3 - Full shunt circuit schematic with experimental measurement probe locations V_1 and V_2

The experiments were performed on the same cantilever beam used in section 4.4.1, Figure 4.15, with two pairs of piezoelectric patches bonded to the surface. One pair of patches is used to drive the beam with a 5-5000 Hz band-limited random signal. The pair of patches bonded near the root of the beam is used as the control pair. It was previously shown in Section 4.4.2 that a negative capacitance shunt allows for global reduction of vibration, therefore, for simplicity, a single accelerometer placed at the tip is used to measure the response of the beam for various shunt conditions.

5.2.3 Results and Analysis

The results and analysis are presented in three sections. First, the circuit model is verified with experimentally obtained measurements of a negative capacitance shunt.

Second, the efficiency of the shunt is explored. Finally, an investigation of the limitations of the op-amp utilized for the negative capacitance is presented.

5.2.3.1 Model Verification

To verify the Multisim model, the power output of the op-amp was numerically simulated for four values of series resistance, R_s in Figure 5.3, and three values of negative capacitance, and compared to the measured power output. The circuit parameters used for verification in the Multisim model and for the experiments are shown in Table 5.1. The simulated power output for four values of series resistance is shown in Figure 5.4. The negative capacitance value of the shunt for all four resistors is -114.4 nF. At low frequencies, the power for all four cases is similar. But, the power output increases significantly for higher frequencies as the series resistance is reduced. An interesting result is that the phase of the power does not change for different resistance values, which indicates the series resistor only affects the gain of the circuit but not the impedance. Before comparing the experimental power to the model results, the tip response of the beam is presented first in Figure 5.5. The tip response for the four resistance values of the negative capacitance shunt are shown along with the uncontrolled response. The series resistor alters how much suppression occurs at the resonances of the beam. At low frequency, about 30 Hz, the 1200 Ω resistor results in more suppression, while small resistors improve the suppression at high frequency resonances.

Due to the resonances of the cantilever beam and the fact that the response of the beam is reduced at different frequencies for the four series resistors, the magnitude of the power output for the experimental system, as shown in Figure 5.6, does not match the simulated power output (the simulation does not include beam resonance behavior). The phase of the power matches the numerical output exactly, and does not vary with change in resistor. Yet the model can be verified by normalizing the square of the strain-induced voltage which dictates the response of the circuit, shown in Figure 5.7. The power output computed by the model, shown in Figure 5.4, exactly matches the experimental normalized power output. Yet for the non-normalized measured power output, it should be noted that a certain level of power output does not correspond to the same level of reduction in tip response. The power output at 32 Hz is the exact same for all resistance values, but the response of the beam is drastically different. The total apparent power output of the op-amp for all frequencies is shown in Table 5.2. Changing the resistor from 4800 Ω to 75 Ω increases the total power by two orders of magnitude. But, due to the power increase the response of the beam for the 75 Ω resistor is greatly reduced compared to the 4800 Ω resistor.

Table 5.1 - Verification circuit parameters

V_o	0.04 V
C_p	113.6 nF
C_2	110 nF
R_2	10.68 MΩ
$R_3 + R_4$	10.21 kΩ

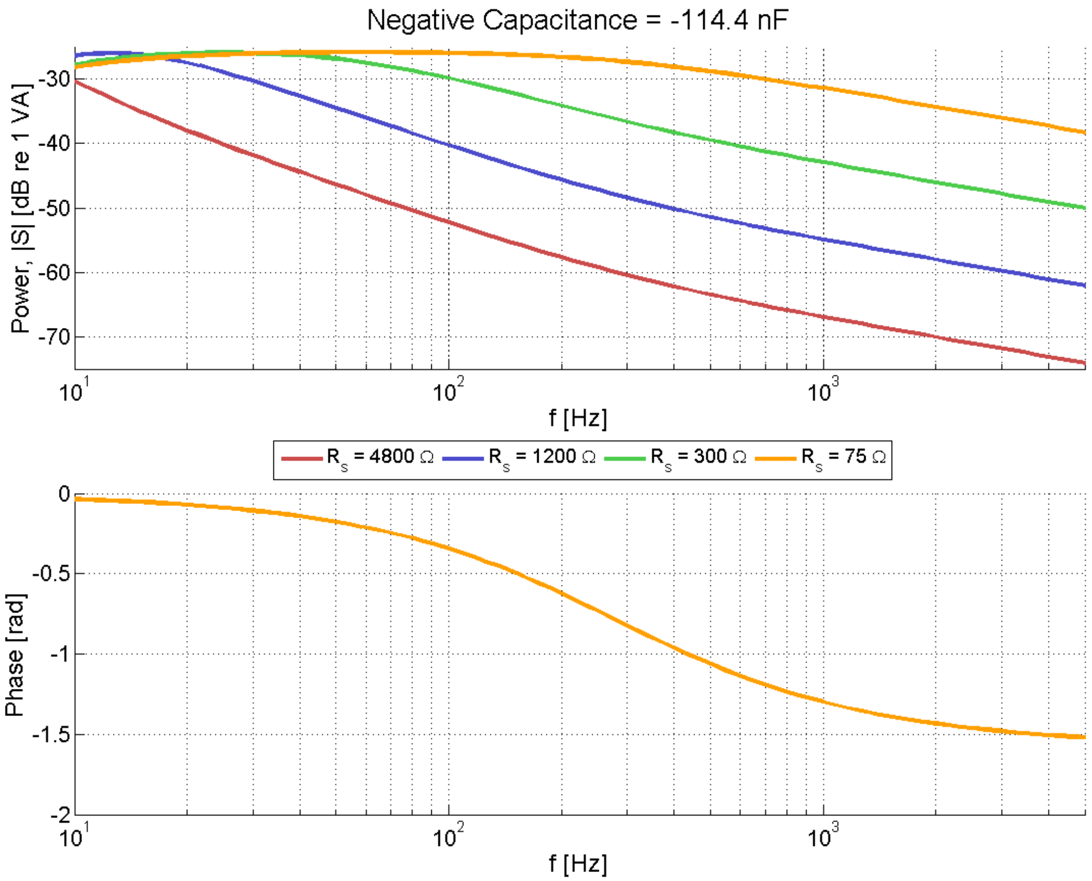

Figure 5.4 - Simulated power output of the op-amp, amplitude and phase, for four values of series resistance

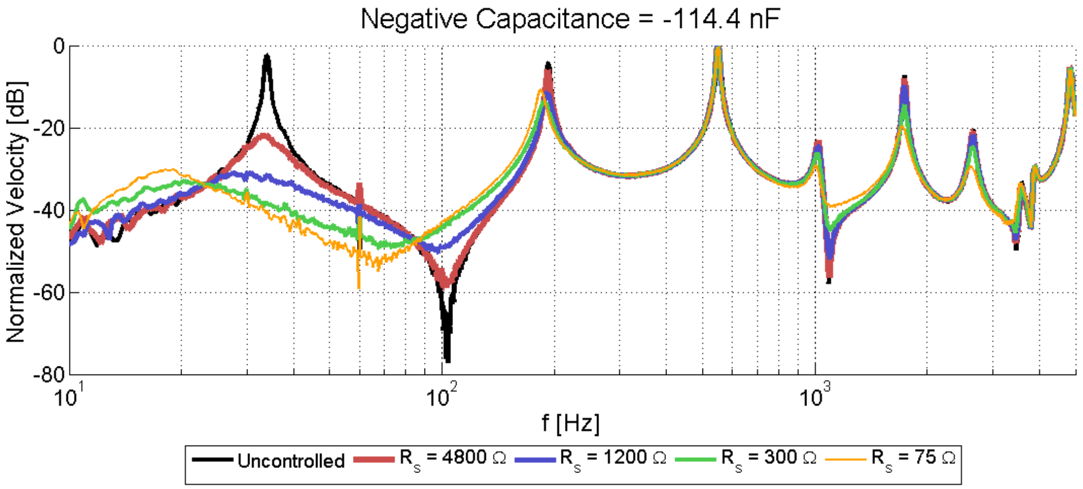

Figure 5.5 - Tip response of the beam for four values of series resistance

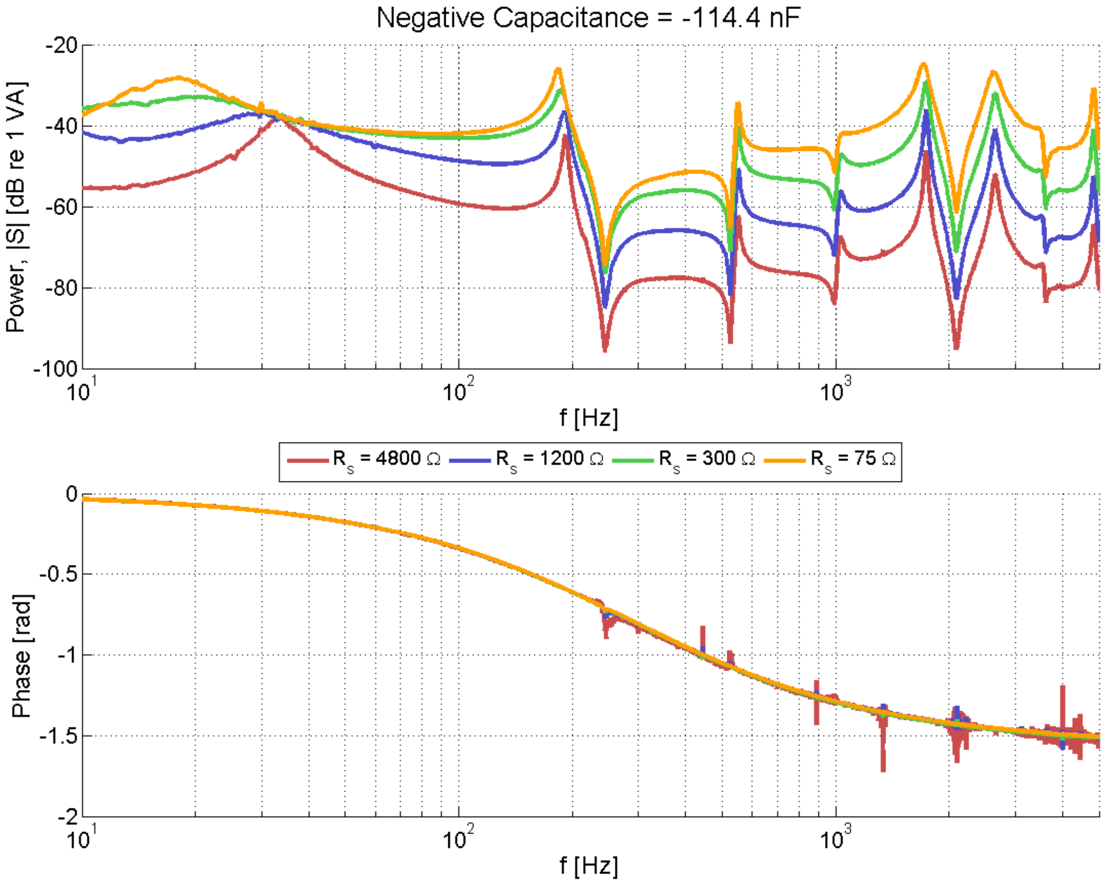

Figure 5.6 - Experimental power output of the op-amp, amplitude and phase, for four values of series resistance

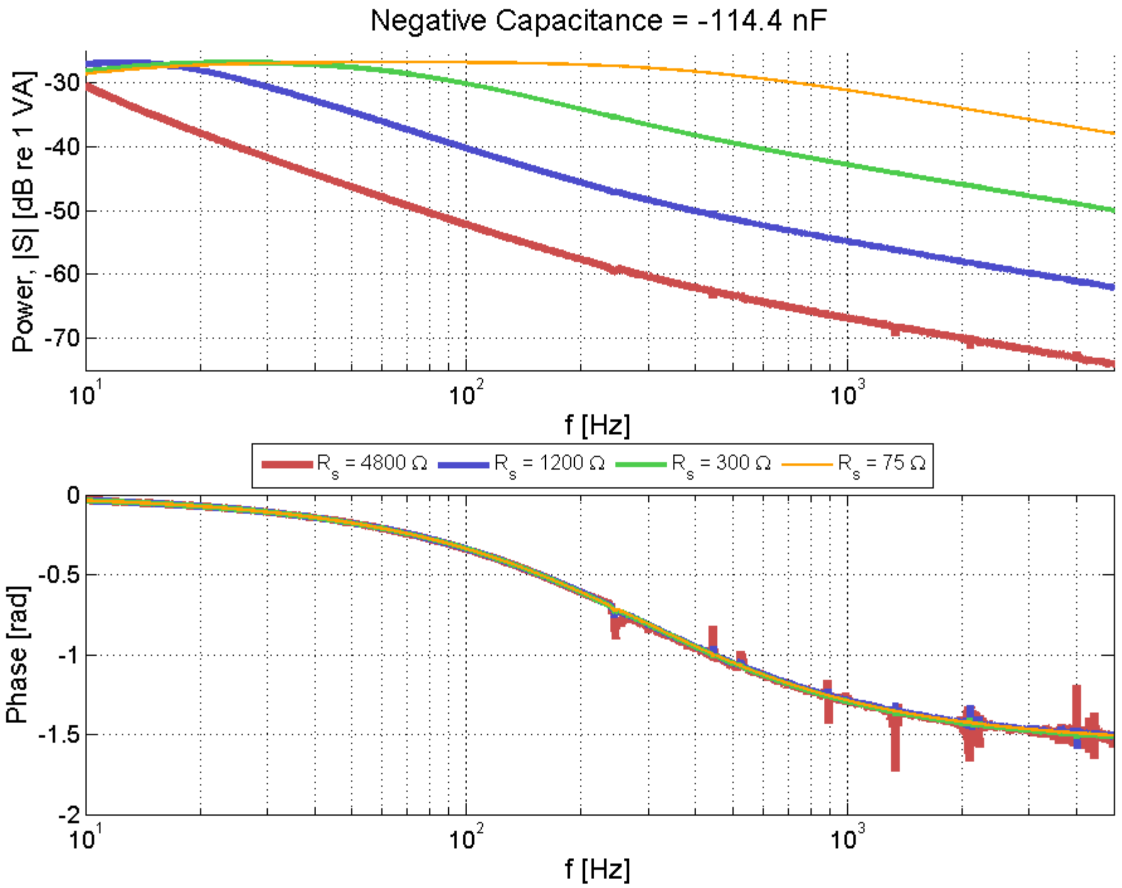

Figure 5.7 - Normalized experimental power output of the op-amp, amplitude and phase, for four values of series resistance

Table 5.2 - Total apparent power output of the op-amp for four resistor values, from 10-5000 Hz

Total Apparent Power [VA]			
$R_s = 4800\ \Omega$	$R_s = 1200\ \Omega$	$R_s = 300\ \Omega$	$R_s = 75\ \Omega$
0.008	0.045	0.242	1.008

Figure 5.4 shows the simulated power output of the op-amp for three values of negative capacitance and a series resistor of 300 Ω. In contrast to changing the resistor, the change in negative capacitance has more effect on the power magnitude at low frequencies and no effect at high frequency. Again, the phase of the power is not affected by negative capacitance. The tip response of the cantilever beam, seen in Figure 5.9, follows the trend of the simulated power output; where by decreasing the negative

capacitance magnitude increases the suppression especially at low frequencies. At high frequencies, there is no change in response for decreasing the negative capacitance magnitude. Figure 5.10 shows the measured power output of the op-amp. The power output does not change at high frequencies for different values of negative capacitance. The power output at low frequencies is reduced for some frequencies and increased for some frequencies. At the resonance, due to the reduction of the response the power output is reduced but the power for frequencies off resonance is increased. The phase of the power is consistent with the phase of the model and the normalized experimental power was again found to be consistent to the model. Table 5.3 shows the total measured power of the op-amp. The difference between the total output for the three negative values is much smaller than for the resistors. Specifically, it requires only 30.8% more power for the circuit to reduce the first resonance by 23 dB. Therefore, it takes substantially less power decrease low frequency resonances by decreasing negative capacitance than decreasing high frequency resonances by reducing the resistor.

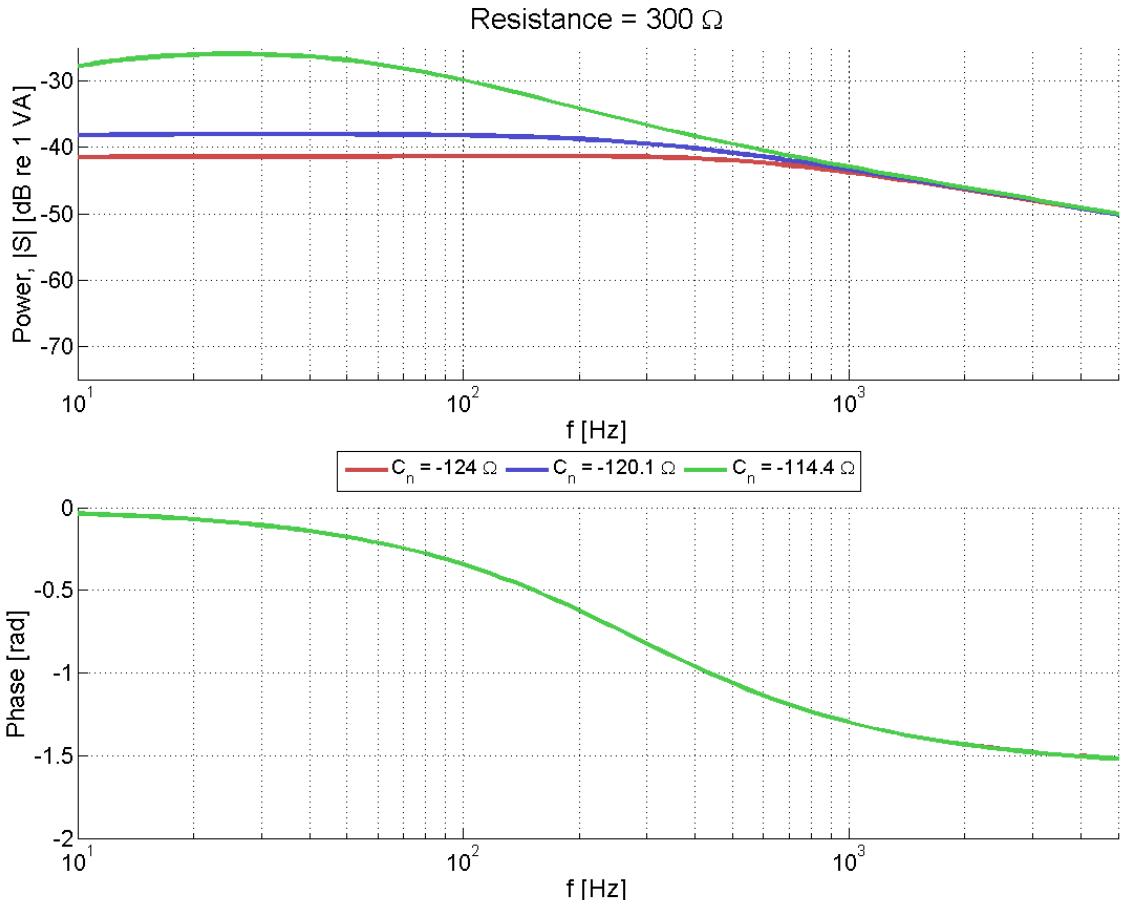

Figure 5.8 - Simulated power output and phase of the op-amp for three values of negative capacitance

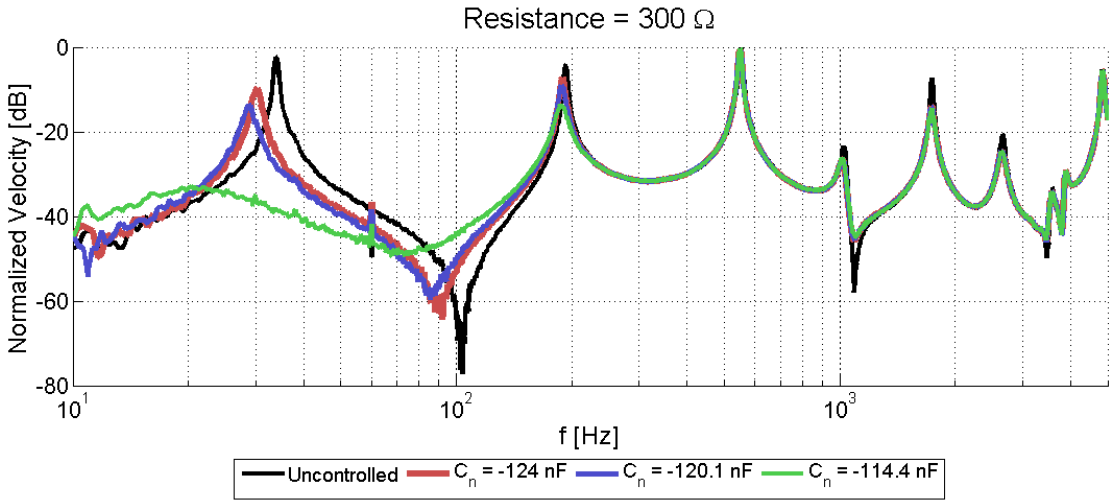

Figure 5.9 - Tip response of the beam for three values of negative capacitance

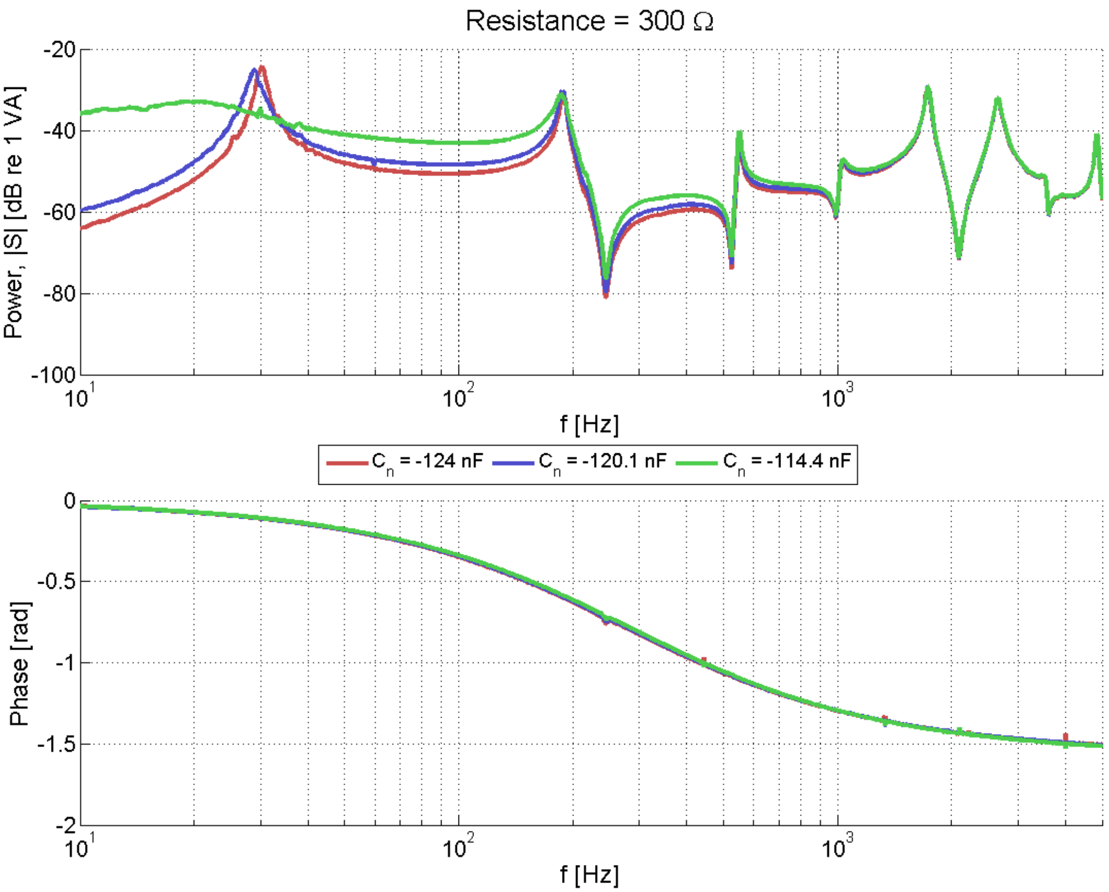

Figure 5.10 - Experimental power output and phase of the op-amp for three values of negative capacitance

Table 5.3 - Total apparent power output of the op-amp for three negative capacitance values, from 10-5000 Hz

Total Apparent Power [VA]		
C_n = -124 nF	**C_n = -120.1 nF**	**C_n = -114.4 nF**
0.185	0.203	0.242

5.2.3.2 Efficiency Improvements

As shown above, the Multisim model accurately predicts the power output behavior of a negative capacitance shunt, apart from resonance behavior. Therefore, it can be used to investigate how the choice in circuit parameters can increase the efficiency of the shunt by reducing the power output of the op-amp. Because the impedance desired is a negative capacitor, the phase of the power should be close to $-\pi/2$ rad, which is the phase of power for an ideal negative capacitor. Because of the fact that the phase of the power is not affected by the negative capacitance value or series resistor, the passive components used to create the negative capacitance will be analyzed to increase the efficiency of the shunt. The passive components of the shunt can be altered without changing the power of the shunt, therefore the efficiency can only be increased by reducing the power output of the op-amp.

To achieve a desired impedance with the negative capacitance shunt using Equation (5.3), the design space for choice of circuit elements is quite large. Yet, the choice of circuit elements affects the power output of the shunt. This is illustrated in Figure 5.11 which shows the power output of the op-amp versus the total potentiometer resistance

$$R_{pot} = R_3 + R_4 \tag{5.10}$$

for a single negative capacitance value and series resistance. The power output of the op-amp changes significantly with the value of R_{pot}. The 100 kΩ potentiometer has the smallest op-amp power output for this system. The phase of the power for that potentiometer is also the closest to that of the ideal negative capacitor. Similarly, power output for four values of reference capacitance C_2 is shown in Figure 5.12. The reference capacitor does not change the power output of the op-amp as much as the potentiometer. Yet, for this system a 110 nF capacitor results in power output of the op-amp with a phase that is closest to $-\pi/2$ rad for all frequencies. The 220 nF capacitor has slightly less power output for most frequencies.

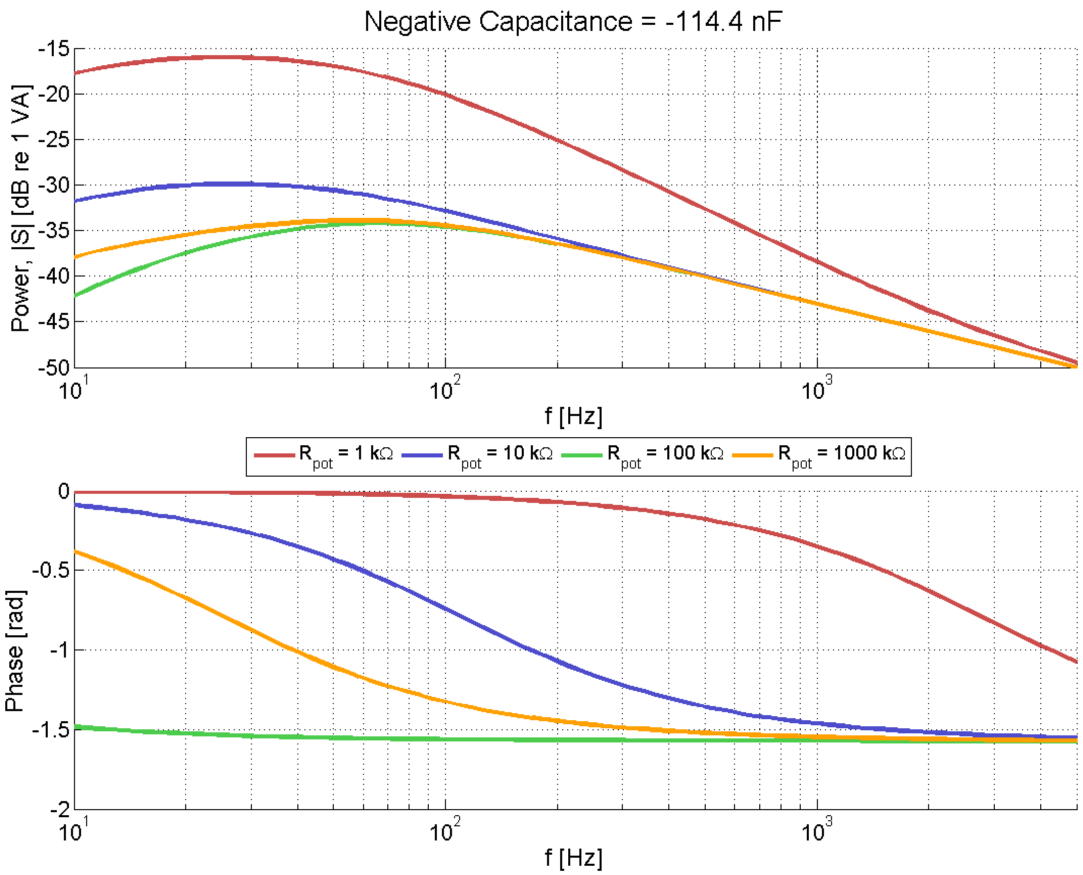

Figure 5.11 - Simulated power output versus frequency for four potentiometer values

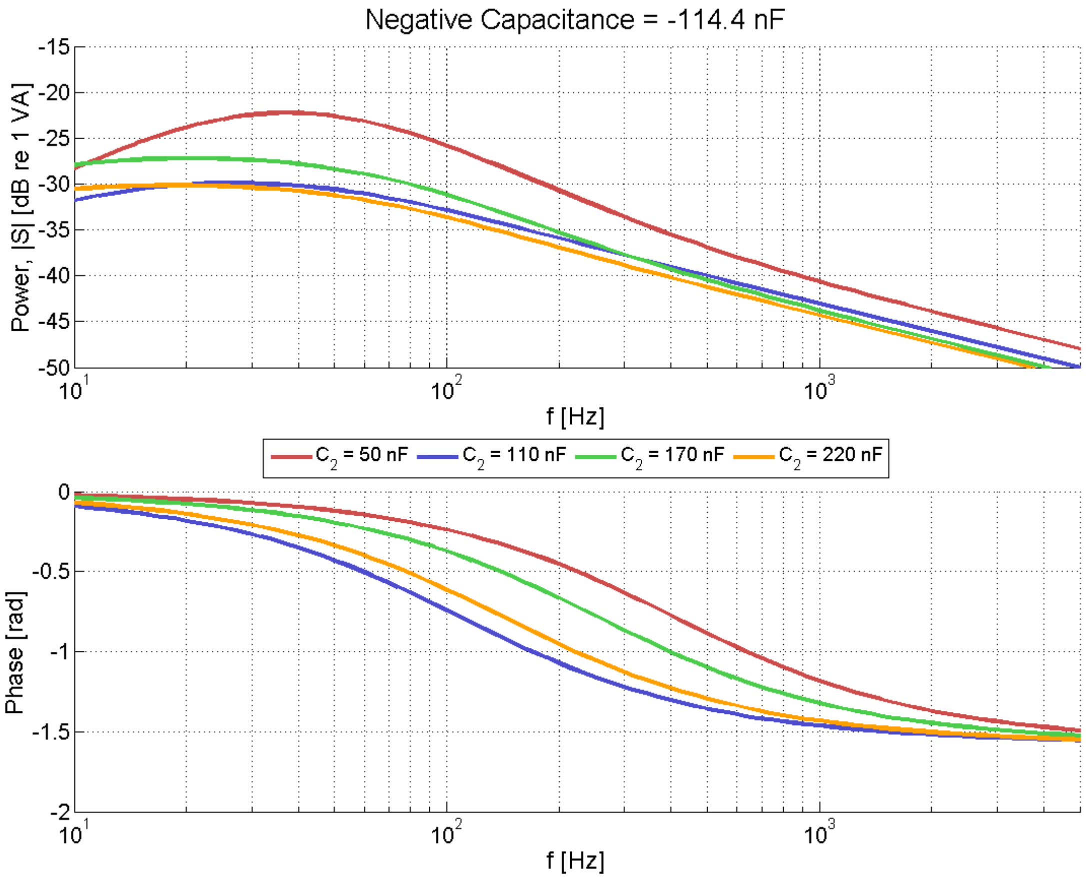

Figure 5.12 - Simulated power output versus frequency for four reference capacitor values

5.2.3.3 Circuit Limitations

Because the Multisim model includes an accurate model for op-amp behavior, the limitations of the shunt can be determined. During operation, the op-amp voltage and current are limited by the op-amp power supply and specifications. An analysis of the voltage output is presented here, but a similar investigation can be performed for the current limitations. For a constant amplitude disturbance voltage, the frequency at which the op-amp voltage is at a maximum is when the series resistance equals the real part of the negative impedance, where the negative impedance is

$$Z_2 = \frac{R_3}{R_4}\left[\frac{1}{R_2} + i\omega C_2\right]^{-1}. \tag{5.11}$$

Due to the fact that a large resistor is chosen for R_2 and R_s is small, the maximum voltage occurs at low frequency. Figure 5.13 shows the low-frequency voltage output of the op-amp for four values of series resistance. The frequency at which the maximum occurs moves to higher frequencies for smaller values of resistance. The amplitude of the maximum is the same for all values of series resistance. The magnitude of the peak voltage value is determined by the negative capacitance value, as shown by Figure 5.14. The maximum voltage increases as negative capacitance decreases. Yet, the increase is non-linear. The voltage peak increase exponentially as the negative capacitance magnitude approaches the simulated patch capacitance C_p. Therefore, the voltage response of the op-amp is sensitive to changes in negative capacitance near the patch capacitance.

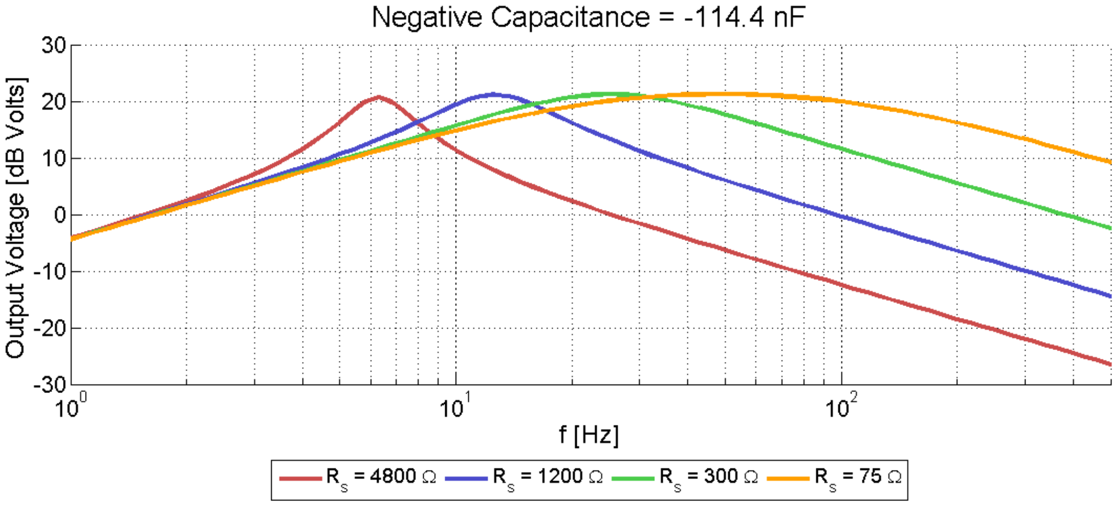

Figure 5.13 - Low frequency simulated voltage output versus frequency for four potentiometer values

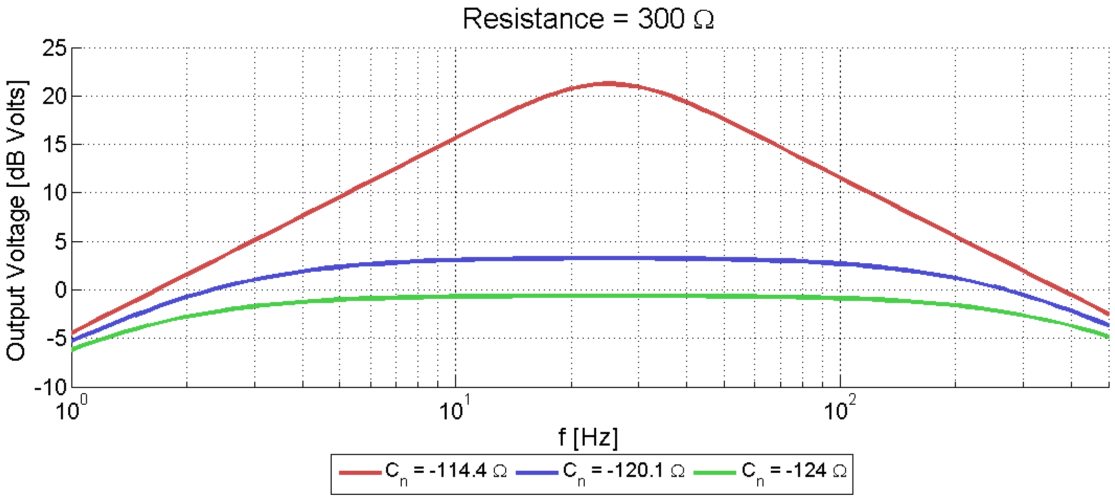

Figure 5.14 - Low frequency simulated voltage output versus frequency for four potentiometer values

The AC analysis of Multisim makes linear, harmonic assumptions to determine the circuit response. But, the circuit response becomes non-linear as the voltage output approaches the op-amp power supply voltage because of the voltage output limit of the op-amp. The non-linearity of the voltage output can be seen in Figure 5.15. The voltage response versus time for a single frequency is shown for three values of power supply voltage V_{ss}. For a 40 V power supply, the circuit behaves normally, but as the power supply voltage is reduced, the amplitude of the response is decreased due to clipping. For the 12 V supply, the response mimics that of an unstable circuit, even though circuit parameters allow for a stable response for the 40 V supply. Therefore, when a negative capacitance shunt is to be applied on a system, a circuit model should be used to determine the parameters and supply voltage that can be implemented for a given shunt to achieve a linear response for a given disturbance.

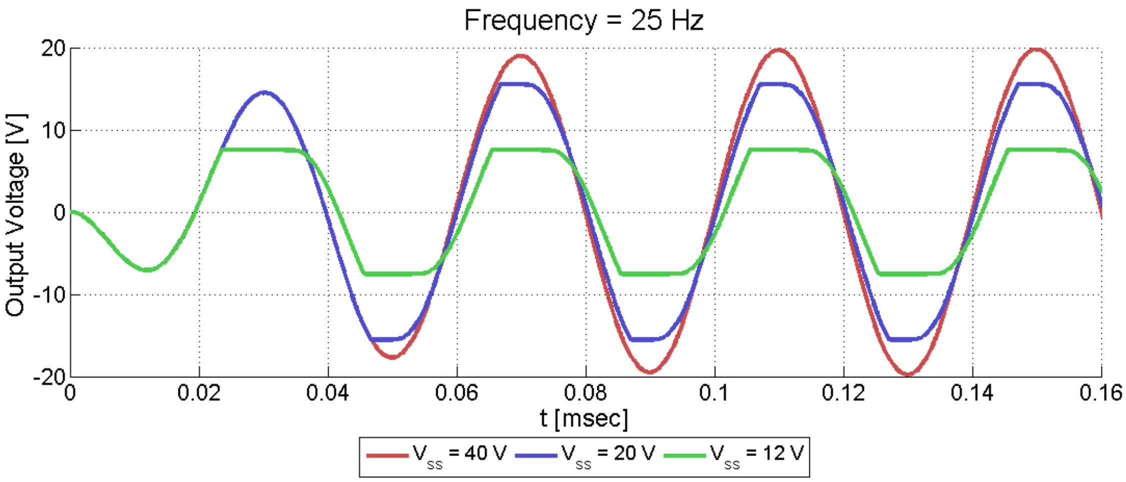

Figure 5.15 - Op-amp voltage output for three values of power supply voltage

5.3 Adaptive Tuning Theory

The inherent goal of vibration reduction using a shunted piezoelectric patch is to minimize the vibration response of a system to which the piezoelectric patch is bonded. When the response is reduced, the strain-induced voltage V_o created by the mechanical motion of the substrate is thereby reduced. Therefore, the components of the negative capacitance shunt should be tuned for maximum reduction of V_o which should correspond to maximum suppression of vibration of the substrate. Based on the results from modeling and measurement of the power output of the op-amp presented in the previous section, the following section outlines a process by which a negative capacitance shunt can be tuned to maximize vibration suppression. By determining the shunt parameters from the circuit response, the parameters can be adaptively tuned without needing an additional sensor to measure the response of the substrate.

The analysis used to determine the shunt parameters can also determine the voltage and current response at any point within the shunt. Through determination of the electrical response of the circuit, specifically the dissipated power in the series resistance, the concept of “cancellation” of the patch capacitance can be validated. If the negative capacitance truly cancels the inherent capacitance of the piezoelectric patch to maximize the power dissipated in the series resistor, the amount of power dissipated in the shunt will correlate to the magnitude of vibration suppression. Similarly, this correlation will corroborate the negative capacitance shunt tuning theory developed by Kim and Jung [66]. Their method calculated the optimal shunt parameters which corresponded to the maximum power dissipated in the resistor. This section will discuss the circuit analysis used to calculate the strain-induced voltage and will experimentally confirm the correlation between voltage reduction during negative capacitance shunt control and the suppression of a vibrating system.

5.3.1 Circuit Analysis

This section outlines an indirect measurement technique to compute V_o due to the fact that the strain-induced voltage V_o created by the vibrating substrate cannot be directly measured. As a reference, the uncontrolled V_o will be calculated first, which will act as a baseline for reduction. Figure 5.16 depicts a circuit schematic that will be used to describe the circuit values to calculate V_o. This circuit includes an electrical model of the piezoelectric patch connected to a resistor. The method to determine the impedance of the piezoelectric patch is detailed in the following section. A small resistor, with respect to the patch impedance, is chosen for R so as not to impart significant damping on the system.

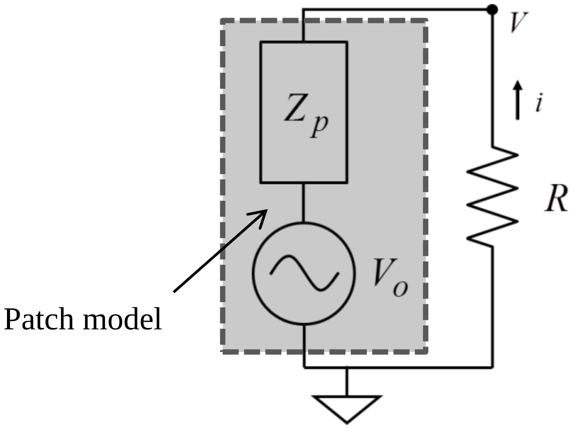

Figure 5.16 - Circuit schematic to determine uncontrolled strain-induced voltage

By measuring the voltage at point V with respect to ground, the current within the circuit can be calculated by

$$i = \frac{V}{R}. \tag{5.12}$$

With the current in the circuit and the voltage across the patch known, the uncontrolled strain-induced voltage can be found by

$$V_o = V + Z_p i. \tag{5.13}$$

Figure 5.17 shows the circuit schematic that describes the necessary circuit parameters to determine the strain-induced voltage V_o when a piezoelectric patch is attached to a negative capacitance shunt. For the analysis, the op-amp is assumed to be ideal. Therefore, the two golden rules of op-amp apply [21]:

I. The voltage difference between the two input terminals is negligible

II. The inputs draw no current.

Using the ideal op-amp assumptions, V_o can be computed from a single voltage measurement within shunt circuit. The circuit voltage response is measured with respect to ground at location V_a, as shown in Figure 5.17. From this measurement and Rule II, the current down the non-inverting branch i_+ is

$$i_+ = \frac{V_a}{R_3 + R_4}. \tag{5.14}$$

The voltage at the non-inverting terminal can then be found by

$$V_+ = V_a - i_+ R_4. \tag{5.15}$$

Utilizing Rule I, V_- is equal V_+. Therefore, the current down the inverting branch is computed as

$$i_- = \frac{V_+ - V_a}{Z_2} \tag{5.16}$$

where Z_2 is the reference capacitor in parallel with the large DC-stability resistor. Using Rule II again, the current in the inverting branch is equal to the current through the series resistor R_s and the patch impedance Z_p. Therefore, the strain-induced voltage is

$$V_o = V_+ + \left[R_s + Z_p\right] i_-. \tag{5.17}$$

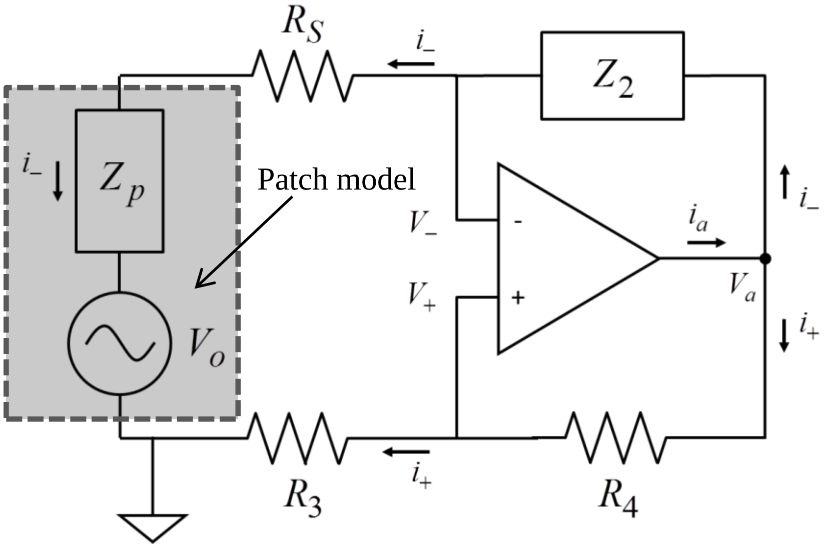

Figure 5.17 - Circuit schematic to determine controlled strain-induced voltage

Apart from the strain-induced voltage, the power dissipated in the series resistor is of interest. The shunt selection method introduced by Kim and Jung [66] outlined in Section 2.4.2 is based on the maximum dissipated power in the series resistor. The circuit analysis presented above can also be utilized to determine the power dissipated in the resistor, R_s

$$S_R = \left[i\_\bar{i}\_R_s \right]. \tag{5.18}$$

where the over-bar denotes the complex conjugate. Computing the power dissipated in the series resistor will permit a comparison between the tuning method proposed here and the method of maximum dissipated power, proposed by Kim and Jung [66].

5.3.2 Piezoelectric Patch Impedance Model

Many previous applications of piezoelectric shunt control utilize the electrical model shown in Figure 5.18a for a piezoelectric patch, which includes a strain-induced voltage, V_o, and the piezoelectric element modeled as a capacitor [10, 24, 38, 75, 91]. Yet, this model does not sufficiently represent the patch impedance when the real part of the patch impedance is on the same order of magnitude as the imaginary part of the patch impedance; a modified electrical model for the patch must be then used to accurately describe the frequency response of the patch. This situation can occur for frequencies near DC, typically below 50 Hz, or when capacitance of the patch is small, less than 10 nF. The modified model is shown in Figure 5.18b and includes a resistor in parallel with the capacitance of the patch. To determine the patch impedance, consider the frequency response function of a simple high pass filter, Figure 5.19, where the frequency response transfer function is equal to

$$\frac{V_{out}}{V_{in}} = \frac{R}{R + Z_p}. \tag{5.19}$$

Equation (5.19) can be rearranged to solve for the impedance of the patch

$$Z_p = R\left(\frac{V_{in}}{V_{out}} - 1\right). \tag{5.20}$$

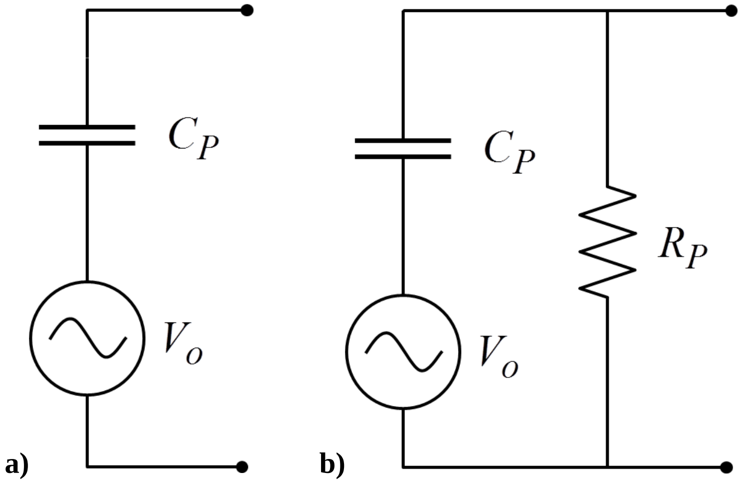

Figure 5.18 - Piezoelectric model a) traditional b) modified

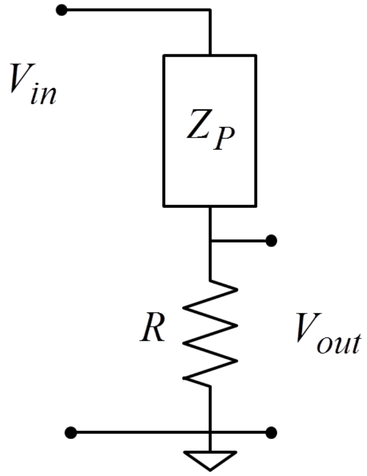

Figure 5.19 - High pass filter

When using this method to determine the impedance of the patch, it is best to measure the patch impedance before bonding it to the vibrating system. For in-situ measurement of the impedance, the effects of the structure must be removed through a frequency-dependent model of the patch impedance that does not include the structural resonances. To approximate the impedance of the patch versus frequency, due to the non-ideal nature of the piezoelectric impedance, the resistor and capacitor are modeled as frequency-dependent components. The frequency-dependent resistor must be added in parallel with the capacitor in the traditional piezoelectric model,

$$Z_p(\omega) = \frac{1}{\frac{1}{R_p(\omega)} + i\omega C_p(\omega)}, \tag{5.21}$$

where R_p and C_p are the frequency-dependent resistor and capacitor. This resistance can arise from the quality of the bond between the patch and substrate because the leads of the piezoelectric patches must be electrically isolated. When full electrical isolation is not present, some amount of inherent resistance may develop. Also, the piezoelectric material, PZT, can exhibit slight impedance nonlinearities [2]. The exact resistance and capacitance for each patch is measured and modeled ad-hoc. The model is then included in the calculation of the strain-induced disturbance voltage presented above.

5.3.3 Circuit Analysis Verification

A test circuit, shown in Figure 5.20, was constructed to verify the circuit analysis developed to compute the strain-induced voltage of a negative capacitance control patch. This circuit includes a negative capacitance shunt built using the method shown in Section 4.3. Attached to the negative capacitance shunt is circuitry that simulates a piezoelectric element: a capacitor C_p in series with a voltage source V_D in parallel with a resistor R_p. The circuit components are outlined in Table 5.4. Using this circuit, the calculated value of V_o can be compared to a known supplied voltage V_D which is driven from an external source.

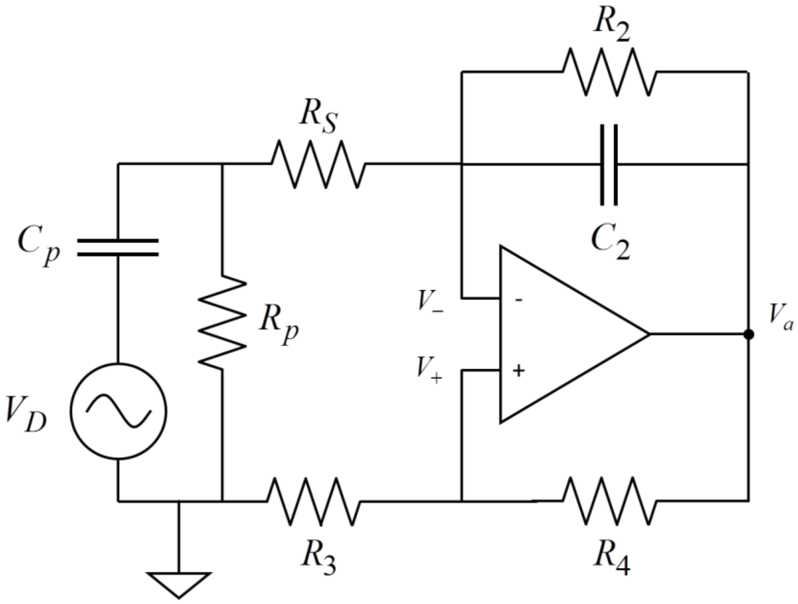

Figure 5.20 - Circuit schematic to verify circuit analysis

Table 5.4 - Verification circuit parameters

V_D	0.04 V
C_p	96.5 nF
R_p	10.62 MΩ
C_2	110 nF
R_2	10.68 MΩ
$R_3 + R_4$	10.21 kΩ

Due to the active and unstable nature of the shunt, precautions were taken to insure that the measurement of the response did not affect the performance of the shunt. The measurement of the voltage at point V_a was measured using a 10x attenuating voltage probe with respect to ground. Due to the fact that the probe is in parallel electrically with both the positive and negative branches of the op-amp, the impedance does not need to be included in the analysis. A Siglab system was used for both a data recording device as well as the voltage generator which supplies V_D. The magnitude and phase of the frequency response of the computed voltage output V_o are normalized by the known driving output voltage V_D for four values of shunt resistance R_S, plotted in Figure 5.21.

The computed V_o closely matches the driving voltage, where the maximum error of the magnitude is 4%. Similarly, there is little error associated with the phase. The errors are more than likely due to a small equivalent resistance in the capacitor, which was modeled as ideal. Therefore, the circuit analysis presented above has been shown to be an accurate method to predict the strain-induced voltage of a vibrating piezoelectric patch connected to a negative capacitance shunt.

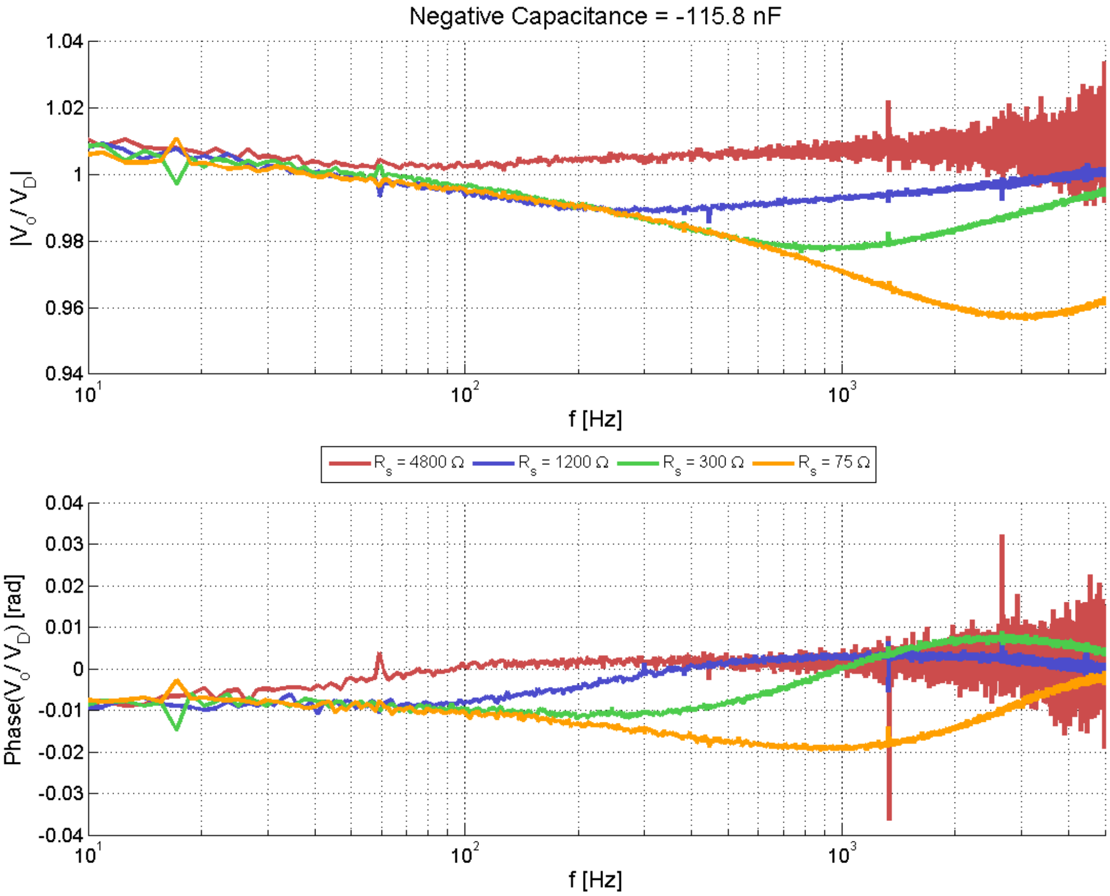

Figure 5.21 - Frequency response of the computed voltage output verification

5.3.4 Control implementation and results

The control analysis presented above was applied to the same aluminum cantilever beam described in Section 4.4.1. The velocity of the tip of the beam was measured to obtain a metric to describe the reduction in vibration to verify the tuning method. Data on the electrical and mechanical responses of the cantilever beam and the shunt circuit was acquired using a system consisting of function generator, the piezoelectric drive patch pair, and a recording device to measure the electrical response of the circuit and the velocity of the tip of the beam. The beam was driven using a chirp signal from 10 to 5000 Hz.

The tip response of the beam and the computed strain-induced voltage is presented for various shunt configurations. Due to the fact that most of the vibrational energy of the system occurs at the resonance frequencies, the analysis will focus on bands of frequencies near resonances. Figure 5.22 shows the tip velocity frequency response and computed strain-induced voltage for three values of negative capacitance. The series resistance is 300 Ω for all cases where the shunt is utilized. The uncontrolled tip response is the open circuit response. The uncontrolled V_o was acquired using a 1100 Ω resistor as described in Section 5.3.1.

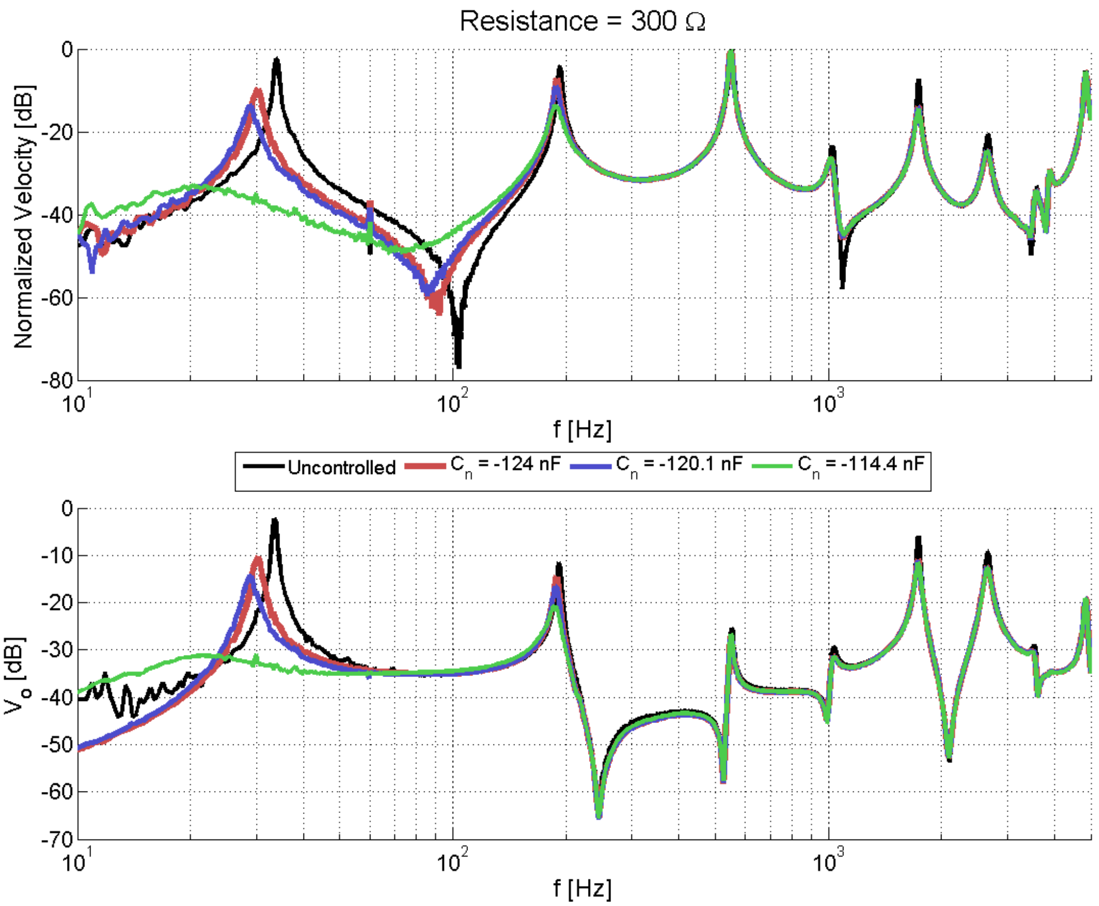

Figure 5.22 - Tip response and strain-induced voltage for three negative capacitance values

As the negative capacitance magnitude decreases, the normalized velocity is decreased for all frequencies, with greater effect at the low frequency resonances. The same behavior is seen in the calculated V_o. There is a proportional decrease in velocity and tip velocity. Most importantly, the negative capacitance value that corresponds to the largest reduction in V_o is the same value that corresponds to largest reduction in tip velocity.

Figure 5.23 shows the tip velocity response and the strain-induced voltage for four values of series resistance. The negative capacitance value for the four controlled responses is -114 nF. Whereas the negative capacitance increased the suppression for all frequencies, the resistor value alters the frequency where more suppression is achieved.

Large resistors exhibit more reduction at low frequencies and the small resistors increase suppression at high frequencies with a slight decrease in performance at low frequency. Again, the computed V_o is consistent with this frequency behavior. Both the resistor and negative capacitance value that minimizes the computed strain-induced voltage V_o minimizes the response of the beam. Therefore, the shunt parameters can be chosen by minimizing V_o and can be adaptively chosen based on the minimization of V_o.

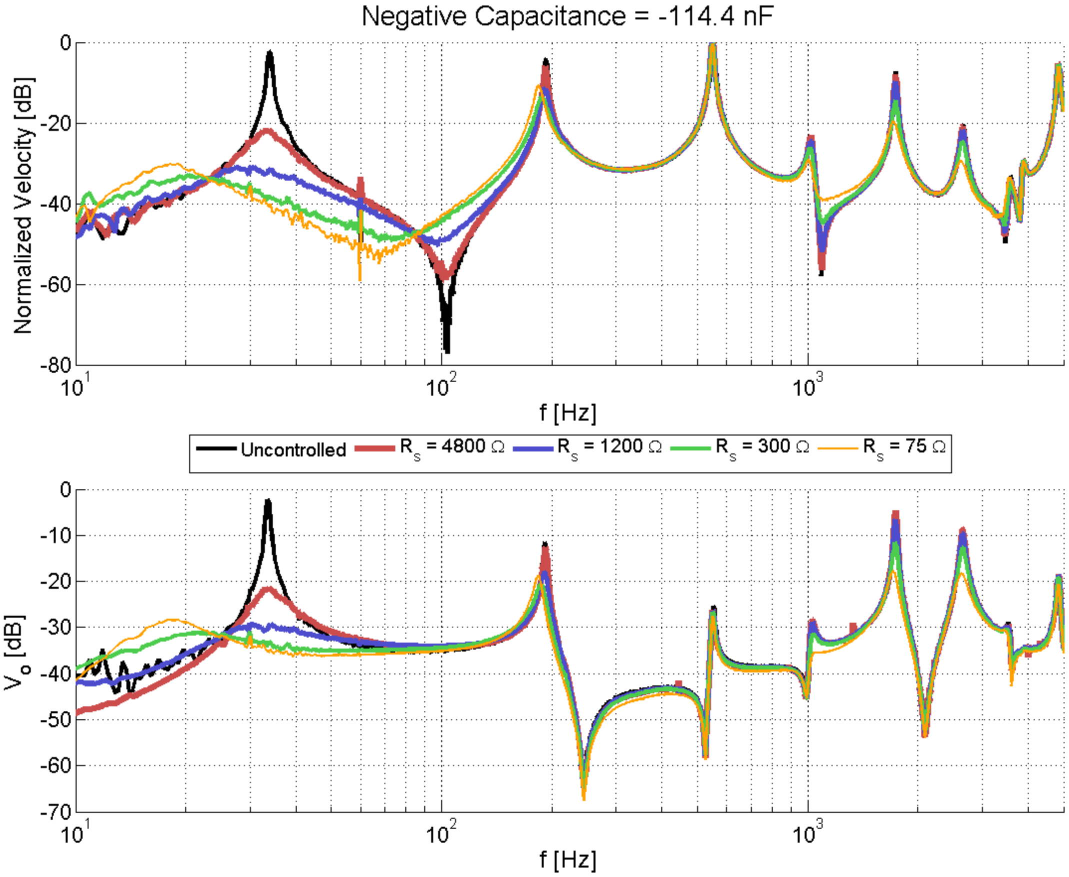

Figure 5.23 - Tip response and strain-induced voltage for four resistance values

To compare the tuning method presented in this section and the maximum power dissipated method of Kim and Jung, the power dissipated in the series resistor is plotted in Figure 5.24 for the same four series resistors presented above. The resistor that exhibits the greatest power dissipated for the resonance at 30 Hz is the 4800 Ω resistor. For the higher frequency resonances, the 1200, 300, and 75 Ω resistors dissipate similar amounts of power. This behavior is in contrast to the change in tip response shown above, where the smallest resistor value causes the circuit to suppress the response significantly more. Therefore, the power dissipated in the series resistor does not correlate to the amount of suppression of the beam, which contradicts Kim and Jung. Yet, in light of the fact that the strain-induced voltage is reduced because of the control of the shunt circuit, the power can be normalized by the computed voltage V_o

$$S_N = \frac{S_R}{V_o^2} \tag{5.22}$$

where S_R is the power dissipated in the resistor. Figure 5.25 shows the normalized power dissipated in the series resistor. The normalized power shows a correlation between the amount of suppression for frequencies above 100 Hz. For instance, the negative capacitance shunt circuit with the 300 Ω resistor yields the largest reduction in vibration and the largest value of normalized power at the resonance at 190 Hz. Yet, below 100 Hz the resistors that cause the greatest suppression do not yield the greatest normalized power. This is most likely due to the fact that the change in stiffness caused by the shunt has more effect on reducing vibration than the added damping of the resistor. Therefore, the normalized power cannot be used to predict the resistor value that maximizes the vibration suppression of a negative capacitance shunt. Ultimately, the results refute the maximum power dissipation method developed by Kim and Jung [66]

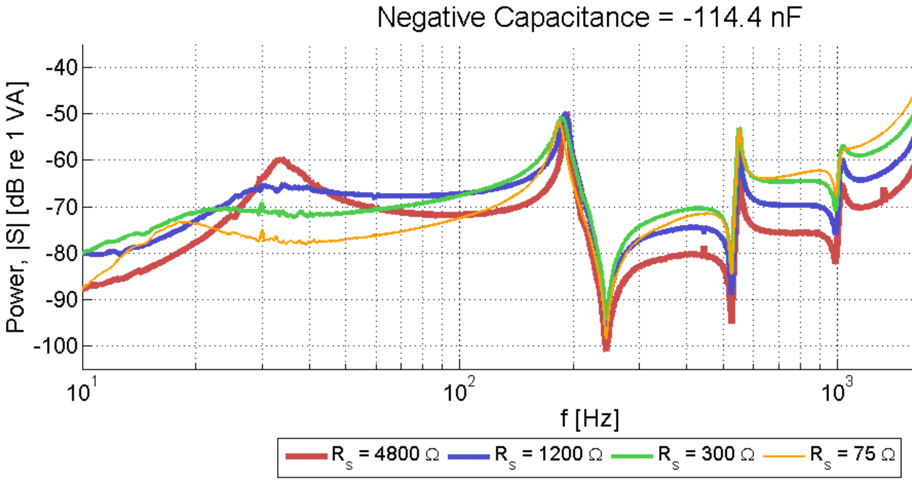

Figure 5.24 - Power dissipated in the series resistor

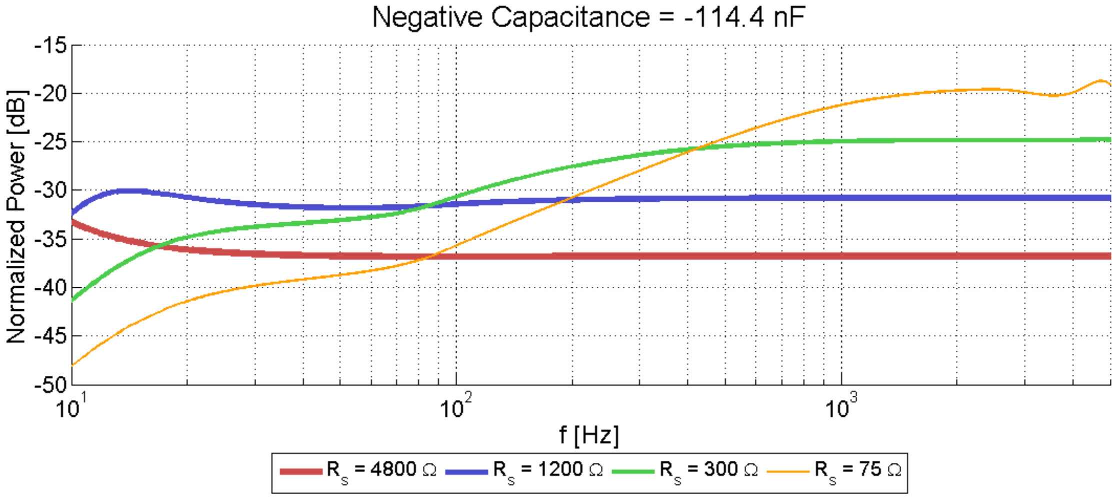

Figure 5.25 - Normalized power in the series resistor

5.4 Circuit Stability

As stated in Chapter 2, the reasons behind shunt parameters which yield unstable a negative capacitance circuit need to be identified and modeled to aid in the prediction of vibration suppression. A process is developed here that predicts the magnitude of negative capacitance that is attainable experimentally given the measured electrical impedance of a patch and uncontrolled voltage response. Two problems that limit the effectiveness of the overall control system are explored: the issues surrounding the variation in patch impedance and the voltage limitations of the op-amp. This section first defines the stability of the shunt, then discusses the impact of the voltage output of the op-amp. An experimental test structure is introduced and the variation in patch impedance is quantified. Finally, the results and analysis are given.

5.4.1 Stability Condition

To obtain maximum performance, appropriate circuit component values must be chosen to reach the necessary negative capacitance. The values of these components are limited by concerns regarding the stability of the circuit; where a stable circuit is considered a circuit configuration that has a non-saturated output. To determine stability of the circuit, one must consider the two following requirements [21]:

i. There must be feedback current to the inverting terminal at DC
ii. The voltage gain down the negative feedback path must be larger than the voltage gain down the positive feedback path

The first condition prevents a bias voltage occurring that would cause the circuit output to drift until the output equaled the supply voltage. The second condition ensures that the harmonic feedback is stable and can be addressed with by the processes outline by Date *et al.* [52].

Date *et al.* analyzed the negative impedance converter circuit in Figure 5.26, where the input to both the inverting and non-inverting terminals of the op-amp are considered as ideal voltage dividers from the output voltage to ground. The voltage gain down the inverting path is

$$V^{-} = \frac{Z_1}{Z_1 + Z_2} V_{out} \,. \tag{5.23}$$

Likewise, the gain for the non-inverting path is

$$V^{+} = \frac{Z_3}{Z_3 + Z_4} V_{out} \, . \tag{5.24}$$

The third voltage relationship considers the voltage difference across the inputs which is

$$V^{+} - V^{-} = \left[\frac{Z_3}{Z_3 + Z_4} - \frac{Z_1}{Z_1 + Z_2} \right] V_{out} \, . \tag{5.25}$$

Returning to the second stability requirement, the voltage gain down the inverting path must be greater than the gain down the non-inverting path; thus, the sign of the coefficient of V_{out} in Equation (5.25) must be negative. Therefore, Equation (5.25) can be simplified to

$$\frac{Z_1}{Z_1 + Z_2} > \frac{Z_3}{Z_3 + Z_4} \, . \tag{5.26}$$

which can be reduced to

$$\frac{Z_2}{Z_1} < \frac{Z_4}{Z_3} \, . \tag{5.27}$$

A stable circuit will have the expression above be true all frequencies. If it is assumed for a Type 1 negative capacitance circuit that both Z_1 and Z_2 are ideal capacitors only, the stability condition becomes

$$\frac{C_p}{C_2} < \frac{R_4}{R_3} \tag{5.28}$$

where C_p is the capacitance of the piezoelectric patch and C_2 is the reference capacitor, which is the definition of stability that is specified by Date *et al*. The determination of a stable circuit is straightforward because Equation (5.28) is independent of frequency and purely real. This will be considered the traditional estimation of instability. Yet, if all the components of the circuit are included in Equation (5.27), the stability condition becomes

$$\frac{1}{\left(Z_p + R_s\right)\left(i\omega C_2 + \frac{1}{R_2}\right)} < \frac{R_4}{R_3} \tag{5.29}$$

where Z_p is the frequency-dependent patch impedance, R_s is the series resistance, and R_2 is the reference resistor in parallel with the reference capacitor C_2. The left-hand side of the expression is both frequency-dependent and complex while the right-hand side is purely real. The stability, therefore, needs to be defined in terms of a complex quantity. The stability condition is

$$\arg\left(\left[\left(Z_p + R_s\right)\left(i\omega C_2 + \frac{1}{R_2}\right)\right]^{-1} - \frac{R_4}{R_3}\right) \neq 0 \tag{5.30}$$

which is analogous to the requirement in control theory that requires the poles be located in the left-half of the complex plane.

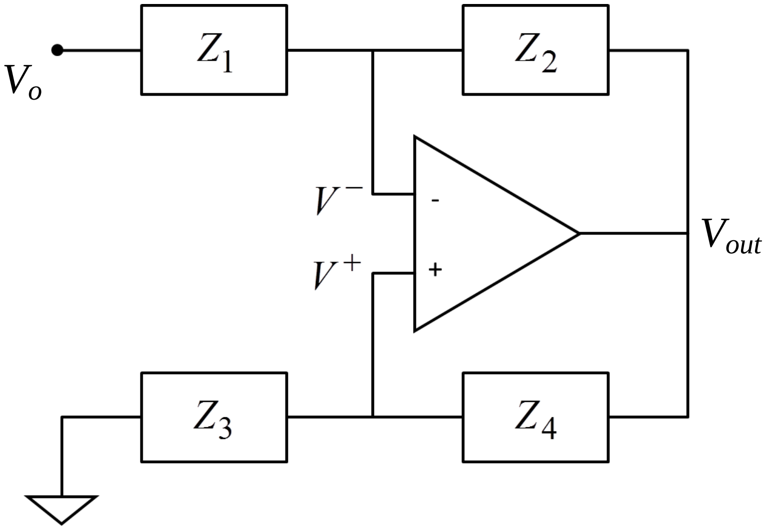

Figure 5.26 - Basic negative impedance converter with input impedance

Equation (5.30) can be used to predict the values of negative capacitance and series resistance for which the circuit will be stable for a given patch. Based on the patch location, impedance, and size, control can be predicted from stable circuit impedances.

5.4.2 Voltage Gain Limitation

As was shown in Section 5.2.3.3, the output voltage of the op-amp in the negative capacitance circuit is limited by the power supply voltage. Therefore, a prediction of the output voltage of the op-amp for a given value of negative capacitance needs to be made to estimate experimentally-attainable shunt configurations. To that end, the strain-induced voltage disturbance on the shunt must be related to the output voltage of the op-amp. The gain G of the circuit can be calculated by [52]

$$G = \left[\frac{Z_3}{Z_3 + Z_4} - \frac{Z_1}{Z_1 + Z_2} \right]^{-1} . \tag{5.31}$$

The goal of the op-amp is the drive the output voltage to a state where there is equal voltage drop down both the inverting and non-inverting branches of the circuit. Considering Figure 5.26, if there is equal voltage drop from V_o to V_{out} and V_{out} to ground, then the predicted voltage output can be estimated by

$$V_{out} = G \frac{V_o}{2} \tag{5.32}$$

where V_o is the uncontrolled strain-induced voltage. The strain-induced voltage can be measured using the process outlined in Section 5.3.1. With the addition of an output voltage limitation in the stability prediction model, the experimentally-attainable circuit parameters can be more accurately estimated. The voltage limit of an OPA445 op-amp used for implementation with a ±35 V supply voltage is 30 V.

5.4.3 Periodic Beam

To investigate the effects of stability and test the prediction method on patch impedance, an experimental test beam was created. The experimental setup consists of a cantilevered aluminum beam with a periodic array of 10 evenly-spaced piezoelectric patches, with nominally consistent patch properties. The physical parameters of the beam and patches are shown in Table 5.5. The patch capacitance listed in the table was obtained with a multimeter measurement, and all patches were measured to have the same capacitance with the given precision. The multimeter measurement obtains the imaginary component of the impedance for a single frequency, where a frequency dependent measurement of impedance may be necessary to fully characterize the electrical properties of the patches. The beam is cantilevered at the root with the array of patches extending at equal intervals of 20 mm. Each patch is considered to have been produced and bonded with identical procedures. The experimental procedure outlined in Section 5.3.3 was used here to measure and record the tip response of the beam and voltage response of the negative capacitance shunt. Patch number 10 was used to drive the beam.

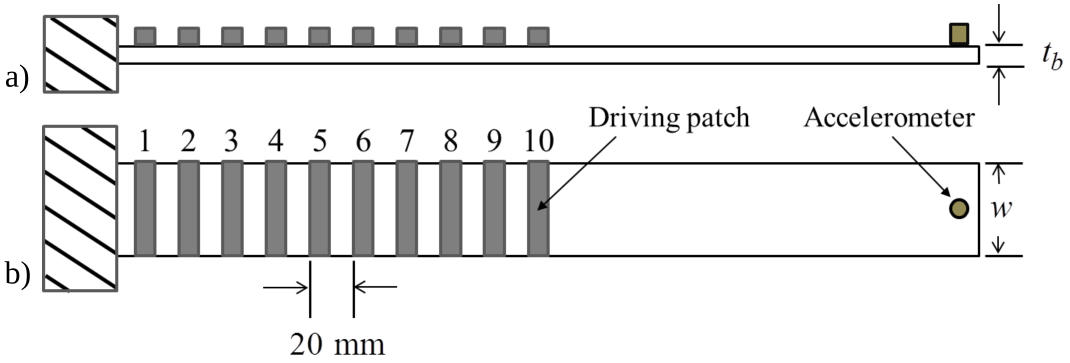

Figure 5.27 - a) Top view and b) side view of a 410 mm long cantilever beam with 10-element periodic array of piezoelectric patches at 20 mm spacing.

Table 5.5 - Beam and patch physical parameters

Beam	Young's modulus	E_b = 73 Gpa
	Density	ρ_b = 2700 kg/m^3
	Thickness	t_b = 2 mm
	Width	w = 30 mm
	Length	L = 410 mm
Piezoelectric	Young's modulus, shorted	E_p = 63 Gpa
Patch	Density	ρ_p = 7800 kg/m3
	Coupling coefficient	k_{31}= 0.35
	Thickness	t = 1.3 mm
	Capacitance	C_p = 2.4 nF

5.4.3.1 Patch Impedance Variation

The method presented in 5.3.2 was used to determine the frequency-dependent patch impedance of all the patches in the array in-situ. Figure 5.28 shows the parallel capacitance C_p and resistance R_p of four representative patches. The solid lines correspond to the experimentally-measured impedance, and the dashed lines are the smoothed-impedance model. For an ideal capacitor, the capacitance is constant with frequency and the resistance is infinite. Yet, all the patches in the array deviate from an ideal capacitor in both resistance and capacitance. Similarly, the variation in patch impedance both versus frequency and across patch number is significant.

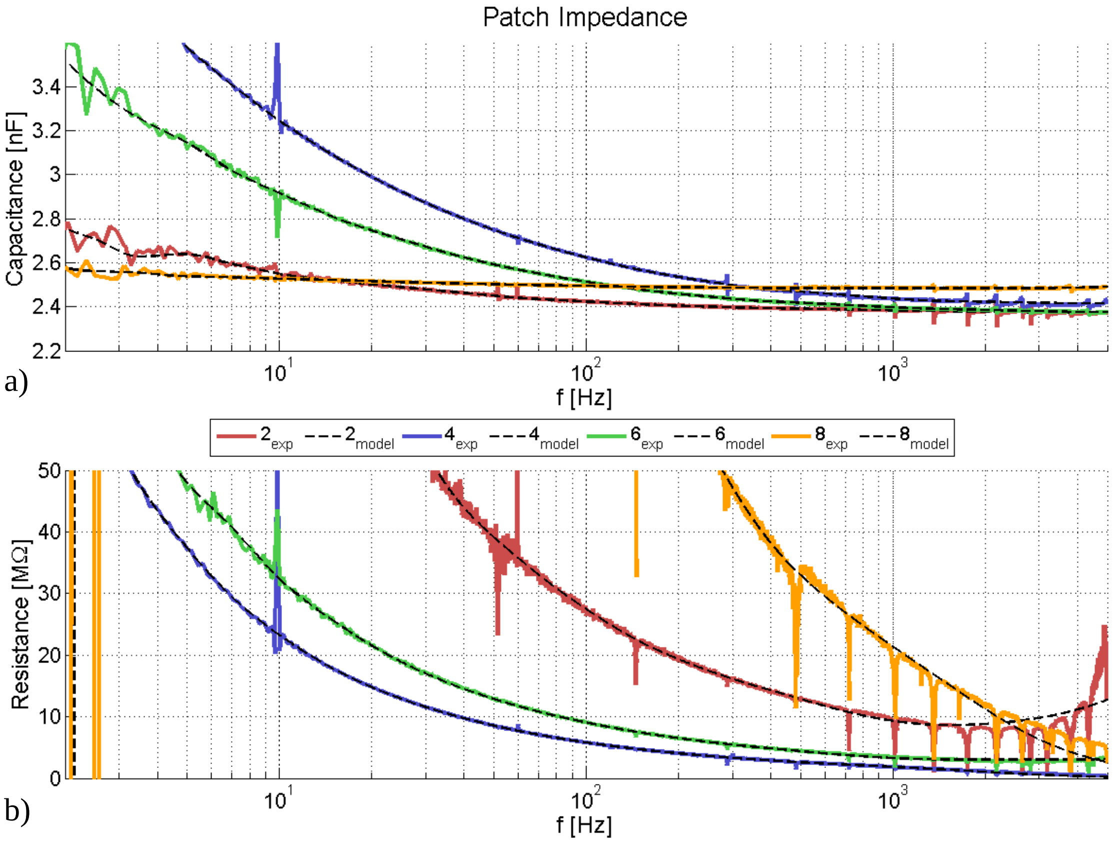

Figure 5.28 - Patch a) capacitance and b) resistance versus frequency

For comparison of shunt parameters between patches and against frequency, the negative capacitance ratio, or NCR, defined in Equation (4.6), will be used. Also, NCR will be a frequency-dependent quantity because the patches are not ideal capacitors.

5.4.4 Results and Analysis

To apply the prediction method to these patches, as well as the stability analysis versus achievable suppression, Patch 2 and patch 6 were chosen to analyze the results of the shunt parameter prediction method and comparison of tip response for stable values of negative capacitance and resistance. These two patches were chosen because their capacitance magnitudes are equal at high frequency.

5.4.4.1 *Model verification parameters*

To test method developed above to predict what components will yield a stable response, a resistance ratio, α, is maximized for a chosen reference capacitor and resistor to satisfy the restrictions of stability and on the magnitude of op-amp output voltage, where

$$\alpha = \frac{R_3}{R_3 + R_4}. \tag{5.33}$$

By maximizing α subject to the stability and output constraints, the NCR will be minimized which corresponds to maximum achievable suppression. The resistance ratio α will also be determined using the traditional method for shunt stability, Equation (5.28), and will be compared to the predicted and experimentally-obtained values. The comparison will be made in terms of the percent error of the experimental value

$$\varepsilon = \frac{\alpha_{ex} - \alpha_{cal}}{\alpha_{ex}} \times 100 \tag{5.34}$$

where α_{ex} denotes the experimental value and α_{cal} is the calculated value, either using the traditional or prediction method. A positive ε corresponds to an over-prediction of NCR, and a negative ε is an under-prediction. Similarly, the sign of the error denotes if the calculated α will cause an unstable response in the circuit. Positive values of α indicate an unstable circuit configuration. In addition to α, the predicted output voltage, computed by Equation (5.32), will be compared to the experimental output voltage of the op-amp V_{out} to validate the electrical behavior of the model.

The attainable circuit parameters of the model can be used to determine the shunt impedance versus frequency which allows for a qualitative comparison of control between patches. Qualitatively, an NCR closest to one will obtain more control. The optimal total resistance for the shunt decreases as frequency increases, where total resistance is computed by

$$R_{total} = \mathrm{Re}\left[Z_1\right] - \mathrm{Re}\left[\frac{Z_2 Z_3}{Z_4}\right] \tag{5.35}$$

Also, at a given frequency, a larger resistance is necessary to obtain more suppression for larger values of NCR [92]. Also, the sign of the error, computed by Equation (5.34), will indicate an under- and over-prediction of suppression respectively.

5.4.4.2 *Effect of α on stability*

Figure 5.29 shows the argument of the stability condition, Equation (5.30), versus for four values of α which illustrates the effect of α on the stability. As stated above, to retain a stable response, the argument cannot equal zero at any frequency. For small values of α, the argument does not zero which corresponds to a stable configuration. Yet, as α increases to a value greater than 0.616, the circuit will become unstable, as shown by α equal to 0.619. The NCR for the same four values of α are shown in Figure 5.30. There is a difference of 0.015 between each of the curves. In terms of suppression, this difference can cause significant reduction. Also, for the current circuit realization, the resistance difference between the highest and lowest α is less than one quarter turn of the potentiometer. Therefore, it may be difficult to experimentally obtain a desired impedance.

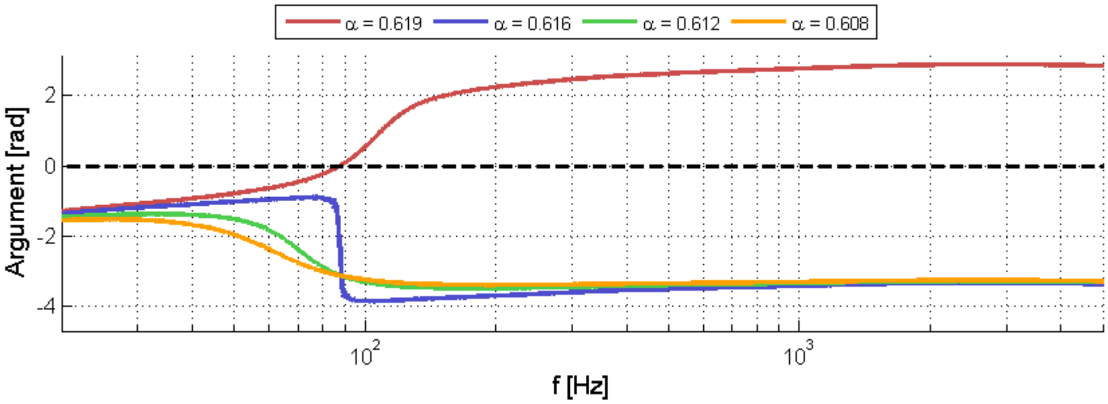

Figure 5.29 - Argument of the stability condition for four values of *α*, for a shunt connected to patch 6

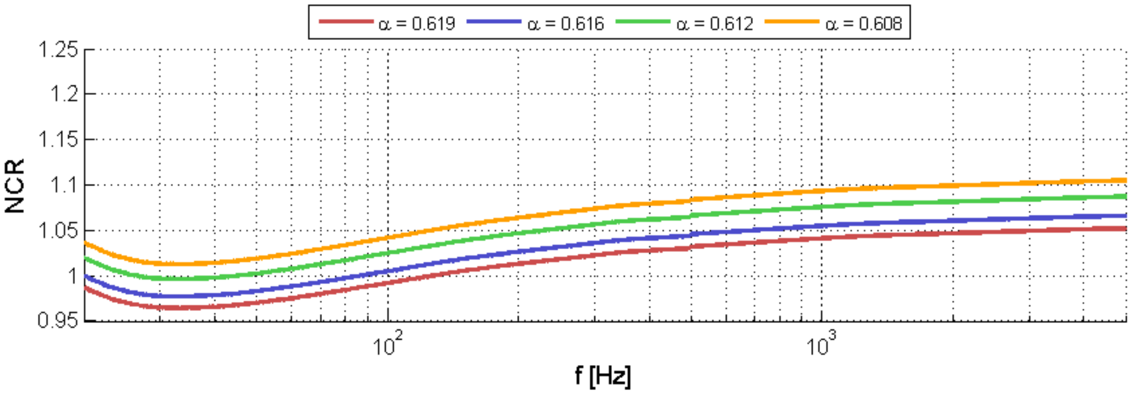

Figure 5.30 - NCR for four values of *α*, for a shunt connected to patch 6

5.4.4.3 Stability prediction of α and the effect on shunt impedance

The predicted voltage output of the op-amp from the stability model and experimental measurements is shown in Figure 5.31 for patch 6. The voltages are shown for four values of reference capacitance at the limit of stability; all other circuit components are held constant. The predicted, traditional, and experimentally obtained α are shown in Table 5.6, along with their associated percent error. The predicted voltage output of the op-amp matches closely with the measured output voltage, which confirms the ability of the model to predict voltage response of the op-amp. For the three largest reference capacitors, the predicted α from the stability prediction method has an error below 0.34% of the experimental value, which confirms the ability of the model to predict stability. The error is also within the precision of the multimeter used to measure the resistance of the potentiometer. The stability prediction method yields an estimate of the maximum attainable α that is 2-10 times more accurate than the traditional method.

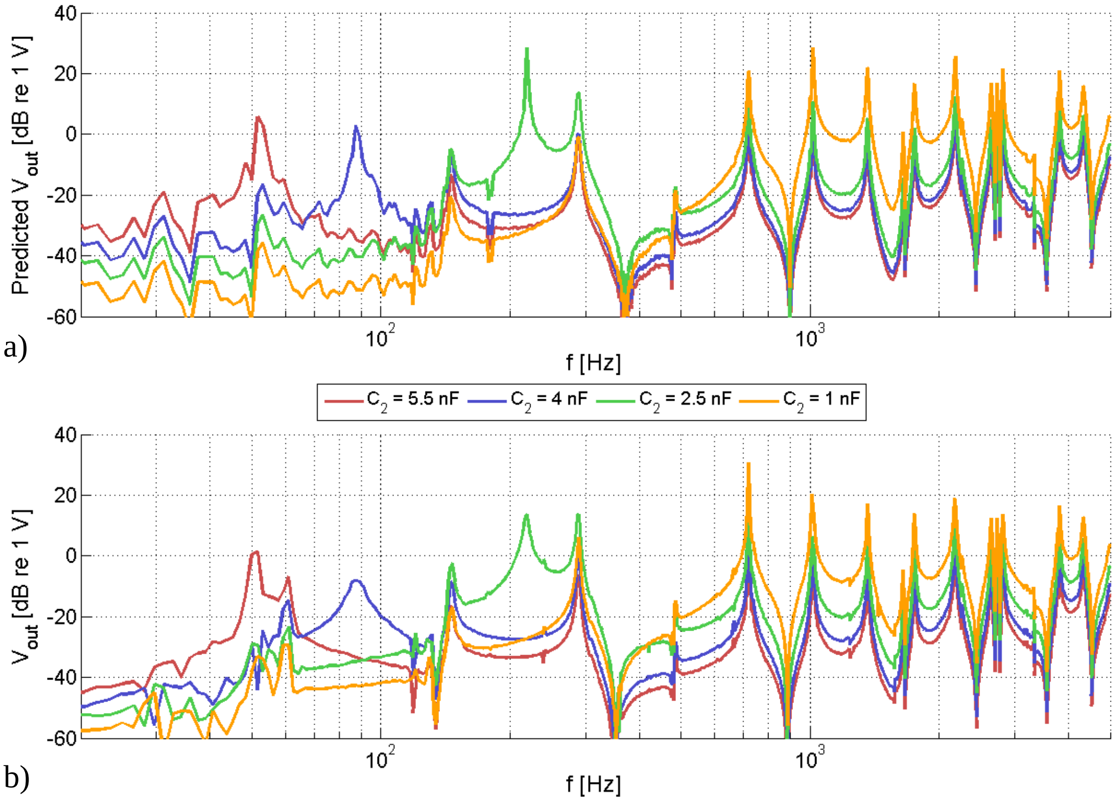

Figure 5.31 - Comparison of a) predicted op-amp output voltage and b) measured output voltage for patch 6

Table 5.6 - Predicted, traditional, and experimental resistance ratio α at the stability limit and their associated percent error for patch 6

	C_2 = 5.5 nF	C_2 = 4.0 nF	C_2 = 2.5 nF	C_2 = 1.5 nF
Predicted	0.682	0.616	0.510	0.302
Traditional	0.694	0.623	0.508	0.292
Experimental	0.681	0.615	0.508	0.299
ε, Pred. (%)	0.21	0.24	0.34	1.07
ε, Trad. (%)	2.03	1.33	0.00	-2.16

Table 5.7 - Predicted, traditional, and experimental resistance ratio α at the stability limit and their associated percent error for patch 2

	C_2 = 5.5 nF	C_2 = 4.0 nF	C_2 = 2.5 nF	C_2 = 1.5 nF
Predicted	0.697	0.628	0.516	0.302
Traditional	0.694	0.623	0.508	0.292
Experimental	0.695	0.627	0.514	0.301
ε, Pred. (%)	0.31	0.26	0.42	0.39
ε, Trad. (%)	-0.09	-0.58	-1.11	-2.75

As shown in Table 5.6, the predicted α values exhibit a bias toward larger values than the experimentally obtained values for patch 6. Therefore, the predicted value corresponds to an unstable circuit. The bias is most likely because of the imprecision of the potentiometer during tuning to achieve a maximum value of α while retaining stability. If a more accurate method of tuning α was utilized, it is expected that the error between predicted and experimental values would be reduced. In contrast, the traditional method estimates both larger and smaller values of α. This leads to the fact that the parameters calculated from the tradition method for will either significantly under- or over-predict the point of instability compared to the proposed prediction method. For example, when C_2 = 5.5 nF, the traditional calculates instability at a point much greater than attainable. In contrast, when C_2 = 1.5 nF the traditional method yields a significantly under-predicted stability point. When the same circuits are connected to patch 2, which is a seemingly identical patch, the traditional method under-predicts stability for all cases as shown in Table 5.7. In contrast, the proposed prediction method obtains values for an unstable circuit, but much closer to the experimental value. The trend is also more consistent between circuit configurations than the traditional method.

The predicted α for the 1.0 nF reference capacitor exhibits an error of 1.07% which can be accounted for by the increased experimental voltage response of the resonance at 700 Hz which limits the op-amp gain at that frequency. The increased experimental voltage is due to the positive feedback of the shunt. The reason for positive feedback can be explained by the fact that the NCR and total resistance for the four shunt configurations obtained above, which can be seen in Figure 5.32. At 700 Hz, the shunt has an NCR slightly less than one and a negative resistance value. The ability of this configuration of a negative capacitance circuit to obtain an NCR less than one was previously thought to be impossible. Yet, this combination leads to positive feedback, which increases the response of the beam, thereby increasing the voltage output greater than predicted. Figure 5.32 also shows the significant difference in attainable NCR and total resistance at the stability point by only changing the reference capacitance. Similarly, the total resistance only matches the desired value of 200 Ω for a small frequency bandwidth. Lastly, it is shown that the circuit can achieve NCR values less than one, which was previously thought to be unattainable given the traditional definition for stability prediction.

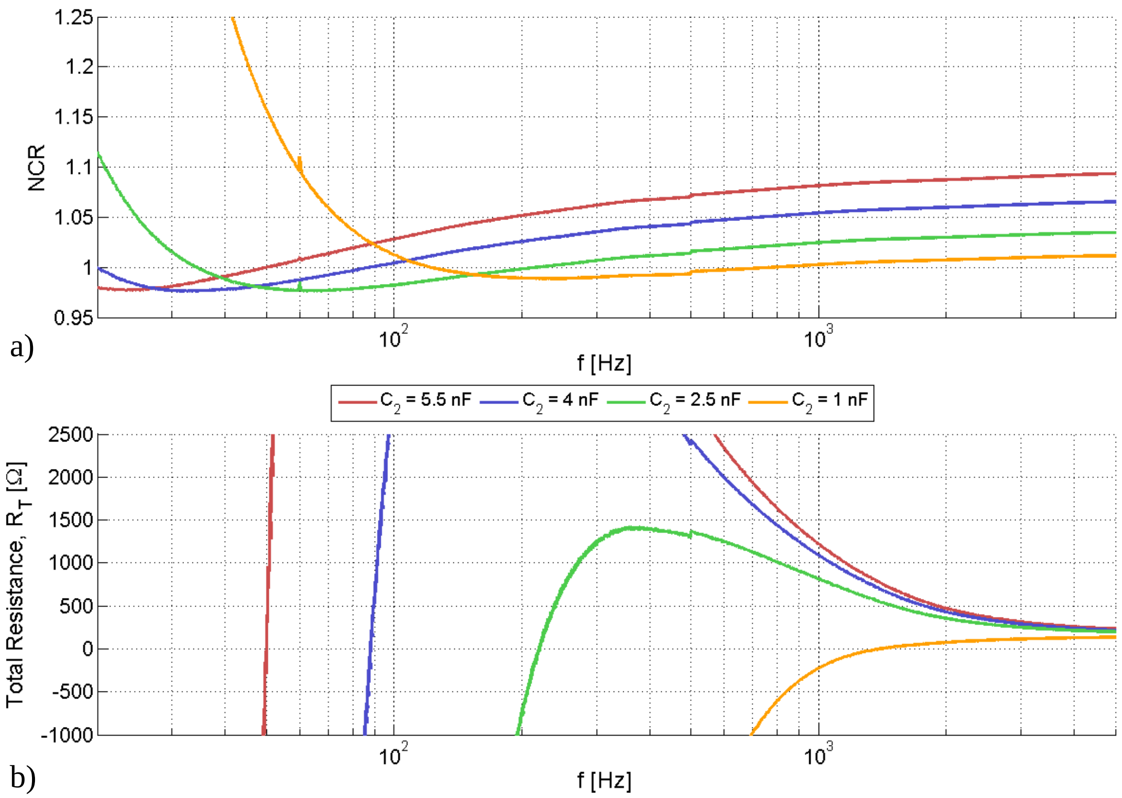

Figure 5.32 - a) NCR and b) total resistance for four shunt configurations attached to patch 6

To assess the effect of patch impedance on stability, α was found for the four values of reference capacitance when the shunt was connected to patch 2. The predicted output voltage again matches the experimental output voltage, as shown in Figure 5.33. Similarly, the predicted α matches the experimental values closely, where the maximum error is 0.41%. Again, there is significant improvement over the traditional estimate. For each reference capacitor, the circuit connected to patch two can achieve a greater α, but the difference reduces for smaller values of C_2. This is due to the frequency-dependent behavior of the patch impedance. Because the reference capacitor and resistor act as a high pass filter, as the reference resistor is reduced the circuit connected to each can reach similar values of NCR above 1000 Hz without going unstable at low frequency, which can be seen in Figure 5.34.

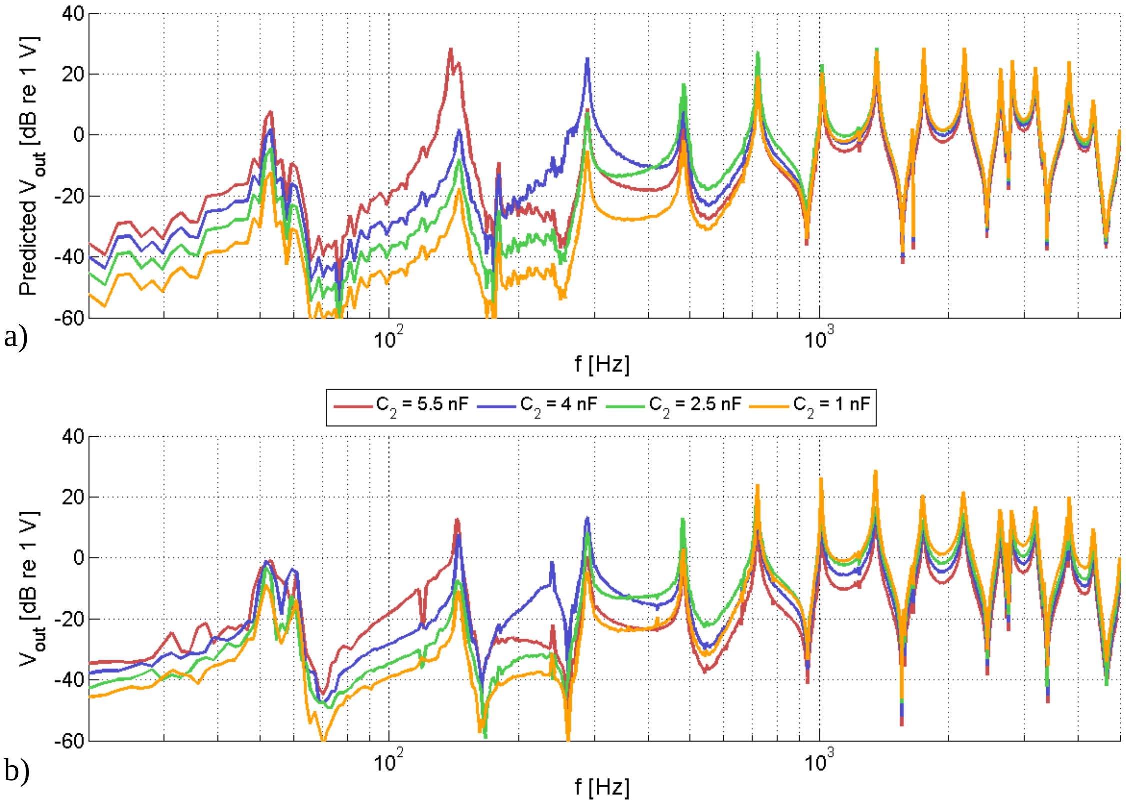

Figure 5.33 - Comparison of a) predicted op-amp output voltage and b) measured output voltage for patch 2

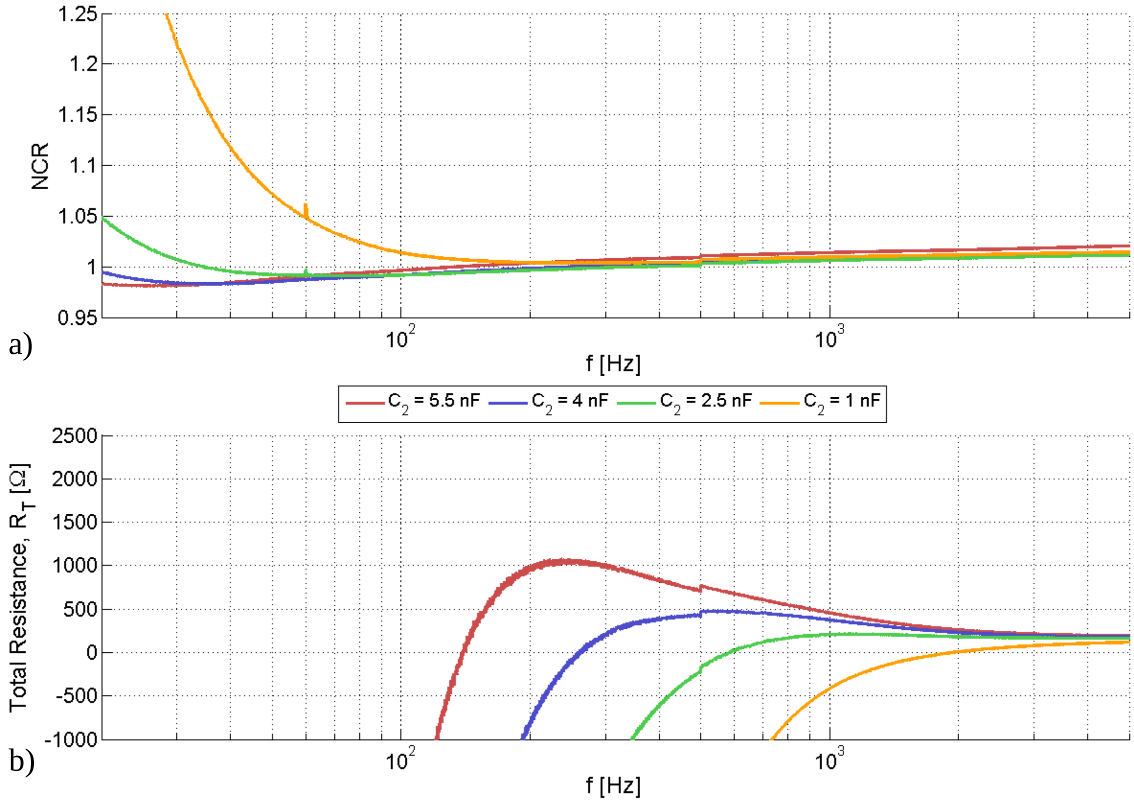

Figure 5.34 - a) NCR and b) total resistance four for shunt configurations attached to patch 2

The impedance of the shunt connected to patch 2 is shown in Figure 5.34 and is more consistent between reference capacitors than the shunt attached to patch 6. This can be attributed to the difference in patch capacitances at low frequency. The more constant frequency behavior of patch 2 allows the patch to reach similar values of NCR across a wider bandwidth. Figure 5.35 shows the ratio of NCR and total resistance of the shunt attached to patch 2 to shunt attached to patch 6. Similarly, Table 5.8 shows a direct comparison of the experimentally obtainable α for patch 6 divided by the obtainable α for patch 2. For seemingly identical patches, only for the 1.0 nF reference capacitor are the attainable α and NCR within 1% between the two cases for most frequencies, with patch 6 being slightly larger than patch 2. For larger capacitor values, the difference in NCR increases where the patch 6 NCR becomes larger than patch 2. The total resistance ratio is significantly different between the two cases. The total resistance is more consistent between C_2 and matches the desired value of 200 Ω over a wider frequency band than for the patch 6 case.

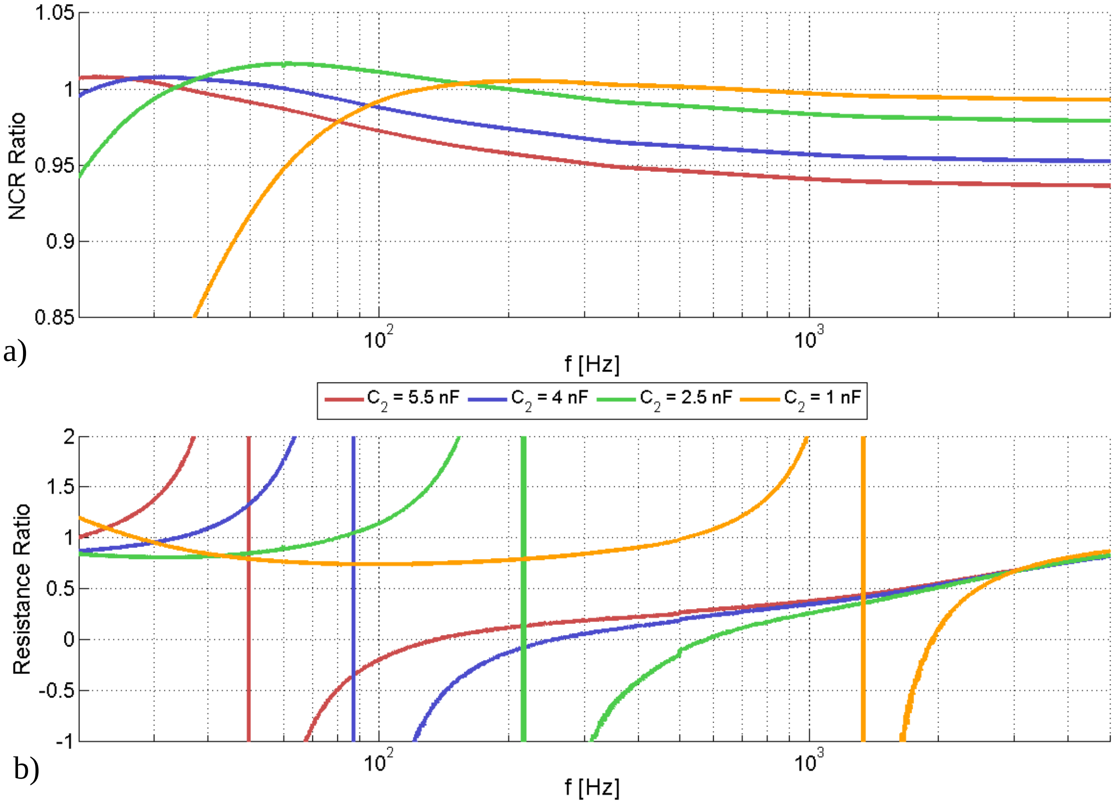

Figure 5.35 - Ratio of a) NCR and b) total resistance between patch 2 and patch 6

Table 5.8 - Ratio of experimental α, patch 6 case divided by patch 2 case

	C_2 = 5.5 nF	C_2 = 4.0 nF	C_2 = 2.5 nF	C_2 = 1.5 nF
α Ratio	0.981	0.981	0.987	0.999

From an inspection of Figure 5.34 and Figure 5.35, it is expected that patch 2 will exhibit more control than patch 6. Patch 2 has a much lower NCR for most frequencies for all reference capacitors. Also, the frequencies where patch 6 has a lower NCR than patch 2, the total resistance has more negative resistance, which will increases the response. This is confirmed in the tip response measurements of the beam when the shunt is attached to patch 2, Figure 5.36, and patch 6, Figure 5.37. Figure 5.36 shows a maximum suppression of 10 dB at the 2800 Hz resonance, which corresponds to the shunt configuration for the 4.0 nF reference capacitor. This configuration also had the lowest NCR across frequency for patch 2. In contrast, there is a maximum reduction of 3 dB at the 2800 Hz resonance when the shunt is connected to patch 6 for the 1.0 nF reference capacitor, as shown in Figure 5.37.

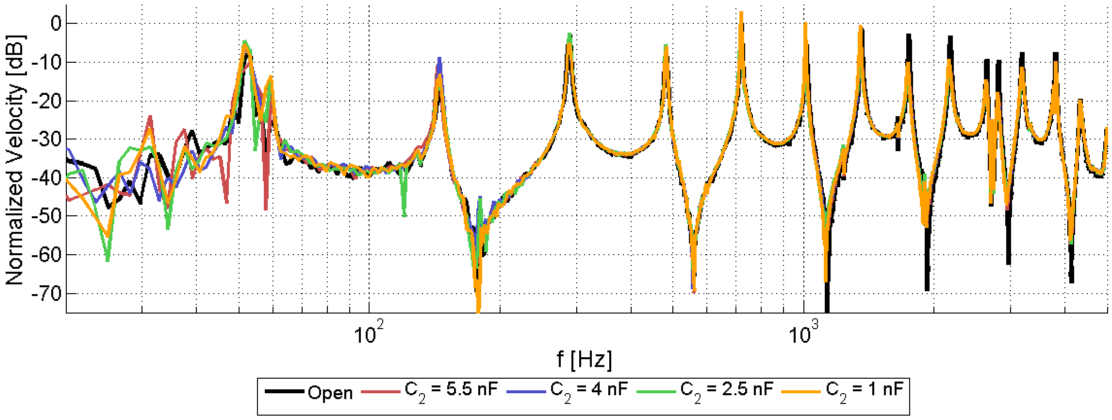

Figure 5.36 - Tip velocity response when shunt is attached to patch 2

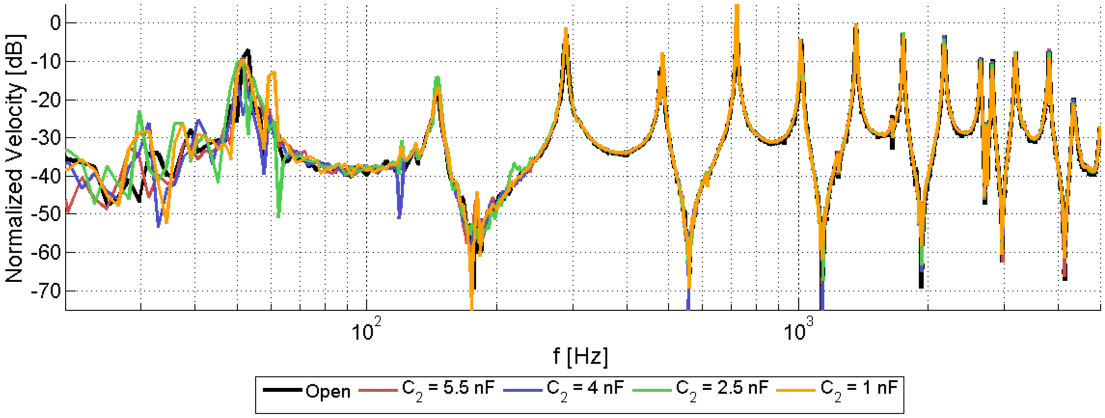

Figure 5.37 - Tip velocity response when the shunt is attached to patch 6

From this analysis, two general implementation guidelines can be made regarding proper selection in shunt components and patch impedance. First, frequencies where the shunt has negative resistance should be kept away from resonant frequencies of the vibration structure under control, generally below the first resonance. By doing this, the response of a vibrating structure will not be significantly increased due to positive feedback which further limits the attainable NCR. Secondly, a patch with a flat capacitance versus frequency and high resistance will impose more suppression. A low NCR will be consistent across frequency, which will increase the bandwidth of suppression. Also, the total resistance will obtain a desired value for a wider frequency range. In addition, by having a flat capacitance, the reference capacitance can be larger to reduce the frequency for which negative resistance occurs. This aids in implementation of the first guideline.

5.5 Summary

This chapter has discussed three aspects of the eletro-mechanical behavior of a structure-patch-shunt system. A modeling approach to determine the power output and efficiency of a negative capacitance shunt was presented. It was shown that a Multisim model of a piezoelectric patch connected to a negative capacitance shunt accurately predicts the power output of the op-amp. Model investigation showed that through selection of the passive elements of a negative capacitance inverter, the efficiency of the shunt can be increased. Also, the model predicts voltage output limits of the op-amp for the ratio of disturbance voltage to op-amp supply voltage.

The second section of the chapter outlined a tuning theory based on a single voltage measurement within the shunt to accurately predict vibration suppression of a vibrating system. The circuit analysis presented also allowed for comparison of maximum suppression to the power dissipated in the shunt. It was shown that maximum dissipated power does not correspond to maximum suppression for all frequencies.

Finally, a prediction method for determining the operating range of a negative capacitance shunt was developed. By measuring the impedance of the patch, the requirements of circuit stability and the op-amp voltage output limitations were accurately modeled and predicted. The prediction method was confirmed on two piezoelectric patches with different impedance frequency behavior. From the analysis of stable circuit values, the prediction of the differences in suppression was made and confirmed experimentally. Lastly, general recommendations were given, based on the conclusions from the stability analysis, on how shunt component values should be determined to increase control.

CHAPTER 6

WAVE PROPAGATION EFFECTS

6.1 Introduction

This chapter numerically and experimentally illustrates the attenuation effect of negative capacitance shunts combined with periodic piezoelectric patch arrays. The first section discusses the wave propagation attenuation for a 1D waveguide. A numerical investigation is performed and compared to experimental results. The next section presents a similar analysis but for a 2D array when negative capacitance shunts are combined with resonant shunts. Lastly, a summary of the conclusions of the chapter is presented.

6.2 One Dimensional Wave Propagation

The physical effects that a negative capacitance shunted periodic array of piezoelectric patches has on a vibrating beam will be explored by analyzing numerical predictions of wave attenuation through the use of finite element analysis, an array length study, and the velocity response of different sections of the beam. These investigations will explore how the periodic array enhances the control ability of the negative capacitance shunt. Through the modification of the "stop-bands" of the periodic array, the negative capacitance shunt is expected to have more control over a wider frequency range as compared to control in the absence of the negative capacitance shunt. The wave attenuation calculations will give perspective to the frequency dependence of the shunt parameters and these parameters will be used as a starting point for the experimental investigations. The array length study will give insight into how much control effort is achieved with increasing the number of patches. It was remarked earlier that the action of the negative capacitance shunt applied to the boundary of a cantilever beam causes the beam to act as if it is infinite. Therefore, by comparing the velocity response of beam over the region of the beam between the forcing and the array, the array area, and between the array and clamp this effect can be further investigated. The results of these studies on a periodic beam will give greater insight into the physical effects of the negative capacitance shunted piezoelectric periodic array and how a modal system may be controlled by periodic arrays.

6.2.1 Finite element analysis

A numerical model of a coupled mechanical-piezoelectric system is developed here to obtain predictions of vibration response and to be validated with experimental results. The system of interest is a thin cantilever beam shown in Figure 6.1. There are 12 equally spaced piezoelectric patch pairs located at the center on the beam, with each patch pair connected to its own individual shunt circuit. These 12 patches constitute the periodic array. The upstream and downstream labels in Figure 6.1 are such because a point force is located at the "upstream" tip. The patch array section of beam can be studied by employing a dispersion analysis of single unit cell of the periodic array, Figure 6.2. The dispersion analysis computes which frequencies are attenuated when a wave is passed through the array. A finite element model for both the full system and the unit cell is developed utilizing the method in Section 3.3. The result of interest for the finite element calculations for the beam is the spatial average transverse velocity. The unit cell finite element model obtains the complex wave number that represents the attenuation of propagating waves.

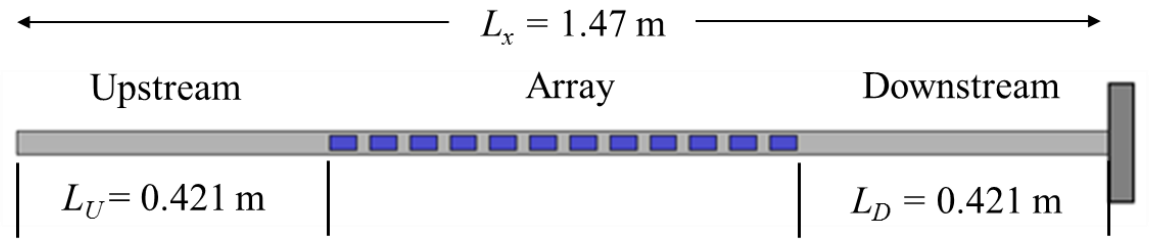

Figure 6.1 - Cantilever beam with a bonded piezoelectric array, centered on beam face

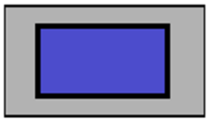

Figure 6.2 - Single unit cell of periodic array

6.2.2 Experimental Setup

A long cantilever beam with a patch array and necessary data acquisition equipment was assembled to investigate the effect of the negative capacitance shunts. The long thin aluminum beam which is clamped on one end has 12 piezoelectric patch pairs bonded symmetrically on both sides, for a total of 24 patches. The construction of the beam consisted of gluing a thin kapton film to both faces of the beam to electrically isolate the bottom surfaces of the piezoelectric patches which are bonded to the kapton. The bottom face of the surface of the piezoelectric was electroded by a thin copper tape that was attached to the piezoelectric by conductive epoxy. The material properties and physical dimensions of the beam and patches are shown in Table 6.1. Each pair of patches is electrically connected in parallel. The individual pairs are connected to individual shunt circuits which creates 12 single input, single output (SISO) control systems. The beam is also separated into three sections, just as Figure 6.1, labeled as: upstream, array, and downstream. These sections will be analyzed separately to investigate energy localization.

Table 6.1 - Beam and patch physical parameters

Beam	Young's modulus	$E_b = 73$ GPa
	Density	$\rho_b = 2700$ kg/m^3
	Length	$L =$ 1.47 m
	Width	$w =$ 18.2 mm
	Thickness	$t =$ 3.3 mm
Piezoelectric	Young's modulus, shorted	$E_p = 63$ GPa
	Density	$\rho_p = 7800$ kg/m^3
	Coupling coefficient	$k_{31} = 0.35$
	Thickness	$t =$ 0.8 mm
	Capacitance	$C_p =$ 58.5 nF

The response of the cantilever beam is measured by the use of a laser Doppler vibrometer. The vibrometer consists of a computer module, function generator, and scanning laser head. The computer controls the necessary settings for data acquisition and links with the function generator to create a signal output. The output is sent to an electromechanical shaker that forces the beam at the tip. The velocity of beam is measured by the scanning laser head at 125 equally spaced locations along the length of the beam. The data from these points are used to compute the spatial average velocity in the regions of interest, either the full length or the three sections of the beam.

The spatial average velocity frequency response function (FRF) comparison between a base line (open circuit) case and the control shunt connected expresses an overall reduction in vibration of the beam. The squared spatial average velocity is defined as

$$\left\langle \left| u\left(f \right) \right|^2 \right\rangle = \frac{1}{L_x} \int_0^{L_x} \frac{u^2\left(f, x \right)}{F\left(f \right)} dx \tag{6.1}$$

where *f* is the frequency and *u* is the velocity at a point *x* along the length of the beam. The spatial average velocity response of the finite element model will be validated by the experimentally obtained measurements.

6.2.3 Results and analysis

To begin, the results of the dispersion theorem analysis will be presented to express the frequency impact of the control shunt on a unit cell. For maximum control, the negative capacitance of the shunt is set to a stable value as close to the magnitude of the patch capacitance. The negative capacitance value is 66.7 nF, which is used for both numerical calculations and experiments. This value is the minimum negative capacitance magnitude that can be obtained experimentally. The frequency dependence of the shunt will be explored by changing the resistance in series with the negative capacitance, R_s in Figure 4.11. Figure 6.3 shows the propagation constant, calculated using the method outlined in Section 3.3.2, for three values of resistance and the open circuit configuration, which is considered the uncontrolled case. The response of the unit cell for the open circuit case displays a stop band at 2600 Hz which is inherent from the impedance mismatch introduced by the bonded patches. For low resistance values, the inherent stop band of the patch geometry at 2600 Hz is amplified when the circuit is applied. Yet, with larger resistance the increased damping in the shunt minimizes the periodic effect but does increase the control effectiveness at lower frequencies. For the 100 Ω resistor, the propagation constant reaches the same increased stop band level of lower resistance and is greater for both higher and lower frequencies. From this figure, the propagation constant predicts for small resistances the control shunt will have a frequency localized impact. The shunt should have the most effect at lower frequencies with higher resistance.

Beginning with a finite element simulation, Figure 6.4, the negative capacitance shunt significantly reduces the velocity of the beam from 600 to 5000 Hz. The maximum numerically predicted reduction is 11 dB at the 2300 Hz resonance. The resonance at 2500 Hz cannot be controlled by the shunts, but both resonances above and below this uncontrolled frequency exhibit the maximum attenuation. This behavior agrees with the dispersion analysis results where the effectiveness dips at 2500 Hz but has a maximum at the frequencies immediately lower. As was also predicted by the interpretation of Figure 6.3, the frequency dependent behavior of the different series resistors is exhibited in the spatial average velocity frequency response of the finite element model. The 100 Ω resistor creates the largest attenuation for frequencies above the uncontrolled mode located at 2600 Hz. In addition, the large resistance configuration produces the largest control at low frequencies. The numerical spatial average velocity response is verified experimentally as shown in Figure 6.5. Both the propagation constant predictions and the numerical results are confirmed by the experimental velocity response of the beam. Figure 6.5 shows the spatial average velocity of the beam for the same three values of resistance. The maximum suppression is found to be 12 dB at 2100 Hz for the 100 Ω resistor. The resonance at 2600 Hz is also not controlled. The frequency nature of the three shunt configurations can be seen as well, with the 55 Ω resistor having a strong localized effect around 2400 Hz. A minimum of 5 dB velocity reduction is obtained at all modal peaks from 600 to 5000 Hz with the 100 Ω resistor. It should also be noted that these attenuation values represent a global measure for the reduction in vibration amplitude because $\langle |u| \rangle$ is a spatial average over the entire length.

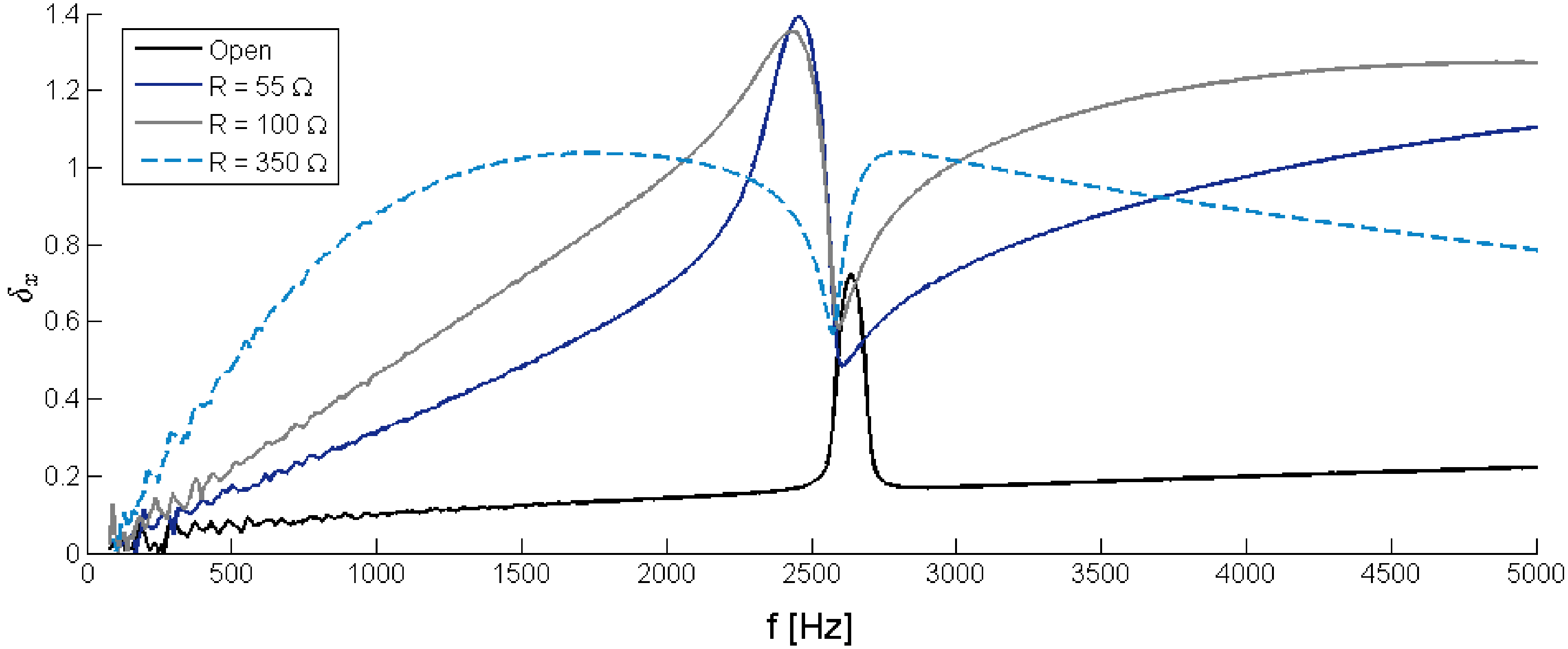

Figure 6.3 - Propagation constant for negative capacitance shunts

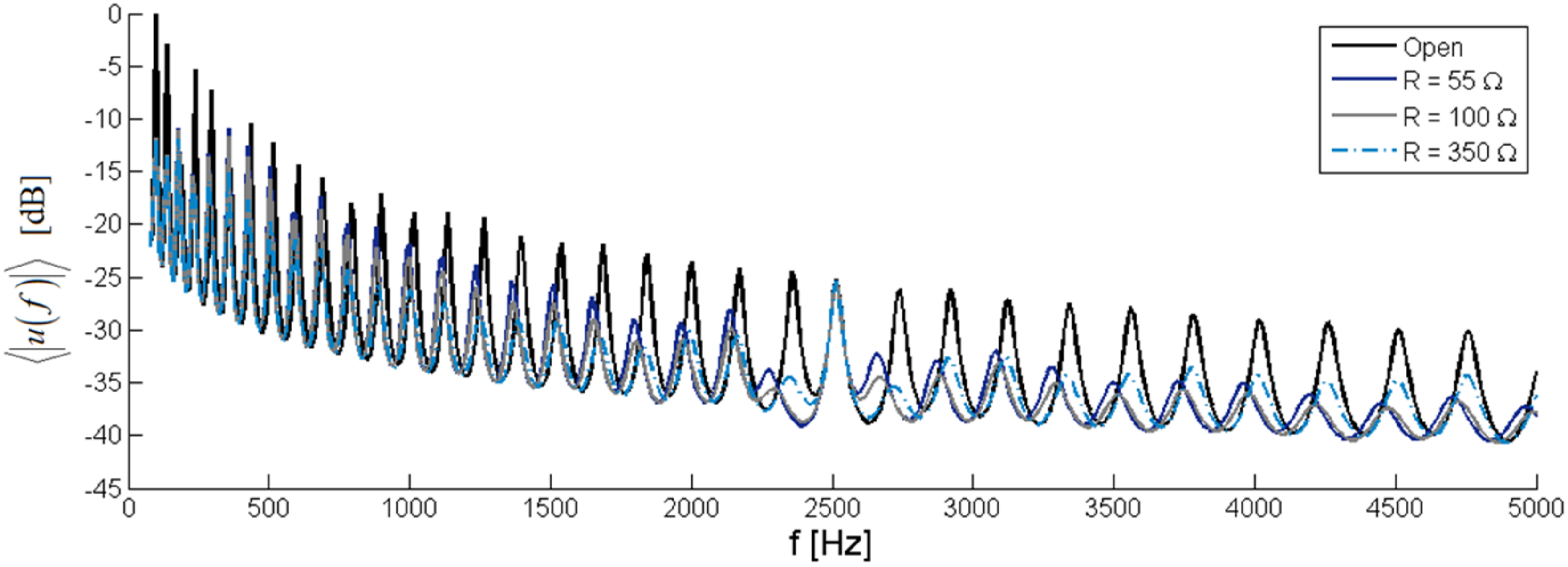

Figure 6.4 - FEM predicted spatial average velocity FRF

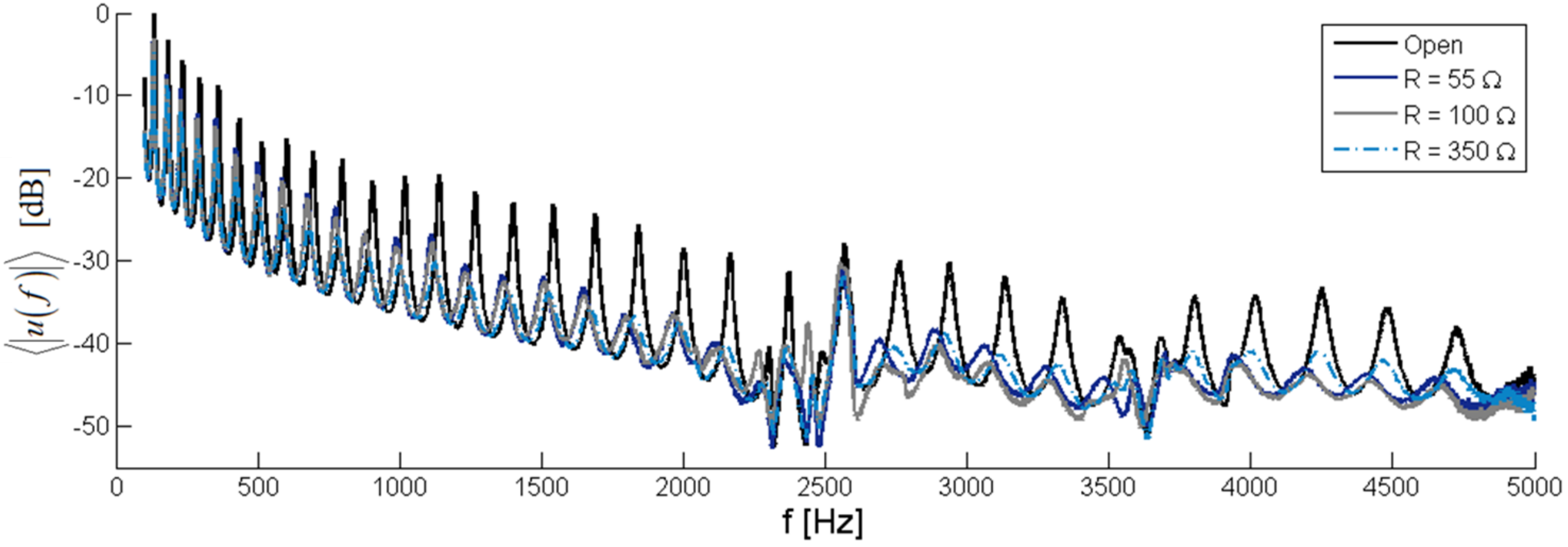

Figure 6.5 - Experimental spatial average velocity FRF

The three sections of the beam behave differently when the control shunt is applied. Figure 6.6 and Figure 6.7 show the spatial average velocity response of the upstream and downstream sections of the beam. The negative capacitance control causes the velocity minima to increase in the upstream section of the beam as seen in Figure 6.6. In contrast, Figure 6.7 shows the average velocity decreases at the anti-resonances of the downstream section. These changes are caused by the vibration localization of the shunt array. This can be quantified by summing the spatial average kinetic energy of each section over all frequencies. The frequency integrated kinetic energy difference between the open and control cases is defined as

$$\Delta T = 10\log_{10}\left[\int_{f}^{f_{\max}} \frac{T_c}{T_{uc}} df\right] \tag{6.2}$$

where T_c is the controlled kinetic energy and T_{uc} is the uncontrolled kinetic energy. The kinetic energy change between the open circuit and control cases for the upstream and downstream sections of the beam are shown in Table 6.2. This table displays the difference between uncontrolled and controlled kinetic energy for three lower integration limits. As the integration is confined to higher frequencies, there is a greater difference between the controlled and uncontrolled cases. This shows that the shunt reduces the energy of the vibration as the waves pass through the array. Therefore for higher frequencies, the circuit has a greater vibration localization effect. This trend is expressed in Figure 6.8, also. The localization is also expected from the analysis of the frequency dependence of the propagation constant, as shown in Figure 6.3, which expresses the attenuation of the propagating wave through the array. The two curves show the kinetic energy difference for the upstream and downstream sections of the beam. The separation between the two curves increases as the frequency of the lower integration limit increases. In summary, the spatial average velocity of the whole beam decreased when the control is added, but the array has a greater effect in reducing the energy in the area downstream of the array. The effect of the array can also be considered an anechoic boundary, because the vibration energy is dissipated and not reflected back upstream.

Table 6.2 - Frequency integrated total kinetic energy difference

Range	Upstream	Downstrem
0.1 - 5 kHz	-4.2 dB	-5.7 dB
0.5 - 5 kHz	-6.6 dB	-10.4 dB
1.5 - 5 kHz	-6.2 dB	-13.7 dB

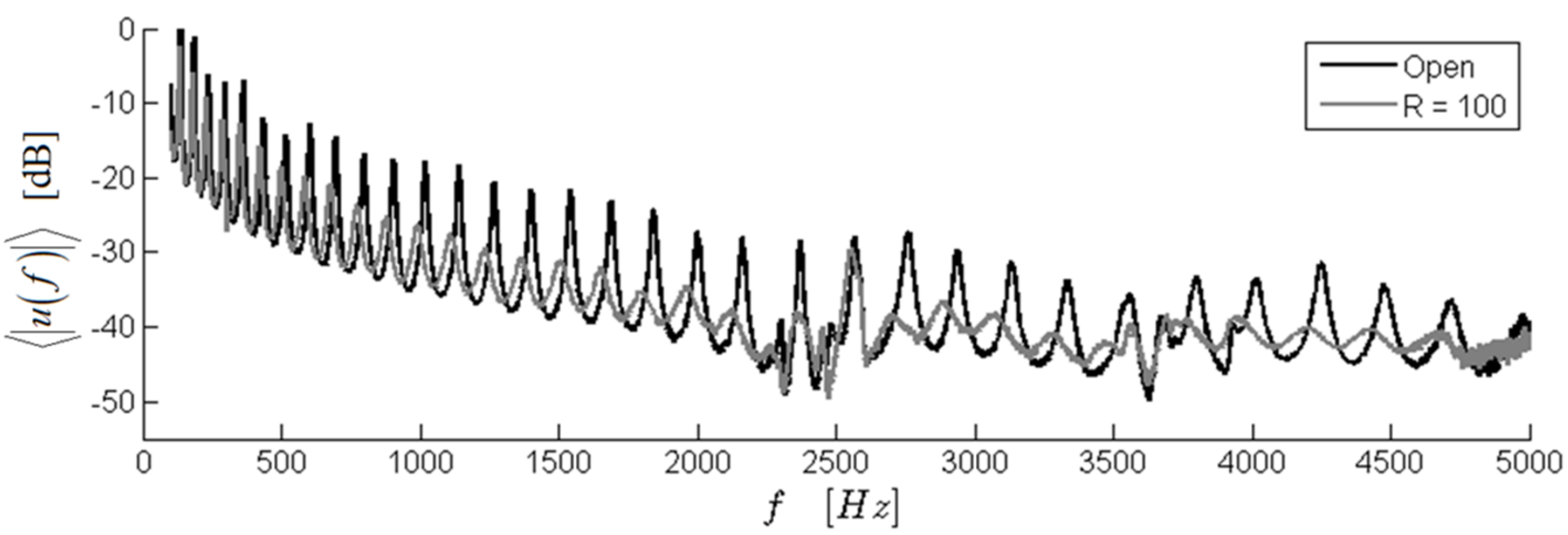

Figure 6.6 - Spatial average velocity FRF for the upstream section

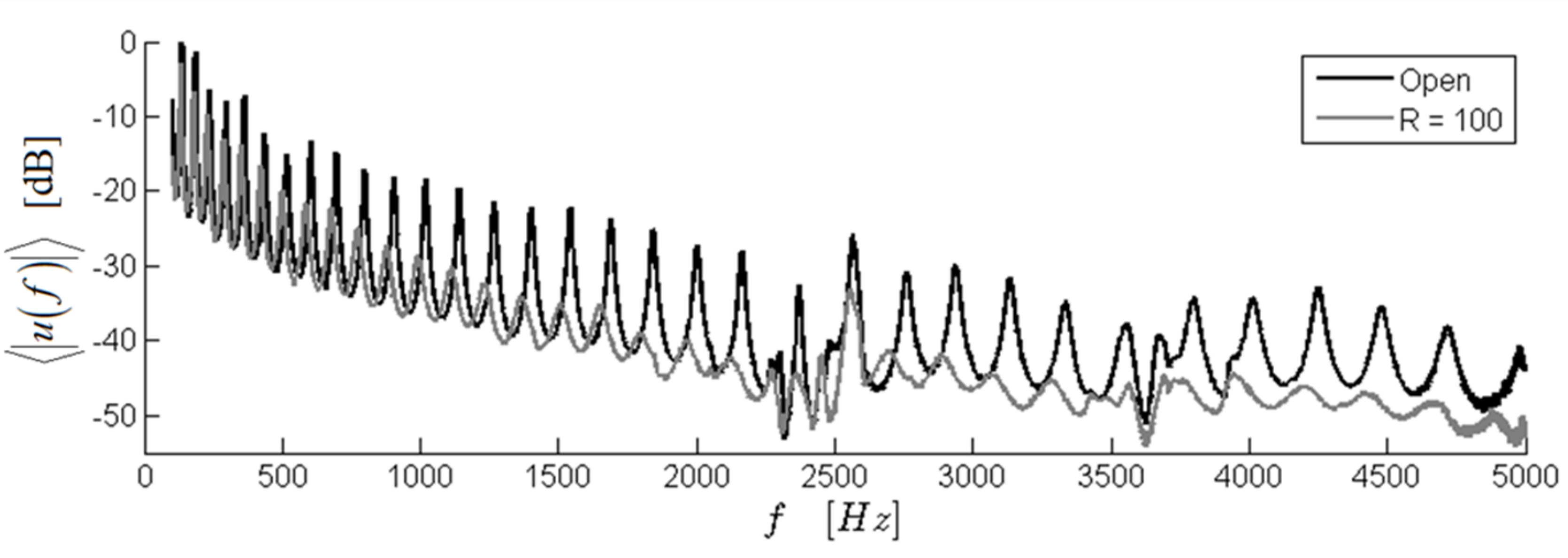

Figure 6.7 - Spatial average velocity FRF for the downstream section

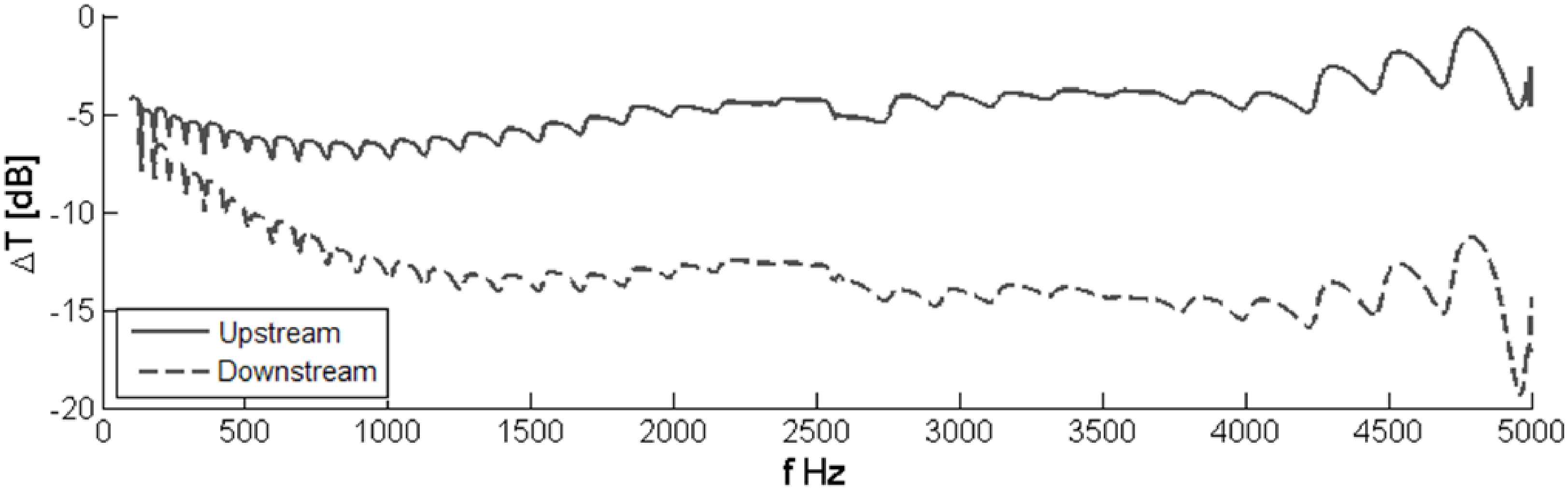

Figure 6.8 - Frequency integrated kinetic energy difference

The number of patches with the control connected impacts the reduction in velocity of the resonant peaks. Figure 6.9 shows the numerical prediction of attenuation for the 15th and 16th resonant peaks of the beam relative to the open circuit case as more patches are added to the array length. The 15th and 16th resonances are located at 1400 and 1550 Hz. A pair of sequential resonances was needed to analyze the behavior of the control when increasing the array length, and these two were chosen arbitrarily because they exhibit average modal attenuation. The attenuation is expressed in a dB value with the uncontrolled amplitude the reference. The overall trend is increasing reduction with increasing array length, yet the addition of certain patches has more impact on control than others. Also, the modes are impacted differently when more patches are applied. The attenuation increases by increasing the number of patches in the array; but not smoothly increasing, rather, exhibiting ramps and plateaus. The behavior is attributed to the modal response of the beam, which affects the locations where a patch can exert control. The ramps are present when the addition of a single patch causes significantly more control to the overall vibration. In contrast, a plateau occurs when adding another patch to the array length does not cause any appreciable increase in attenuation. The reduction in modal amplitude therefore depends on the location of the additional patch in the array with respect to the mode shape. Therefore, the propagation constant cannot be considered an exact prediction between reduction in vibration of a modal system at every frequency.

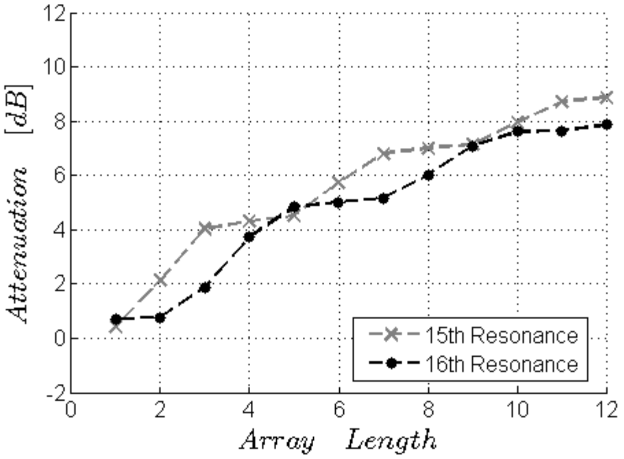

Figure 6.9 - Numerical vibration reduction versus array length, # of patches

The experimental data shows similar ramps and plateaus in attenuation with increased array length, Figure 6.10. The corresponding resonances show after 8 patches there is only incremental increases in attenuation. Therefore, by adding more patches to create a longer array will only yield diminishing returns in suppression of vibration.

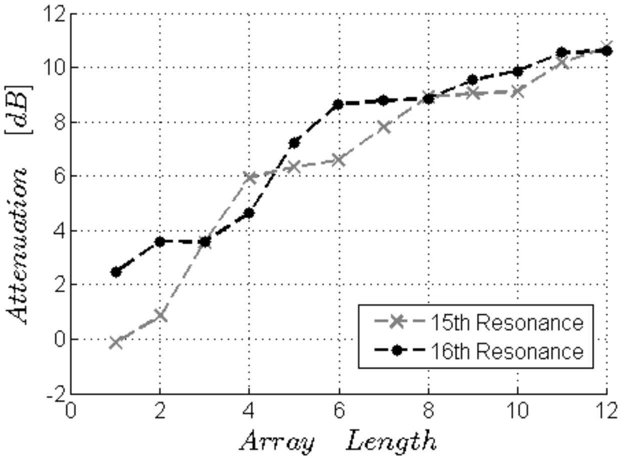

Figure 6.10 - Experimental velocity reduction versus array length, # of patches

6.3 Two Dimensional Wave Propagation

Apart from using just negative capacitance shunts for vibration suppression, control of a 2-D plate structure can be achieved by a hybrid shunt configuration. The term hybrid refers to the simultaneous use, on the same host structure, of both resonant RL and negative capacitance electrical shunts. The use of hybrid shunts has been investigated by Tang and Wang [35], Tsai and Wang [32], and by Zhao [93] where the use of hybrid active-passive mechanisms were applied to the same patch. The present approach is different in the sense that an individual patch is shunted with either an RL or a negative capacitance circuit. This significantly simplifies the design of the two networks that can now be considered separately. The present implementation also exploits the unique properties of periodic systems to generate broadband frequency regions of wave attenuation. The simultaneous use of resonant and negative capacitance shunts is studied here to combine the advantages of the two concepts and thus to provide a control mechanism specifically designed to suppress vibrations in the low-mid frequency range, which typically characterize the critical spectrum of structure-borne noise in rotorcraft cabins [94]. Numerical analyses are conducted employing a finite element model specifically developed to investigate the dynamic behavior of thin plates with surface-bonded shunted piezoelectric patches. Specifically the FE model is used to calculate the frequency response of finite assemblies and to predict the dispersion properties of periodic systems through the unit cell analysis approach typically employed to characterize the wave propagation properties of periodic media. Experimental tests are also performed on a periodic thin plate both to validate the predictions of the unit cell analysis and to verify the effectiveness of the proposed control strategy.

6.3.1 Numerical Configuration and Results

Finite element simulations are exploited to predict the capability of periodic hybrid shunts to reduce the vibration field of a cantilever plate. The host structure is a rectangular aluminum plate ($E = 71.0$ GPa, $\nu = 0.33$) with sides length of 406×203 mm and thickness of 1.0 mm. The plate dimensions are chosen to realize a periodic layout of 4×4 piezoelectric patches, as shown in Figure 6.11, which constitutes a reasonably simple configuration that can be further studied experimentally. The technical specifications of ACX QP25N patches, which are used in the experimental validation, are summarized in Table 6.3. These piezoelectric properties are used in the numerical analysis. The vibration attenuation properties of the proposed configuration are studied both in terms of the attenuation constants, evaluated on the unit cell of the periodic plate, and through analysis of the frequency response of the finite assembly. The attenuation constant is calculated along the main plate direction (x direction as defined in Figure 6.11) which is of interest due to the geometry and forcing of this test case. For the frequency response, the plate is excited with a point force, and the response is evaluated in terms of out-of-plane displacement at one node of the model as shown in Figure 6.11. The hybrid configuration is implemented by an equal number of RL and negative capacitance circuits, each connected to a single piezoelectric patch. To verify the robustness of this control strategy, two different shunt distribution arrangements, labeled “A” and “B”, are tested as illustrated in Figure 6.12 along with the corresponding unit cell configurations. In Figure 6.12, the dark solid patches indicate patches connected to negative capacitance circuits, while the shaded (blue) patches are connected to resonant (RL) networks. For convenience, the negative capacitance shunts are labeled NIC in all the figure captions.

Table 6.3 - Mide ACX QP25N specifications

Device Size	50.8 x 25.4 x 0.508 mm
Weight	3.68 g
Number of Active Elements	2
Capacitance	200 nF
PZT Wafer Size	45.97 x 20.57 x 0.127 mm
Operating Range	± 100 V

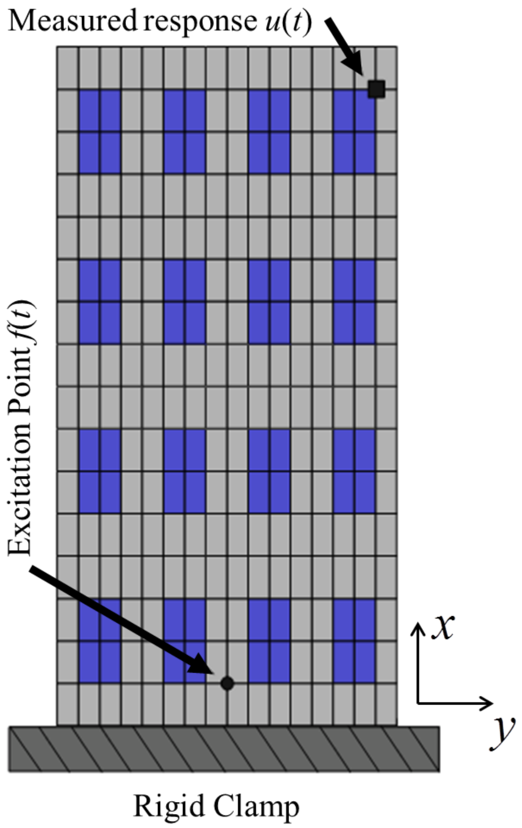

Figure 6.11 - Cantilever aluminum plate with 4×4 array of surface-bonded piezo

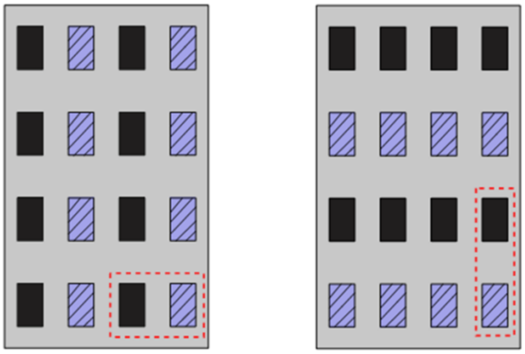

(a) Configuration A

(b) Configuration B

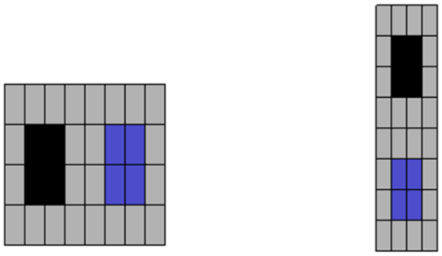

(c) Unit cell A

(d) Unit cell B

Figure 6.12 - Configurations A (a) and B (b) chosen to realize a finite periodic assembly, and corresponding unit cells (c) and (d)

The computed attenuation constants are shown in Figure 6.13a and Figure 6.14a for different configurations of the shunted network. The open circuit case represents a baseline reference in which the piezoelectric patches are not connected to the corresponding shunt circuits and thus no control authority is exercised on the system. A first attenuation range is shown to be centered at about 220 Hz, and remains approximately the same for all circuit configurations. This can be attributed to the impedance mismatch generated by the added mass and stiffness of the piezoelectric patches and cannot be controlled through the shunting parameters.

Figure 6.13a and Figure 6.14a show that when only the negative capacitance circuits are connected to the electrodes of the piezoelectric patches does the attenuation constant assumes positive values almost everywhere in the considered frequency range. From a different perspective, frequency response functions (FRFs), shown in Figure

6.13b and Figure 6.14b, illustrate that significant vibration reduction is achieved in the corresponding frequency range. These figures also show that between 400 and 600 Hz the significant vibration level of the structure is only partially attenuated by negative capacitance shunts. Due to their resonant behavior, RL shunts are tuned to this region of opportunity to improve the control effect of the negative capacitance networks. Figure 6.13 and Figure 6.14 in fact show that when tuned to 500 Hz, the RL shunts alone generate a significant region of wave attenuation centered at the tuning frequency that is responsible for a strong reduction of vibration amplitudes as shown in the corresponding FRF plots. When the two shunting strategies are simultaneously used it is possible to observe a summing interaction that retains the broadband vibration reduction effect typical of the negative capacitance circuits and also the resonant behavior at 500 Hz due to the tuning of the RL networks as illustrated in Figure 6.13b and Figure 6.14b respectively. The similarity of behaviors observed for both configurations A and B testifies to the robustness of this control strategy.

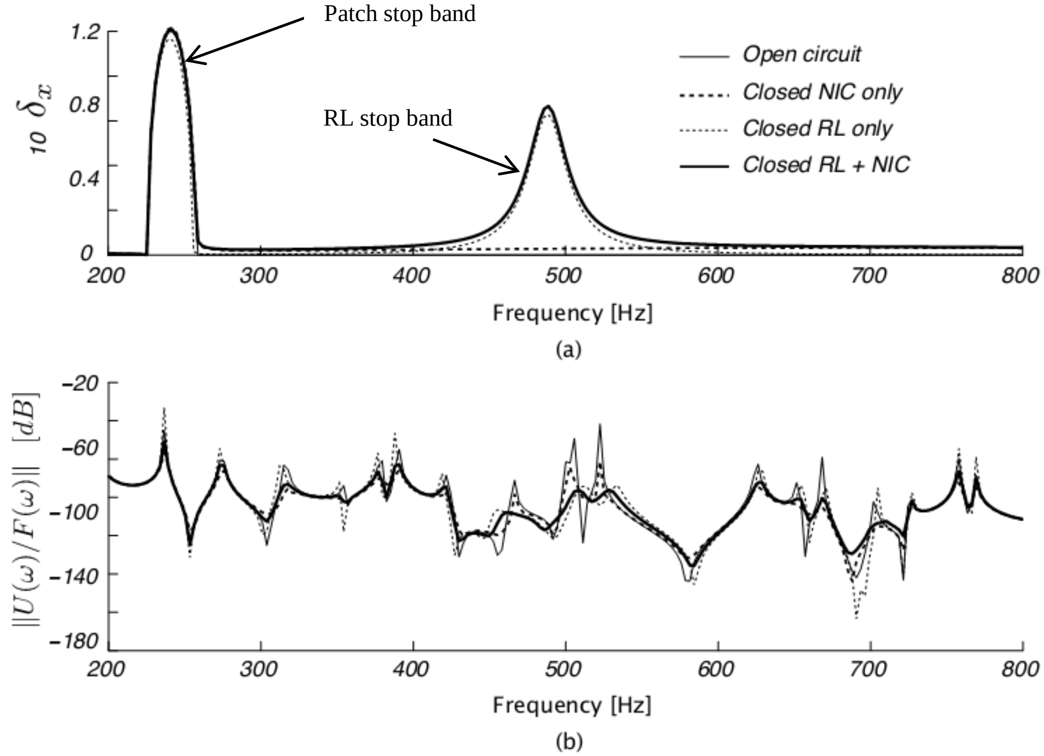

Figure 6.13 - Attenuation constant (a) and frequency response (b) of the system in configuration A

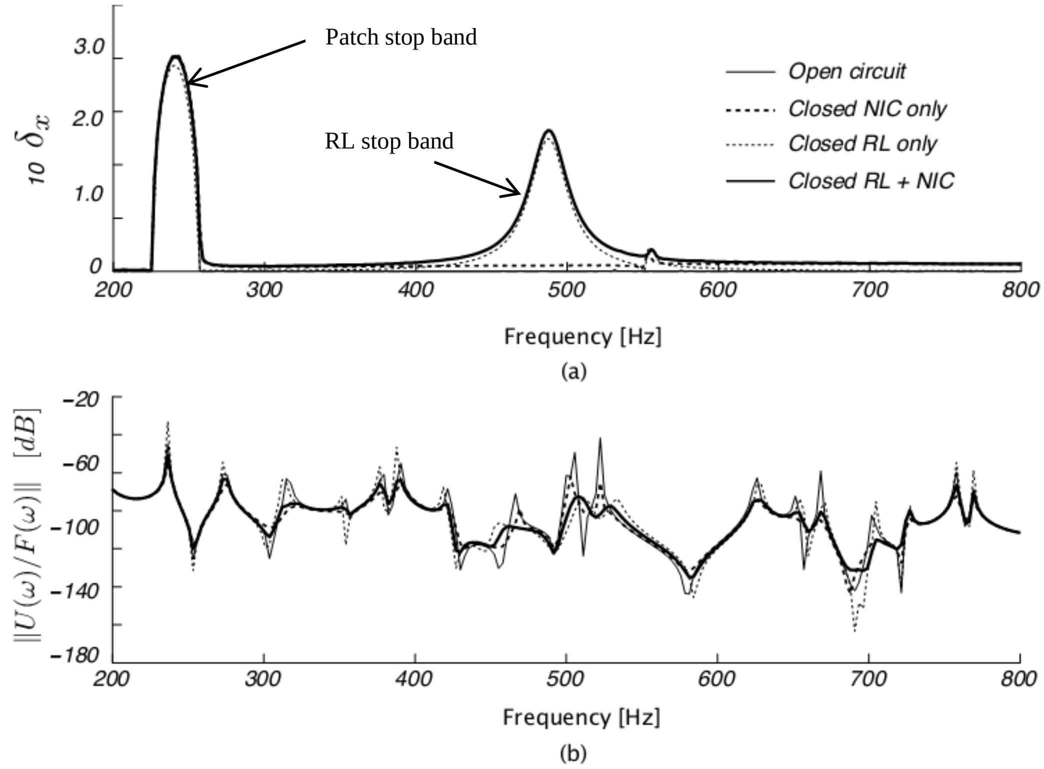

Figure 6.14 - Attenuation constant (a) and frequency response (b) of the system in configuration B

6.3.2 Experimental Setup

Experiments were conducted to verify the effectiveness of the hybrid configuration in reducing both low- and mid-frequency modes in the range between 0 and 1400 Hz. Dynamic tests were performed on an aluminum cantilever plate with surface bonded PZT patches. The host structure and the piezoelectric patches were the same used for numerical simulations and the experimental setup is shown in Figure 6.15. The applied force was provided through an electrodynamic shaker LDS V201/3, and the response was measured through a Polytec PSV-400 scanning laser vibrometer. All the actuators were connected to an independent circuit using cables CB-011 provided by the patch manufacturer. In order to limit the effects of these thick and stiff cables on the dynamics of the tested structure, they were suspended with soft rubber bands.

Both the resonant and negative capacitance shunts were created using active circuit elements. The negative capacitance shunt was implemented using the "Type 1" configuration and a series resistor, as outlined in Section 4.3. Using a trial and error approach, a series resistor of 100 Ω was determined to yield the greatest suppression of vibration over the frequency range of interest. For resonant shunts which target low- to mid-frequency vibrations, the required inductor is typically on the order of tens of Henries which would be impractical to implement by passive means on lightweight structures due to the sheer size and weight of such large inductors. Therefore, there is a need for a synthetic inductor, which employs two op-amps and passive circuit elements to create tunable inductance. Refer to the work of Casadei *et al.* for a presentation and analysis of the synthetic inductors used for these experiments [95]. The value of inductance is selected in order to tune the RL circuit at a specific frequency f_{tun} according to

$$L = \frac{1}{\omega_{tun}^2 C_p} \tag{6.3}$$

where $\omega_{tun} = 2\pi f_{tun}$ and C_p is the capacitance of the piezoelectric patch. A 33 Ω resistor was chosen for the resonant shunt, which corresponded to the compromise between attenuation magnitude and bandwidth.

Figure 6.15 - Finite periodic assembly used to experimentally validate the effectiveness of hybrid shunting

6.3.3 Results and Analysis

Frequency response functions corresponding to different shunting strategies are presented and compared to experimentally verify the effectiveness of hybrid shunts. Four different shunting configurations are considered to verify the vibration control performance of configurations A and B. The change in attenuation behavior at different frequencies is tested by measuring the systems' response when the RL circuit is tuned at 700 Hz (Figure 6.16 and Figure 6.17) and 1150 Hz (Figure 6.18 and Figure 6.19). Four different circuit configurations are illustrated. A first run is made considering only the effect of the negative capacitance circuits while the other piezoelectric patches are shorted (i.e. $Z_S = 0$). Then, the complementary configuration is measured where only the RL circuits are connected and tuned at the desired frequency. The third measurement is made to consider the simultaneous effect of the two shunting strategies. Finally, the open circuit response (i.e $Z_S \rightarrow \infty$) is also illustrated as a common reference baseline to evaluate the performances of the different shunting strategies. Frequency response functions are illustrated in Figure 6.16 to Figure 6.19 along with plots of the unit cell attenuation constant to verify the accuracy of this approach to predict the actual response of the system. These measurements are repeated for the two periodic configurations of Figure 6.12 in order to experimentally demonstrate the robustness of the proposed control approach. Two different tuning frequencies are selected for the RL circuit tunings. Of particular interest is the 0-1400 Hz range, which is relevant for the reduction of structure-borne noise in rotorcraft cabins [94]. The first tuning frequency is arbitrary selected at 700 Hz, while the second tuning frequency is chosen at 1150 Hz to compensate for the lack of effectiveness of the negative capacitance shunts around this higher frequency.

Figure 6.16a through Figure 6.19a show the effects of different shunting configurations on the attenuation constant of the system. These results demonstrate the broadband damping effect introduced by the negative capacitance shunts and the possibility to introduce additional attenuation bands through proper tuning of the resonant RL shunts. The same figures show that when the two control strategies are simultaneously combined on the same structure, the hybrid solution allows for the benefits of both the negative capacitance and RL effects. These trends are corroborated by the measured averaged spatial response of the plate, defined as the spatial average value of the velocity responses measured by the laser vibrometer over the plate surface. In particular, Figure 6.16b through Figure 6.19b show, for both configurations A and B, that amplitude attenuation up to 8 dB is achieved on the tuning frequency of 700 Hz and 4 dB at the second tuning frequency of 1150 Hz by RL shunts, but also that their effectiveness vanishes at frequencies away from the tuning, where instead negative capacitance shunts perform better. When the two shunting strategies are used simultaneously the frequency response of the plate follow the trend imposed by the negative capacitance networks in the lower frequency range, while at higher frequencies the dynamics is dominated by the resonant behavior of RL shunts. It is particularly interesting to observe that RL circuits can be tuned to frequencies where the negative capacitance shunt does not have desired performance, allowing for increased attenuation as demonstrated by Figure 6.18 and Figure 6.19.

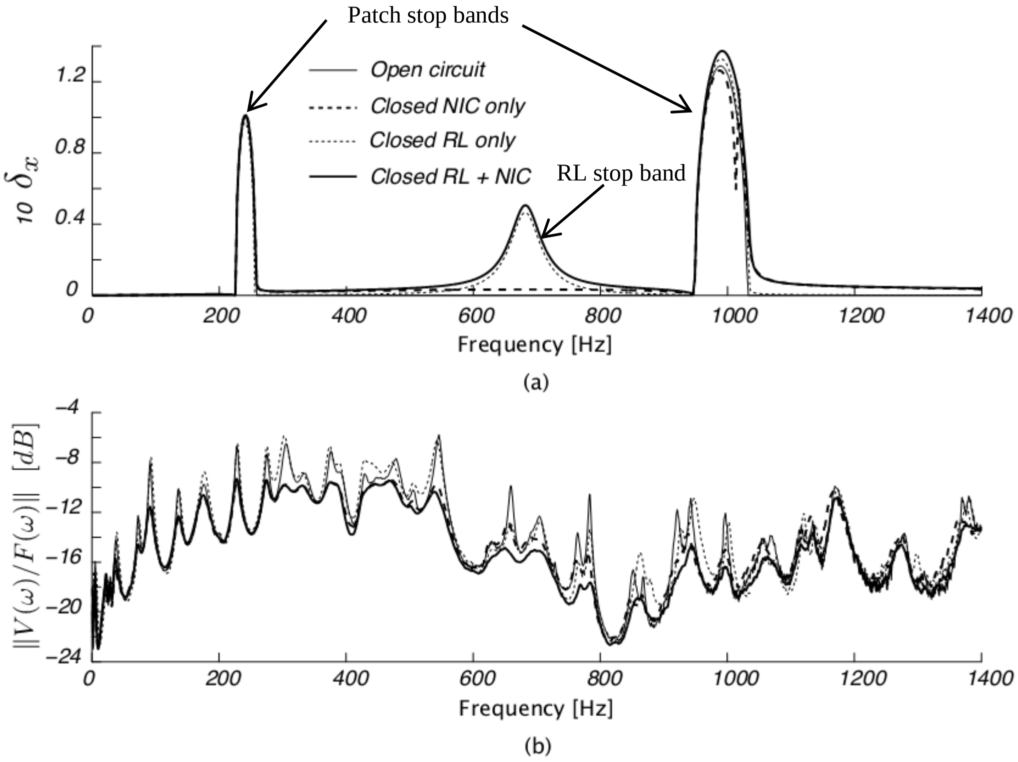

Figure 6.16 - Attenuation constant (a) and measured frequency response (b) of the system in configuration A, RL tuned to 700 Hz

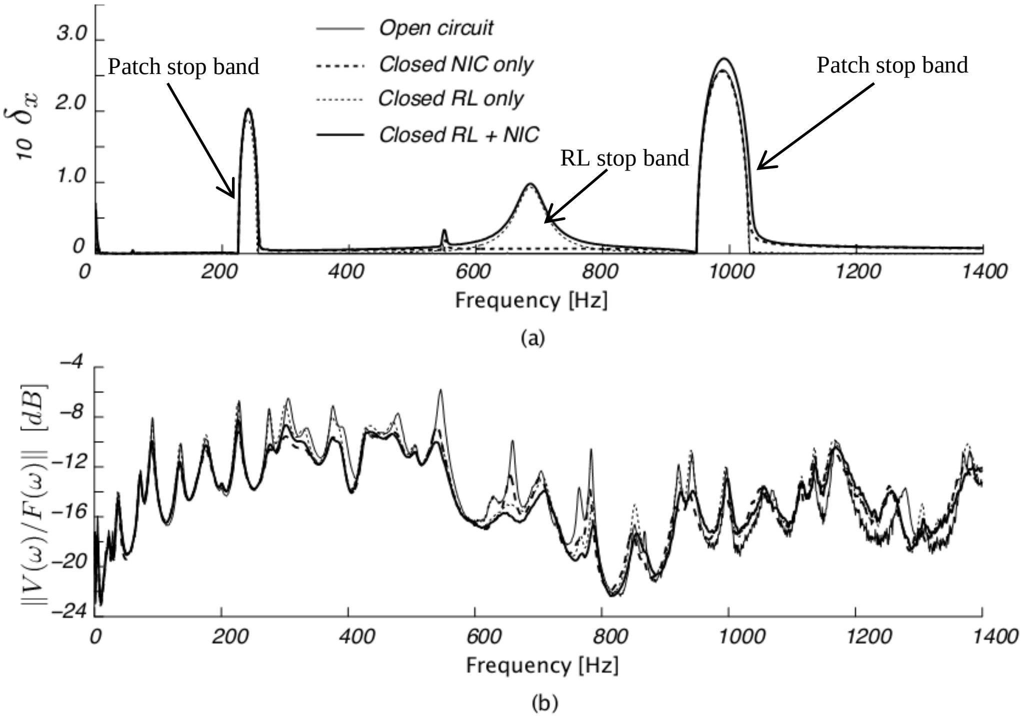

Figure 6.17 - Attenuation constant (a) and measured frequency response (b) of the system in configuration B, RL tuned to 700 Hz

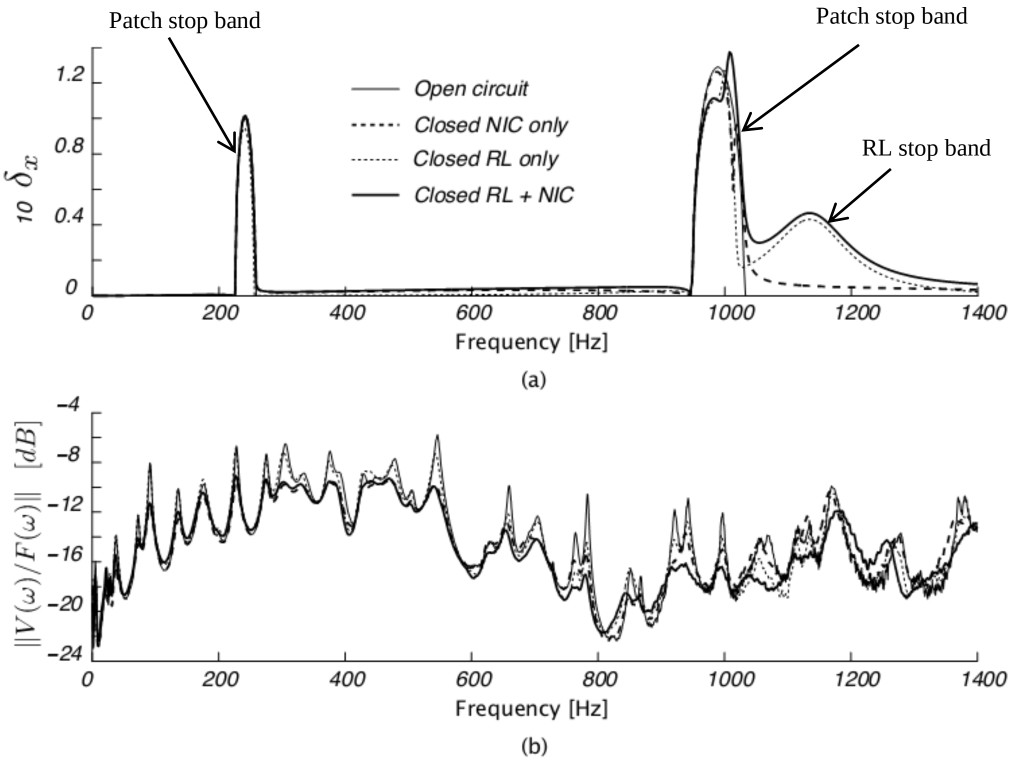

Figure 6.18 - Attenuation constant (a) and measured frequency response (b) of the system in configuration A, RL tuned to 1150 Hz

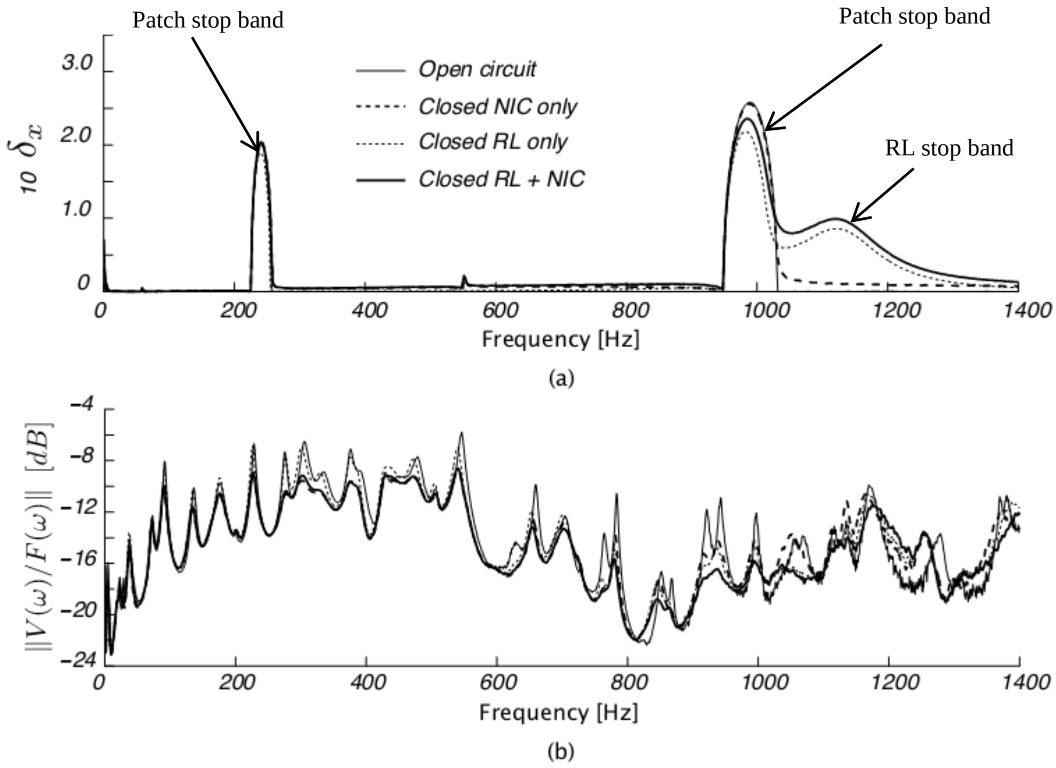

Figure 6.19 - Attenuation constant (a) and measured frequency response (b) of the system in configuration B, RL tuned to 1150 Hz

6.4 Summary

For a one dimensional waveguide, the effect of the negative capacitance shunted piezoelectric patch on a cantilever beam is a reduction in overall vibratory response. A dispersion analysis approximates the frequency dependence effect of the shunt, but the propagation constant does not give a precise measure for each resonance of a modal system. Increasing array length causes an increase in vibration control, with a maximum spatial average velocity suppression of 12 dB on an experimental beam. The control array also results in the beam to begin to act as if it there is an anechoic termination where more of the vibration energy is localized between the forcing location and the patch array.

A 2-D periodic structure with hybrid arrays of RL and negative capacitance shunts is used to attenuate the vibration level of an aluminum plate at both low- and mid-frequencies. Numerical investigations demonstrated that the simultaneous combination of different shunting strategies allows for both broadband and specific frequency damping. Experimental measurements showed that when the RL and negative capacitance shunting networks are combined, the resulting effect is given by the combination of the beneficial effects of the single circuits. This behavior is even more evident when the RL circuits are tuned to a frequency region of poor performance of the negative capacitance networks. Similar results were obtained for different tuning frequencies and periodic configurations to demonstrate the effectiveness and robustness of the proposed control strategy.

CHAPTER 7

CONCLUSIONS

The two major areas of contribution in this work with regard to negative capacitance piezoelectric shunts are the determination of the correlation between electromechanical behavior and suppression of a vibrating system and a study of the effect of the shunt-patch system in periodic arrays on beams and panels. The research documented in this dissertation has determined both electromechanical and structural improvements to negative capacitance shunted piezoelectric transducers.

Two investigations were made into the performance of a negative capacitance shunt connected to a piezoelectric patch. First, a numerical parameter study of the negative capacitance shunt was performed to determine the effect of the shunt on the stiffness and damping of a piezoelectric patch. This study concluded that for ideal circuit components it is possible to obtain infinite damping ratio for any frequency. Yet, the stiffness and damping ratios are not attainable in practice. Secondly, a comparison study of the two established negative capacitance shunt tuning methods was made. The wave-tuning tuning theory was found to be numerically equivalent to the reactive input power theory. Therefore, inherently, the negative capacitance shunt can be considered an impedance control method.

Three aspects of electromechanical modeling and implementation improvements were developed: an adaptive shunt tuning theory, improved prediction of stability, and improved shunt efficiency. While previous shunt tuning methods necessitated accurate electrical and structural models, a novel tuning theory was developed that utilizes the minimization of a single voltage measurement to determine the shunt parameters that correspond to maximum vibration suppression. Also from this tuning theory, it was found that the more power dissipated within the series resistor or the power output of the op-amp does not always correspond to more suppression. Secondly, a method was developed to accurately predict the values of negative capacitance that are physically attainable within a stable shunt circuit. Previous stability criterion did not accurately predict unstable circuit values due to simplified electrical assumptions of the shunt and patch. By accounting for both stability and output requirements the accuracy of prediction can be improved by 2-10 times. Lastly, a numerical model was developed to accurately predict the electromechanical response of the system. Through the use of the model, it was possible to improve the power output efficiency of the op-amp through selection of the shunt's passive circuit components and to quantify the limitations of a negative capacitance shunt.

The second area of contribution of this dissertation is in the study of the effect of the negative capacitance shunt applied in 1- or 2-D periodic arrays. Since negative capacitance shunts connected to a periodic array had not previously been shown experimentally, the wave propagation advantages of a periodic array in conjunction with the shunt were investigated. When applied to a periodic array, the negative capacitance created broadband suppression of the propagating wave. Similarly, through proper component selection, the spectrum of the suppression could be tailored. The frequency behavior of the shunt was predicted by the propagation constant solved for using a finite element model. A numerical model of a long cantilever beam exhibited the same frequency behavior as the propagation constant for various shunt conditions. It was also found that the negative capacitance shunt can also obtain broadband control when applied to a 2-D periodic array.

7.1 Further Work

The results of this work lead to several opportunities for future research. First, a closed-loop controller could be developed to adaptively tune the circuit parameters to impose maximum suppression of vibration using the experimental tuning theory developed in this work. By using digital potentiometers and a field-programmable gate array or analog methods, the tuning theory could be implemented experimentally. Similarly, the stability prediction method would lead to gain limits on the minimization function to guard against circuit configurations which would cause instability of the circuit.

With regard to structural or mechanical research, the construction of a piezoelectric patch array could be optimized for a given system. A negative capacitance shunt was shown to significantly decrease the vibration response of a cantilever beam, but the beam had a single resonance that could not be controlled. To combat this, the array could be constructed in a non-periodic fashion or consist of a multi-patch unit cell with separate circuit configurations per patch. Other modifications to location, size, and geometry of the patch array could be made to increase the suppression for a given goal. Similarly, the negative capacitance shunt control system should be applied to more complex test structures such as a stiffened aircraft panel.

Lastly, the combination of stability prediction method and a periodic array could be made to tailor the shunt impedance for a given design goal. Currently, a periodic array is utilized to reduce the transmitted wave through the array but could just as easily be utilized to minimize the reflected wave. Also, the current frequency behavior of the shunt is not optimal for all frequencies. Therefore, given an optimized frequency-dependent impedance, the stability prediction method could be utilized to determine shunt parameters to best fit that impedance.

REFERENCES

1. Fuller, C.R., S.J. Elliott, and P.A. Nelson, *Active Control of Vibration*. 1996, New York, NY: Academic Press. 332.
2. IEEE/ANSI, *IEEE Standardy on Piezoelectricity,* 1988.
3. Moheimani, S.O.R., *A survey of recent innovations in vibration damping and control using shunted piezoelectric transducers.* IEEE Transactions on Control Systems Technology, 2003. **11**(4): p. 482-94.
4. Burke, S.E. and J. James E. Hubbard, *Active Vibration Control of a Simply Supported Beam Using a Spatially Distributed Actuator.* IEEE Control Systems Magazine, 1987(August): p. 25-30.
5. Burke, S.E. and J.E. Hubbard Jr, *Distributed actuator control design for flexible beams.* Automatica, 1988. **24**(5): p. 619-627.
6. Crawley, E.F. and J.d. Luis, *Use of piezolectric actuators as elements of intelligent structures.* AIAA Journal, 1987. **25**(10): p. 1373-1385.
7. Vipperman, J.S. and R.L. Clark, *Implications of using colocated strain-based transducers for output active structural acoustic control.* Journal of the Acoustical Society of America, 1999. **106**(3): p. 1392-1399.
8. Niederberger, D., *Smart Damping Materials using Shunt Control*, 2005, Swiss Federal Institute of Technology (ETH) Zurich.
9. Moheimani, S.O.R. and A.J. Fleming, *Piezoelectric Transducers for Vibration Control and Damping*. Advances in Industrial Control, ed. M.J. Grimble and M.A. Johnson. 2006, London: Springer-Verlag.

10. Hagood, N.W. and A. von Flotow, *Damping of structural vibrations with piezoelectric materials and passive electrical networks.* Journal of Sound and Vibration, 1991. **146**(2): p. 243-68.

11. Park, J. and D.L. Palumbo. *A New Approach to Identify Optimal Properties of Shunting Elements for Maximum Damping of Structural Vibration Using Piezoelectric Patches*. in *Active 2004*. 2004. Williamsburg, VA: CD Proceedings published by the Institute of Noise Control Engineers.

12. Forward, R.L., *Electronic damping of vibrations in optical structures.* Applied Optics, 1979. **18**: p. 690-697.

13. Kim, J. and J.-Y. Choi, *Performance test for transmitted noise reduction of smart panels using piezoelectric shunt damping.* Smart Materials and Structures, 2005. **14**(6): p. 587-593.

14. Thorp, O., M. Ruzzene, and A. Baz, *Attenuation and localization of wave propagation in rods with periodic shunted piezoelectric patches.* Smart Materials and Structures, 2001. **10**(10): p. 979-989.

15. Caruso, G., *A critical analysis of electric shunt circuits employed in piezoelectric passive vibration damping.* Smart Materials and Structures, 2001. **10**(5): p. 1059-68.

16. Wu, S.-Y. *Piezoeleciric shunts with a parallel R-L circuit for structural damping and vibration control*. in *SPIE - Smart Structures and Materials*. 1996. Newport Beach, CA, USA.

17. Hollkamp, J.J. and R.W. Gordon, *An experimental comparison of piezoelectric and constrained layer damping.* Smart Materials and Structures, 1996. **5**(5): p. 715-22.

18. Park, C.H., *Dynamics modelling of beams with shunted piezoelectric elements.* Journal of Sound and Vibration, 2003. **268**: p. 115–129.

19. Casadei, F., et al. *Vibration Control of Plates Featuring Periodic Arrays of Hybrid Shunted Piezoelectric Patches* in *SPIE - Smart Structures and Materials 2009: Active and Passive Smart Structures and Integrated Systems* 2009. San Diego, CA, USA.

20. Spadoni, A., M. Ruzzene, and K. Cunefare, *Vibration and Wave Propagation Control of Plates with Periodic Arrays of Shunted Piezoelectric Patches.* Journal of Intelligent Material Systems and Structures, 2009. **20**(8): p. 979-990.

21. Horowitz, P. and W. Hill, *The Art of Electronics*. 2nd ed. 1996, New York, NY: Cambridge University Press. 1125.

22. Hollkamp, J.J., *Multimodal passive vibration suppression with piezoelectric materials and resonant shunts.* Journal of Intelligent Material Systems and Structures, 1994. **5**(1): p. 49-57.

23. Wu, S.Y. *Method for multiple mode shunt damping of structural vibration using a single PZT transducer*. in *SPIE - Smart Structures and Materials 1998: Passive Damping and Isolation, 2-3 March 1998*. 1998. San Diego, CA, USA.

24. Behrens, S., S.O.R. Moheimani, and A.J. Fleming, *Multiple mode current flowing passive piezoelectric shunt controller.* Journal of Sound and Vibration, 2003. **266**: p. 929-942.

25. Niederberger, D., et al., *Adaptive multi-mode resonant piezoelectric shunt damping.* Smart Materials and Structures, 2004. **13**(4): p. 1025-1035.

26. Aoki, Y., P. Gardonio, and S.J. Elliott, *Rectangular plate with velocity feedback loops using triangularly shaped piezoceramic actuators: Experimental control performance.* Journal of the Acoustical Society of America, 2008: p. 1421-1426.

27. Bailey, T. and J. James E. Hubbard, *Distributed Piezoelectric-Polymer Active Vibration Control of a Cantilever Beam.* AIAA Journal, 1985. **8**(5): p. 605-611.

28. Gardonio, P., E. Bianchi, and S.J. Elliott, *Smart panel with multiple decentralized units for the control of sound transmission. Part I: theoretical predictions.* Journal of Sound and Vibration, 2003. **274**: p. 163-192.

29. Gardonio, P. and S.J. Elliott, *Modal response of a beam with a sensor-actuator pair for the implementation of velocity feedback control.* Journal of Sound and Vibration, 2005. **284**(1): p. 1-22.

30. Elliott, S.J., et al., *Active vibroacoustic control with multiple local feedback loops.* Journal of the Acoustical Society of America, 2001. **111**(2): p. 908-915.

31. Lee, Y.-S., P. Gardonio, and S.J. Elliott, *Coupling analysis of a matched piezoelectric sensor and actuator pair for vibration control of a smart beam.* Journal of the Acoustical Society of America, 2002. **111**(6): p. 2715-2726.

32. Tsai, M.S. and K.W. Wang, *A coupled robust control/optimization approach for active-passive hybrid piezoelectric networks.* Smart Materials and Structures, 2002. **11**: p. 389-395.

33. Yoon, H.-S. and G. Washington, *Active Vibration Control of Flexible Structures Using Piezoceramic Patch Actuators.* Journal of Intelligent Material Systems and Structures, 2008. **19**: p. 145-155.

34. Tang, J. and K.W. Wang, *Vibration control of rotationally periodic structures using passive piezoelectric shunt networks and active compensation.* Transactions of the ASME Journal of Vibration and Acoustics, 1999. **121**(3): p. 379-90.

35. Tang, J. and K.W. Wang, *Active-passive hybrid piezoelectric networks for vibration control: comparisons and improvement.* Smart Materials and Structures, 2001. **10**(August): p. 794-806.

36. Morgan, R.A. and K.W. Wang. *A multi-frequency piezoelectric vibration absorber for variable frequency harmonic excitations*. in *SPIE - Smart Structures and Materials 2001: Damping and Isolation, 5-7 March 2001*. 2001. Newport Beach, CA, USA.

37. Dosch, J.J., D.J. Inman, and E. Garcia, *A self-sensing piezoelectric actuator for collocated control.* Journal of Intelligent Material Systems and Structures, 1992. **3**(i): p. 166-185.

38. Moheimani, S.O.R., A.J. Fleming, and S. Behrens, *On the feedback structure of wideband piezoelectric shunt damping systems.* Smart Materials and Structures, 2003. **12**: p. 49-56.

39. Fleming, A.J. and S.O.R. Moheimani, *Adaptive piezoelectric shunt damping.* Smart Materials and Structures, 2003. **12**(1): p. 36-48.

40. Quaegebeur, N., P. Micheau, and A. Berry, *Decentralized harmonic control of sound radiation and transmission by a plate using a virtual impedance approach.* Journal of the Acoustical Society of America, 2009. **125**(5): p. 2978-2986.

41. Forward, R.L., *Electromechanical transducer-coupled mechanical structure with negative capacitance compensation circuit*, 1979: United States.

42. Wu, S.-Y. *Broadband piezoelectric shunts for passive structural vibration control*. in *SPIE - Smart Structures and Materials 2001: Damping and Isolation, 5-7 March 2001*. 2001. Newport Beach, CA, USA.

43. Bisegna, P. and G. Caruso. *On the use of negative capacitances for vibration damping of piezoactuated structures*. in *SPIE - Smart Structures and Materials 2005. Damping and Isolation, March 2005*. 2005. San Diego, CA, USA.

44. Browning, D.R. and W.D. Wynn, *Vibration damping system using active negative capacitance shunt circuit with piezoelectric reaction mass actuator*, 1996, Lucent Technologies: United States.

45. Park, C.H. and A. Baz, *Vibration control of beams with negative capacitive shunting of interdigital electrode piezoceramics.* Journal of Vibration and Control, 2005. **11**: p. 331-346.

46. Kamada, T., R. Kiuchi, and M. Nagai, *Suppression of railway vehicle vibration by shunt damping using stack type piezoelectric transducers.* Vehicle System Dynamics, 2008. **46**(sup1): p. 561-570.

47. Behrens, S., A.J. Fleming, and S.R. Moheimani, *A broadband controller for shunt piezoelectric damping of structural vibration.* Smart Materials and Structures, 2003. **12**(1): p. 18-28.

48. Neubauer, M., et al., *Optimization of damping and absorbing performance of shunted piezo elements utilizing negative capacitance.* Journal of Sound and Vibration, 2006. **298**(1-2): p. 84-107.

49. Bisegna, P. and G. Caruso. *On the use of negative capacitances for vibration damping of piezoactuated structures*. 2005. San Diego, CA, USA: SPIE.

50. Preumont, A., et al., *The damping of a truss structure with a piezoelectric transducer.* Computers & Structures, 2008. **86**(3–5): p. 227-239.

51. Collet, M., K.A. Cunefare, and M.N. Ichchou, *Wave Motion Optimization in Periodically Distributed Shunted Piezoelectric Beam Structures.* Journal of Intelligent Material Systems and Structures, 2009. **20**(7): p. 787 - 808.

52. Date, M., M. Kutani, and S. Sakai, *Electrically controlled elasticity utilizing piezoelectric coupling.* Journal of Applied Physis, 2000. **87**(2): p. 863-868.

53. Bondoux, D. *Piezodamping: a low-power-consumption technique for semi-active damping of light structures*. 1996. Lyon, France: SPIE.

54. Umesh, A.K., A.W. Miles, and G.C. Stephen, *The effect of a negative capacitance circuit on the out-of-plane dissipation and stiffness of a piezoelectric membrane.* Smart Materials and Structures, 2008. **17**(3): p. 035017.

55. Sluka, T., P. Mokrý, and H. Lissek, *A theory of sound transmission through a clamped curved piezoelectric membrane connected to a negative capacitor.* International Journal of Solids and Structures, 2010. **47**(17): p. 2260-2267.

56. Bruneau, H., et al. *Semipassive and semiactive vibration control using new amplified piezoelectric actuators*. 1999. Newport Beach, CA, USA: SPIE.

57. Marneffe, B.d., *Active and Passive Vibration Isolation and Damping via Shunted Transducers*, in *Department of Mechanical Engineering and Robotics*2007, Universite Libre de Bruxelles.

58. Behrens, S., A.J. Fleming, and S.O.R. Moheimani. *New method for multiple-mode shunt damping of structural vibration using a single piezoelectric transducer*. in *SPIE - Smart Structures and Materials 2001: Damping and Isolation, 5-7 March 2001*. 2001. Newport Beach, CA, USA.

59. Fukada, E., et al., *Sound isolation by piezoelectric polymer films connected to negative capacitance circuits.* IEEE Transactions on Dielectrics and Electrical Insulation, 2004. **11**(2): p. 328-333.

60. Imoto, K., et al., *Elasticity Control of Piezoelectric Lead Zirconate Titanate (PZT) Materials Using Negative-Capacitance Circuits.* Japanese Journal of Applied Physics, Part 1 (Regular Papers, Short Notes & Review Papers), 2005. **44**(9B): p. 7019-7023.

61. Date, M., M. Kutani, and S. Sakai, *Methods for controlling the elastic modulus of piezoelectric substances and apparatus therefor*, 2000: United States.

62. Kodama, H., et al., *Elastic wave control element using piezelectric materials*, 2003: United States.

63. Sheng-Bing, C., et al., *Band gap control of phononic beam with negative capacitance piezoelectric shunt.* Chinese Physics B, 2011. **20**(1): p. 014301.

64. Václavík, J. and P. Mokrý, *Measurement of mechanical and electrical energy flows in the semiactive piezoelectric shunt damping system.* Journal of Intelligent Material Systems and Structures, 2012. **23**(5): p. 527-533.

65. Park, C. and H. Park, *Multiple-mode structural vibration control using negative capacitive shunt damping.* Journal of Mechanical Science and Technology, 2003. **17**(11): p. 1650-1658.

66. Kim, J. and Y.-C. Jung, *Broadband noise reduction of piezoelectric smart panel featuring negative-capacitive-converter shunt circuit.* The Journal of the Acoustical Society of America, 2006. **120**(4): p. 2017.

67. Cunefare, K.A. *Negative capacitance shunts for vibration suppression: wave based tuning and reactive input power*. in *Active 2006*. 2006. Adelaide, Australia.

68. Mead, D.J. and Y. Yaman, *The response of infinite periodic beams to point harmonic forces: A flexural wave analysis.* Journal of Sound and Vibration, 1991. **144**(3).

69. Mead, D.J., *A New Method of Analyzing Wave Propagation in Periodic Structures; Applications to Periodic Timoshenko Beams and Stiffened Plates.* Journal of Sound and Vibration, 1986. **114**: p. 9-27.

70. Ruzzene, M. and A. Baz, *Control of Wave Propagation in Periodic Composite Rods Using Shape Memory Alloys.* Transactions of the ASME. Journal of Vibration and Acoustics, 2000. **122**(4): p. 151-159.

71. Hofer, M., et al., *Finite-Element Simulation of Wave Propagation in Periodic Piezoelectric SAW Structures.* IEEE Transactions on Ultrasonics, Ferroelectrics, and Frequency Control, 2006. **53**(6): p. 1192-1201.

72. Brillouin, L., *Wave propagation in periodic structures*. 2nd ed. 1952: Dover.

73. Baz, A., *Active Control of Periodic Structures.* Transactions of the ASME. Journal of Vibration and Acoustics, 2001. **123**(10): p. 472-9.

74. Agnes, G.S. *Piezoelectric Coupling of Bladed-Disk Assemblies*. in *SPIE - Smart Structures and Materials 1999: Passive Damping and Isolation, 1-2 March 1999* 1999. Newport Beach, CA, USA.

75. Zhang, J., K.W. Wang, and H. Yu. *Active coupling enhancement of piezoelectric networks for vibration delocalization of nearly periodic structures*. in *SPIE - Smart Structures and Materials*. 2003. San Diego, CA, USA.

76. Yu, H. and K.W. Wang, *Vibration Suppression of Mistuned Coupled-Blade-Disk Systems Using Piezoelectric Circuity Network.* Transactions of the ASME. Journal of Vibration and Acoustics, 2009. **131**(2).

77. Yu, H. and K.W. Wang, *Piezoelectric Networks for Vibration Suppression of Mistuned Bladed Disks.* Transactions of the ASME. Journal of Vibration and Acoustics, 2007. **129**(5): p. 559-.

78. Bisegna, P. and G. Caruso, *Dynamical behavior of disordered rotationally periodic structures: A homogenization approach.* Journal of Sound and Vibration, 2011. **330**(11): p. 2608-2627.

79. Airoldi, L. and M. Ruzzene, *Wave Propagation Control in Beams Through Periodic Multi-Branch Shunts.* Journal of Intelligent Material Systems and Structures, 2011. **22**(14): p. 1567-1579.

80. Airoldi, L. and M. Ruzzene, *Design of tunable acoustic metamaterials through periodic arrays of resonant shunted piezos.* New Journal of Physics, 2011. **13**(11): p. 113010.

81. Gang, W., C. Shengbing, and W. Jihong, *Low-frequency locally resonant band gaps induced by arrays of resonant shunts with Antoniou's circuit: experimental investigation on beams.* Smart Materials and Structures, 2011. **20**(1): p. 015026.

82. Shengbing, C., et al., *Improved modeling of rods with periodic arrays of shunted piezoelectric patches.* Journal of Intelligent Material Systems and Structures, 2012.

83. Lu, Y. and J. Tang, *Electromechanical tailoring of structure with periodic piezoelectric circuitry.* Journal of Sound and Vibration, 2012. **331**(14): p. 3371-3385.

84. Casadei, F., et al., *Periodic shunted arrays for the control of noise radiation in an enclosure.* Journal of Sound and Vibration, 2010. **329**(18): p. 3632-3646.

85. Bisegna, P., G. Caruso, and F. Maceri, *Optimized electric networks for vibration damping of piezoactuated beams.* Journal of Sound and Vibration, 2006. **289**(4-5): p. 908-937.

86. Cook, R.D., D.S. Malkus, and M.E. Plesha, *Concepts and Applications of Finite Element Analysis*. 3 ed. 1989, New York, NY: Wiley.

87. Park, C.H., *Multi-mode vibration damping device and method using negative capacitance shunt circuits*, 2005: United States.

88. Beck, B., K.A. Cunefare, and M. Ruzzene. *Broadband Vibration Suppression Assessment of Negative Impedance Shunts*. in *SMASIS08*. 2008. Ellicott City, Maryland USA.

89. Wu, S.Y., *Broadband piezoelectric shunts for structural vibration control*, 2000: United States.

90. Beck, B., K.A. Cunefare, and M. Collet. *Experimental Assessment of Negative Impedance Shunts for Vibration Suppression on a Beam*. in *SPIE - Smart Structures and Materials 2008: Active and Passive Smart Structures and Integrated Systems* 2008. San Diego, CA.

91. Behrens, S., A.J. Fleming, and S.O.R. Moheimani. *Series-parallel impedance structure for piezoelectric vibration damping*. in *SPIE - Smart Materials II, 16-18 Dec. 2002*. 2002. Melbourne, Vic., Australia.

92. Beck, B.S., et al. *New method of negative capacitance shunt tuning for vibration control*. 2012. San Diego, California, USA: SPIE.

93. Zhao, Y., *Vibration Suppression of a Quadrilateral Plate Using Hybrid Piezoelectric Circuits.* Journal of Vibration and Control, 2010. **16**(5): p. 701-720.

94. Millott, T.A., et al. *Flight test of active gear-mesh noise control on the S-76 aircraft*. in *54th AHS Forum*. 1998. Washington, DC.

95. Casadei, F., et al., *Broadband vibration control through periodic arrays of resonant shunts: experimental investigation on plates.* Smart Materials and Structures, 2010. **19**(1): p. 1-13.